9-1-2021

# Manipulating the Aliovalent Magnetic Dopants in Ti(IV)-based Oxide Nanocrystals

Muhammad Abdullah
*University of Massachusetts Amherst*

# Manipulating the Aliovalent Magnetic Dopants in Ti(IV)-based Oxide Nanocrystals

A Dissertation Presented

by

Muhammad Abdullah

Submitted to the Graduate School of the
University of Massachusetts Amherst in partial fulfillment
of the requirements for the degree of

DOCTOR OF PHILOSOPHY

September 2021

Chemistry

**Manipulating the Aliovalent Magnetic Dopants in Ti(IV)-based Oxide Nanocrystals**

A Dissertation Presented

by

Muhammad Abdullah

Approved as to style and content by:

_____
Kevin R. Kittilstved, Chair

_____
Scott Auerbach, Member

_____
Dhandapani Venkataraman, Member

_____
Wei Fan, Member

_____
Ricardo Metz, Department Head
Department of Chemistry

## DEDICATION

*To those who inspired but may not read it – perhaps they can't!*

**[Translation in Urdu]**

انتساب

ان کے نام جنہوں نے متاثر کیا مگر کبھی اسکو پڑھیں گے نہیں ۔ شاید وہ پڑھ بھی نہیں سکتے !

## ACKNOWLEDGMENTS

The order in which people are mentioned here in this acknowledgment section is based solely on the mutual interactions and is not intended as the relative level of appreciation.

Foremost, I would like to express my sincere gratitude to my advisor Prof. Kevin Kittilstved for his continuous support during my entire time at UMass Amherst. Working under the supervision of such a skillful person has shaped me as a scientist. I could not have imagined having a better mentor when I needed to define my future ventures. I would also like to thank the rest of my thesis committee, Prof. Dhandapani Venkatraman, Prof. Scott Auerbach, and Prof. Wei Fan, for their encouragement and insightful comments during various stages of my graduate work.

My experiences with the people affiliated with the lab have made my journey much product and beyond expectations. My thesis work would not have been possible without an incredible undergraduate, Ruby Nelson. I am grateful to her for the significant contribution she made over three years working with me. I have many coworkers to thank for the time we spent together in the lab. I greatly appreciate William's help in kick-starting research projects and training me on various tools at the earlier stages of my research. I would also like to extend my gratitude to Fumitoshi, Haneen, Enes, and Jillian for their indispensable support, fruitful discussions, and the wonderful time we spent together in the lab, including all those dine-outs. The stress in graduate school is prevalent, and we all want to erupt a string of complaints to vent out. Jillian and I had several venting sessions almost every day at morning coffee to blow off some steam. I would also thank Gaurav, Hyunggu, and

Taylor, who I enjoyed working with towards the end of time in the lab. In addition, I would like to thank my collaborators Prof. Stephen Nonnenmann, Prof. Nianqiang Wu, Dr. Hui Yang, and people in DV's lab, Emily and Michael. I am also thankful to people I met EPR summer school at Denver. My most extended lab teaching experience working with Prof. Ruthanne Paradise has certainly brought several teaching skills that would remain an integral part of my academic profile. I am very grateful to Bob, Ryan, and Sally for the technical support to customize and troubleshoot various equipment. I am very thankful Louis Raboin for help with microscopy traning. I am also indebted to the staff in the chemistry department, particularly JMS, Vicki, Marv and Rebecca for the administrative help.

A healthy social life is an integral part of my graduate experience and connected to my overall well-being. As my acquaintances became friends, the support became substantive to stay strong through these challenging years. I greatly value the friendship with Hamza Javaid that started back in days at LUMS and then grew out at UMass with the addition of some amazing people. I am very much honored to have Kushboo Singh, Noman Bashir, Yasra Chandio, Sohaib Ahmed, Aimen Gaba, Zaid Ahmed and Adeel Nasarullah in my life. Their support and care have helped me overcome many setbacks to stay focused on my ambitions. I do not have words to express my gratitude to all these wonderful people. I owe some special thanks to Yasra for feeding me through these years. I can never forget in my life the warmth reception I always received from both Yasra and Noman. To my friends scattered around the world; Zeeshan Arshad, Nausheen Rashid, Soneela Asghar, Muhammad Sohail, Muhammad Akmal, Muhammad Rizwan, Irfan Mustafa, Samar Abbas, and

Tayyaba Sheikh, thank you for your thoughts, prayers, and being there whenever I needed a friend. I am also very thankful to my former advisors and mentors, Dr. Irshad Hussain, Dr. Mazhar Hussain, Dr. Muhammad Yaqub, Dr. Badar Uddin, and Dr. Zahid Shafiq, for their guidance and support.

Finally, I would like to thank my family, my inspiring mom, and dad, my sisters and their families, and little Sonia for their love, support, and strength that has made it all possible. I am also thankful to my in-laws and fiancée Amara for their unremitting support. Thanks to everyone else to whom acknowledgment is due.

# ABSTRACT

## MANIPULATING THE ALIOVALENT MAGNETIC DOPANTS IN TI(IV)-BASED OXIDE NANOCRYSTALS

SEPTEMBER 2021

**MUHAMMAD ABDULLAH**

B.S., BAHAUDDIN ZAKARIYA UNIVERSITY PAKISTAN

M.S., LAHORE UNIVERSITY OF MANAGEMENT SCIENCES PAKISTAN

Ph.D., UNIVERSITY OF MASSACHUSETTS AMHERST

Directed by: Professor Kevin R. Kittilstved

The intentional incorporation of impurities or dopants in semiconductors is fundamental to manipulate the properties that render them useful for spintronics, photocatalysis, and optoelectronics. One long-standing challenge in integrating the doped semiconductors in various applications is the design of materials with controlled individual dopant properties such as dopants speciation, valence state, and spin dynamics. Despite several elegant studies to circumvent these material challenges, the quest for new materials with tunable dopant properties to address the theoretical and experimental understanding continues. In this work, we combine synthetic chemistry and various spectroscopies to study a class of materials possessing both substitutional magnetic dopants, surface defects, and tunable charge carrier densities.

This thesis builds off a substantial body of work to understand the defect chemistry and dopant-carrier interactions in colloidal $SrTiO_3$, $BaTiO_3$, and $TiO_2$ nanocrystals (NCs). At the initial stages of this work, the formation of paramagnetic surface defects during hydrothermal synthesis of colloidal $SrTiO_3$ and $BaTiO_3$ NCs is

investigated. These defects are identified as surface adsorbed superoxide radicals formed by reducing molecular oxygen during synthesis. The critical roles of lactate ions as reducing agents, hydrazine as an oxygen scavenger, and choice of precursor are thoroughly explored. In a continuation of this work, the critical role of precursor and slow hydrolysis in dopant incorporation are discussed that has enabled us to prepare sub-10 nm colloidal NCs of $BaTiO_3$ and $TiO_2$ doped with an array of aliovalent magnetic dopants at substitutional $Ti^{4+}$ sites. In a post-synthetic modification, the effect of excess electrons added by the photochemical method on dopant properties is explored. Using various spectroscopies, we presented a reversible control over Fe valence states between $Fe^{3+}$ and $Fe^{2+}$. This observation exists to at least in $SrTiO_3$, $BaTiO_3$, and $TiO_2$ NCs and contrasts with the acceleration of $Cr^{3+}$ spin relaxation time in $SrTiO_3$ NCs found previously. This work demonstrates that dopant-carrier interactions are unique, which depends on the relative position of redox-level of dopants in the band structure and their Zeeman energies under applied magnetic field. This work helped us build the electronic structure of Ti(IV)-based oxide NCs where $Fe^{3+/2+}$ redox-level located within the bandgap acts as trap center for photoexcited carriers while $Cr^{3+/2+}$ is situated above the conduction band. The ability to refine and control these magnetic properties by simply using photons contributes to the fundamental understanding of carriers' interactions in oxide semiconductors and provides insights into the pathways for charge and spin-based applications for energy storage and quantum processing.

# TABLE OF CONTENTS

## LIST OF TABLES

Table Page

## LIST OF FIGURES

Figure Page

# CHAPTER 1

# INTRODUCTION

## 1.1 Doped Semiconductors

Modulating the properties of semiconductors by introducing impurities or defects is a key to impart new functionalities which render them useful for various applications.[1] These impurities are typically foreign elements that are added unintentionally or deliberately during the growth of semiconducting materials. The typical example includes the silicon-based semiconductors which make the backbone of the entire electronic industry today. The intrinsic carrier concentration in silicon is relatively low which make it non-conducting material.[2] However, the addition of a small amount of impurity drastically changes the carrier concentration. As demonstrated in Figure 1.1, incorporation of phosphorous in silicon adds extra electrons while that boron introduces holes making silicon an n-type or p-type semiconductor, respectively. Such dopants are also known as aliovalent dopants as they have different valence states than the host site.

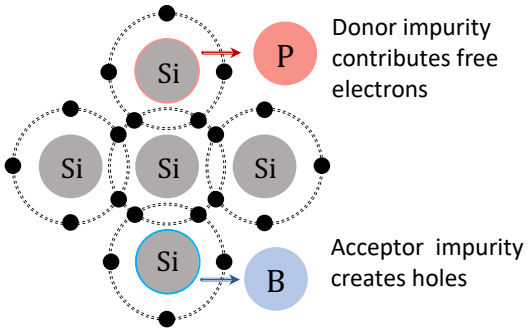


**Figure 1.1** Pictorial representation of silicon doping with phosphorous (n-type dopant) and boron (p-type dopant) to add extra electrons and holes due to differences in the valence states.

This would be hard-pressed to find an electronic device that does not have silicon-based semiconductor in it. Many of the daily usage devices such as computers,

cellphones, automobiles, and all appliances in our kitchens, along with everything with a controlled circuit, has semiconductors integrated into them as a critical component. Aliovalent dopants not only change the carrier concentration and conductivity but also the optical properties of host lattices by introducing impurity levels within the bandgap. For example, Cr dopants in $SrTiO_3$ and $TiO_2$ create sub-bandgap energy levels, enhancing their visible light-harvesting properties involving these new levels.[3] Similarly, Mn dopant in ZnSe and other perovskites imparts emission properties with the potential use in light-emitting diode and related display applications.[4,5] Some of the aliovalent dopants are also known not to create the impurity levels within the bandgap yet alter the optical properties of host materials. The example includes substituting $Nb^{5+}$ in $TiO_2$ and $Al^{3+}$ dopants in ZnO-based lattices as an effective method to tune their optical response, carrier concentration and conductivity.[6,7] Unlike many other transition metal dopants, $Nb^{5+}$ dopant in $TiO_2$ does not create an impurity level within the bandgap but above the conduction band. It seems unrealistic for $TiO_2$ to change its optical response or carrier concentration by simply involving Nb impurity levels. Instead, the substitution of aliovalent $Nb^{5+}$ at $Ti^{4+}$ site in $TiO_2$ adds extra electrons as of charge compensation. These added electrons are typically free in the conduction band giving rise to surface plasmon in the IR region of wavelength. These n-type carriers are also explored for photocatalysis and optoelectronics. [8,9]

Changes in the electronic structures of semiconductors are primarily defined by the individual dopant properties such as its oxidation state, energy level alignment and speciation within the host lattice. For instance, the substitution of $Al^{3+}$ in ZnO acts

as an n-type dopant while the same dopant produces p-type carriers in $SnO_2$.[7,10] Similarly, some dopants do not change the carrier concentration or optical properties; they bring in new functionalities such as magnetism with an example of $Mn^{2+}$ in ZnO.[11] Such dopants are typically isovalent as the oxidation state of dopant is the same as the host site.

Both the aliovalent dopants and isovalent magnetic dopants in semiconductors have been an integral part of technological applications. For example, in conventional silicon-based computing devices that rely on the flow of charge carriers under the influence of an external electrical field, storage is mainly accomplished on magnetic materials. In contrast, the information process is carried out in semiconducting chips containing billions of transistors.[12] As information technology evolves, these devices are expected to perform much faster in an energy-efficient way. However, there are several challenges down the road that includes energy inefficient and time-consuming exchange of information between active processing units and storage systems, the heat generated in microchips with the increasing number of transistors and quantum confinement effects with shrinking the size of technological devices. Therefore, seeking substitute electronic materials for both semiconducting devices and fundamental science is of great interest.

Alternatively, spin-based electronics, so-called “spintronics” have recently led to a new paradigm in technological advancement. Spintronics devices use spin in addition to the charge of electrons that requires far less energy to manipulate the spin states and produce less heat.[13] The practical challenges associated with widespread applications of spintronics include *designing new materials* with tunable properties.

One of the most employed solutions to bring both semiconducting and magnetic properties in a single material is achieved by introducing paramagnetic dopants into semiconducting materials, so-called magnetic semiconductors.[14] Convincing the magnetic semiconductors to exhibit room-temperature ferromagnetism (long-range spin ordering phenomenon) is crucial for their integration into devices for various applications such as spin-based information storage, creation, and transport of spin-polarized current, signal amplification and switching applications.[15] Developing the field of spin-based applications, particularly quantum computing, has become a focused research area across several disciplines of chemistry, materials science and physics which aim to address materials' synthetic challenges, sensitive characterization tools to understand the behavior of magnetic centers and theoretical and experimental understanding of magnetic properties.[16]

### 1.2 $ABO_3$ oxides – a model host-lattice

$SrTiO_3$ and $BaTiO_3$ belong to a class of materials called perovskites with the general chemical formula of $ABO_3$. In the single crystal of the $ABO_3$ unit cell, the B-site cation is $Ti^{4+}$ located at the center of the cube and coordinated to six $O^{2-}$ anions, making a perfect octahedron. While those A-site cations, i.e., $Sr^{2+}$ or $Ba^{2+}$, are located at the corner of the cube as of charge compensation, as shown in Figure 1.2. The coexistence of covalent as well as ionic bonding and unfilled 3*d* shell of $Ti^{4+}$ leads to unique crystal and electronic structure, which make $ABO_3$ a model host lattice for dopant incorporation.[17,18]

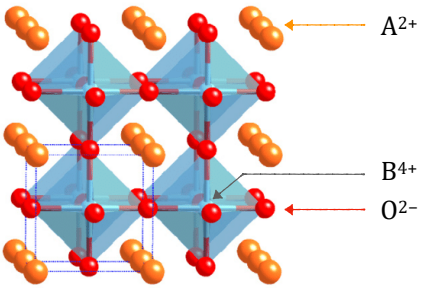


**Figure 1.2** Crystal structure of $ATiO_3$ lattice displaying the position of atoms within the unit cells.

### 1.3 Applications of doped $SrTiO_3$ and associated challenges

$SrTiO_3$ has been proven to be among efficient photocatalytic materials for water splitting and $CO_2$ reduction owing to its proper band alignment with respect to the reaction being catalyzed.[19-21] It has the conduction band located above the standard reduction potential of $H^+/H_2$ reaction and the valence band below the $O_2/H_2O$ reactions. This band position fulfills the fundamental requirement to qualify as a photocatalyst for complete water-splitting reaction. Despite having the appropriate band position, the practical applications of pristine $SrTiO_3$ have been limited due to its optical transparency in the visible region owing to its large bandgap energy (~3.25 eV). It means it can absorption only less than 4% of the available solar spectrum. Therefore, $SrTiO_3$ requires a strategy to make it absorb visible light. The introduction of cationic or anionic dopants into $SrTiO_3$ has been an effective strategy for tuning its bandgap and optical properties. For example, Cr, Ru and Rh doping introduce sub-bandgap states which increases the optical density of $SrTiO_3$ in the visible region making it an efficient light photocatalyst.[22-26] Although these dopants have been known to enhance photocatalytic properties, they can also impart undesired properties. For instance, higher oxidation states such as $Cr^{4+}$ and $Cr^{6+}$ have been known to act as trap centers for photoexcited carriers in $SrTiO_3$ bulk powder, which

can ultimately deteriorate the photocatalytic properties.[27,28] Similarly, aliovalent dopants and multiple oxidation states also manipulate the defect chemistry and produce various crystal disorders that can damage the intrinsic catalytic properties.[29] Therefore, controlled incorporation of dopants with desired oxidation state and speciation is of utmost importance for advancing the applicability of $SrTiO_3$ as a photocatalyst.

$SrTiO_3$ has also drawn attention as a multifunctional material by doping various transition metal ions.[30-32] As an example, Mn-doped $SrTiO_3$ has been reported to exhibit a high dielectric and magnetism simultaneously.[33] Similarly, the substitution of magnetic dopants in $SrTiO_3$ has led to making it dilute magnetic semiconductor (DMS), although the concrete efforts are yet in progress to achieve room temperature ferromagnetism.[34,35] The example includes Pr-doped $SrTiO_3$, where room temperature magnetic ordering has been realized with increasing the dopant concentration.[36] The origin of many of these magnetic properties has been ambiguous and suspected as dopants clustering, the interactions between dopants and free or trapped carriers, presence of interstitial impurities and mixed-valence states of the dopants.[37-40] Integration of $SrTiO_3$ based DMS into technological devices such as spintronics or any related applications demands the theoretical and experimental understanding to prepare high-quality doped $SrTiO_3$. Briefly, there is a need to develop synthetic methodologies that allow the dopant incorporation without clustering or losing control over the oxidation state of dopants and defect formation. There is also a need to understand the interplay between defects and dopants using sophisticated structural and spectroscopic tools.

### 1.4 Specific challenges addressed in the thesis

Our group has been actively studying $SrTiO_3$ bulk powders and colloidal NCs possessing both substitutional dopants and n-type carriers. We combine solid-state to hydrothermal syntheses and various dopant-specific spectroscopies to prepare and characterize doped $SrTiO_3$. There has been a dramatic variance in their properties, such as dopant valence state, speciation, and defect chemistries across the length scale that remain elusive. For example, the substitution of aliovalent $Cr^{3+}$ dopants at $Ti^{4+}$ site in $SrTiO_3$ is compensated by the formation of oxygen vacancies ($V_o$) in bulk powder, while there are no spectroscopically detectable $V_o$ in colloidal NCs.[41,42] Instead, there is the formation of oxygen-related defects on the surface of colloidal NCs which are very sensitive to the presence of additives during the synthesis. Similarly, there is also the existence of higher oxidation states of dopants such as $Cr^{4+}$ and $Cr^{5+}$ in bulk powder which can be reduced to $Cr^{3+}$ by introducing n-type carriers.[27] This observation has also been consistent with Mn dopants which also exist in multiple oxidation states and can be reduced to $Mn^{2+}$ by annealing the powder samples.[43] Conversely, there is no evidence of multiple oxidation states of dopants in colloidal NCs. The introduction of n-type carriers in colloidal NCs instead shows the spin interactions with substitutional $Cr^{3+}$ dopants.[44] The underlying mechanism of such spin interactions, the existence of such phenomenon in other dopants and the effect of host lattices and site symmetries are many of the unanswered questions attempted to address in the current thesis.

In chapter 2, we investigate the formation of paramagnetic surface defects during hydrothermal synthesis of $ATiO_3$ (A = Sr and Ba) colloidal NCs by combing the

synthetic chemistry and a set of spectroscopic tools. We identified these defects as surface adsorbed superoxide radicals formed by reducing molecular oxygen during synthesis. The critical roles of lactate ions as reducing agents and hydrazine as oxygen scavengers have also been thoroughly investigated to establish a correlation between the formation and the control of these surface defects. Chapter 3 discusses the syntheses and photodoping of $Fe^{3+}$-doped $ATiO_3$ colloidal NCs. This work provides a detailed investigation of $Fe^{3+}$ dopants speciation in as-prepared NCs, and reversible control over its valence state ($Fe^{3+}/Fe^{2+}$) by post-synthetic manipulation of Fermi level. We also propose the mechanistic details of this interplay between excess electrons and dopants in electronic structure. In chapter 4, a synthetic method to make aliovalent doped $TiO_2$ colloidal NCs is developed. This method allows the incorporation of an array of dopants such as $Fe^{3+}$, $Nb^{5+}$, and $Cr^{3+}$ at the substitutional $Ti^{4+}$ sites in the $TiO_2$ NCs. Following the synthesis, the effect of excess carriers introduced by (a) photodoping and (b) aliovalent $Nb^{5+}$ doping on $Fe^{3+}$ is explored. This works also opens the avenue for the long-standing challenge of spectroscopic investigation of "air-sensitive" colloidal NCs. Chapter 5 builds off the spin cross-relaxation found previously in $SrTiO_3$ NCs by our group to explore the existence of this phenomenon in structurally similar lattices. A synthetic method for making $Cr^{3+}$-doped $BaTiO_3$ and $Cr^{3+}$-doped $TiO_2$ colloidal NCs has been developed. In this method, we employed slow-hydrolyzing Ti(IV) precursor that allows the successful dopant incorporation at the $Ti^{4+}$ site in $BaTiO_3$ during hydrothermal synthesis. In the second half of this chapter, the introduction of extra charge carriers using photodoping method has been discussed. Our spectroscopic studies showed that these

photochemically introduced electrons are localized at $Ti^{3+}$ defects creating small polarons. The coexistence of both paramagnetic $Cr^{3+}$ and $Ti^{3+}$ in a single lattice shows the spin cross-relaxation phenomenon at room temperature, where fast-relaxing $Ti^{3+}$ accelerates the $Cr^{3+}$ spin relaxation rate.

## 1.5 References


(1) Queisser, H. J.; Haller, E. E. Defects in semiconductors: some fatal, some vital. *Science* **1998,** *281* (5379), 945-950.

(2) Wick, F. G. Some electrical properties of silicon I. thermo-electric behavior of metallic silicon. *Phys. Rev.* **1907,** *25* (5), 382.

(3) Jiao, Z.; Chen, T.; Xiong, J.; Wang, T.; Lu, G.; Ye, J.; Bi, Y. Visible-light-driven photoelectrochemical and photocatalytic performances of Cr-doped $SrTiO_3/TiO_2$ heterostructured nanotube arrays. *Sci. Rep.* **2013,** *3* (1), 1-6.

(4) Guo, D.; Xu, S.; Wang, C.; Wang, Z.; Yin, H.; Deng, H.; Jiang, Y.; Zhang, Z.; Zhang, X.; Shao, H. Doping of Mn2+ into aqueous ZnSe nanocrystals with pure dopant emission through a light-induced electrostatic attraction and diffusion method. *J. Phys. Chem. C* **2021,** *125* (1), 989-997.

(5) Paul, S.; Bladt, E.; Richter, A. F.; Döblinger, M.; Tong, Y.; Huang, H.; Dey, A.; Bals, S.; Debnath, T.; Polavarapu, L. Manganese‐doping‐induced quantum confinement within host perovskite nanocrystals through Ruddlesden‐Popper defects. *Angew. Chem. Int. Ed.* **2020,** *59* (17), 6794-6799.

(6) Su, W.; Song, K.; Huo, D.; Li, B. Analysis of correlation between electrical and infrared optical properties of anatase Nb doped $TiO_2$ films. *Current Applied Physics* **2013,** *13* (3), 556-561.

(7) Zhou, D. M.; Wang, P. J.; Roy, C. R.; Barnes, M. D.; Kittilstved, K. R. Direct evidence of surface charges in n-type Al-doped ZnO. *J. Phys. Chem. C* **2018,** *122* (32), 18596-18602.

(8) Singh, S.; Sharma, V.; Sachdev, K. Investigation of effect of doping concentration in Nb-doped $TiO_2$ thin films for TCO applications. *J. Mater. Sci.* **2017,** *52* (19), 11580-11591.

(9) Nogueira, M.; Lustosa, G.; Kobayakawa, Y.; Kogler, W.; Ruiz, M.; Monteiro Filho, E.; Zaghete, M.; Perazolli, L. Nb-doped $TiO_2$ photocatalysts used to reduction of $CO_2$ to methanol. *Adv. Mater. Sci. & Eng.* **2018,** *2018*.

(10) Benouis, C.; Benhaliliba, M.; Mouffak, Z.; Avila-Garcia, A.; Tiburcio-Silver, A.; Lopez, M. O.; Trujillo, R. R.; Ocak, Y. The low resistive and transparent Al-doped $SnO_2$ films: p-type conductivity, nanostructures and photoluminescence. *J. Alloys Compd.* **2014,** *603*, 213-223.

(11) Norberg, N. S.; Kittilstved, K. R.; Amonette, J. E.; Kukkadapu, R. K.; Schwartz, D. A.; Gamelin, D. R. Synthesis of colloidal $Mn^{2+}$: ZnO quantum dots and high-$T_C$ ferromagnetic nanocrystalline thin films. *J. Am. Chem. Soc.* **2004,** *126* (30), 9387-9398.

(12) O'Regan, G., Transistor. In *The innovation in computing companion*, Springer: 2018; pp 249-252.

(13) Sarma, S. D.; de Sousa, R.; Hu, X.; Koiller, B. Spin quantum computation in silicon nanostructures. *Solid State Commun.* **2005,** *133* (11), 737-746.

(14) Dietl, T. A ten-year perspective on dilute magnetic semiconductors and oxides. *Nat. Mater.* **2010,** *9* (12), 965-974.

(15) Bader, S.; Parkin, S. Spintronics. *Annu. Rev. Condens. Matter Phys.* **2010,** *1* (1), 71-88.

(16) Ohno, H. A window on the future of spintronics. *Nat. Mater.* **2010,** *9* (12), 952-954.

(17) Maier, R. A.; Johnston‐Peck, A. C.; Donohue, M. P. (Magic Dopant) amphoteric behavior of a redox‐active transition metal ion in a perovskite lattice: new insights on the lattice site occupation of manganese in SrTiO3. *Adv. Funct. Mater.* **2016,** *26* (45), 8325-8333.

(18) Buscaglia, M.; Buscaglia, V.; Viviani, M.; Nanni, P.; Hanuskova, M. Influence of foreign ions on the crystal structure of BaTiO3. *J. Eur. Ceram. Soc.* **2000,** *20* (12), 1997-2007.

(19) Wrighton, M. S.; Ellis, A. B.; Wolczanski, P. T.; Morse, D. L.; Abrahamson, H. B.; Ginley, D. S. Strontium titanate photoelectrodes. Efficient photoassisted electrolysis of water at zero applied potential. *J. Am. Chem. Soc.* **1976,** *98* (10), 2774-2779.

(20) Shoji, S.; Yamaguchi, A.; Sakai, E.; Miyauchi, M. Strontium titanate based artificial leaf loaded with reduction and oxidation cocatalysts for selective $CO_2$ reduction using water as an electron donor. *ACS Appl. Mater. Interfaces* **2017,** *9* (24), 20613-20619.

(21) Townsend, T. K.; Browning, N. D.; Osterloh, F. E. Nanoscale strontium titanate photocatalysts for overall water splitting. *ACS nano* **2012,** *6* (8), 7420-7426.

(22) Li, H.; Yin, S.; Wang, Y.; Sekino, T.; Lee, S. W.; Sato, T. Roles of $Cr^{3+}$ doping and oxygen vacancies in $SrTiO_3$ photocatalysts with high visible light activity for NO removal. *J. Catal.* **2013,** *297*, 65-69.

(23) Kato, H.; Kudo, A. Visible-light-response and photocatalytic activities of $TiO_2$ and $SrTiO_3$ photocatalysts codoped with antimony and chromium. *J. Phys. Chem. B* **2002,** *106* (19), 5029-5034.

(24) Yu, H.; Ouyang, S.; Yan, S.; Li, Z.; Yu, T.; Zou, Z. Sol–gel hydrothermal synthesis of visible-light-driven Cr-doped $SrTiO_3$ for efficient hydrogen production. *J. Mater. Chem.* **2011,** *21* (30), 11347-11351.

(25) Kawasaki, S.; Nakatsuji, K.; Yoshinobu, J.; Komori, F.; Takahashi, R.; Lippmaa, M.; Mase, K.; Kudo, A. Epitaxial Rh-doped $SrTiO_3$ thin film photocathode for water splitting under visible light irradiation. *Appl. Phys. Lett.* **2012,** *101* (3), 033910.

(26) Kuo, Y.; Klabunde, K. J. Hydrogen generation from water/methanol under visible light using aerogel prepared strontium titanate ($SrTiO_3$) nanomaterials doped with ruthenium and rhodium metals. *Nanotechnology* **2012,** *23* (29), 294001.

(27) Lehuta, K. A.; Kittilstved, K. R. Reversible control of the chromium valence in chemically reduced Cr-doped $SrTiO_3$ bulk powders. *Dalton Trans.* **2016,** *45* (24), 10034-10041.

(28) Łącz, A.; Drożdż, E. Porous Y and Cr–doped $SrTiO_3$ materials—electrical and redox properties. *J. Solid State Electrochem.* **2019,** *23* (10), 2989-2997.

(29) Osawa, N.; Takahashi, R.; Lippmaa, M. Hole trap state analysis in $SrTiO_3$. *Appl. Phys. Lett.* **2017,** *110* (26), 263902.

(30) Azzoni, C.; Mozzati, M.; Paleari, A.; Massarotti, V.; Bini, M.; Capsoni, D. Magnetic evidence of different environments of manganese ions in Mn-substituted strontium titanate. *Solid State Commun.* **2000,** *114* (12), 617-622.

(31) Inaba, J.; Katsufuji, T. Large magnetoresistance in spin-and carrier-doped $SrTiO_3$. *Phys. Rev. B* **2005,** *72* (5), 052408.

(32) Savinov, M.; Trepakov, V.; Syrnikov, P.; Železný, V.; Pokorný, J.; Dejneka, A.; Jastrabik, L.; Galinetto, P. Dielectric properties of Mn doped $SrTiO_3$. *J. Phys.: Condens. Matter* **2008,** *20* (9), 095221.

(33) Shvartsman, V.; Bedanta, S.; Borisov, P.; Kleemann, W.; Tkach, A.; Vilarinho, P. $(Sr,Mn)TiO_3$: A magnetoelectric multiglass. *Phys. Rev. Lett.* **2008,** *101* (16), 165704.

(34) Kim, H.-S.; Bi, L.; Dionne, G.; Ross, C. Magnetic and magneto-optical properties of Fe-doped $SrTiO_3$ films. *Appl. Phys. Lett.* **2008,** *93* (9), 092506.

(35) Kumar, A. S.; Suresh, P.; Kumar, M. M.; Srikanth, H.; Post, M.; Sahner, K.; Moos, R.; Srinath, S. In *Magnetic and ferroelectric properties of Fe doped $SrTiO_{3-\delta}$ films*, J. Phys.: Conf. Ser., 2010; p 092010.

(36) Durán, A.; Martínez, E.; Díaz, J.; Siqueiros, J. Ferroelectricity at room temperature in Pr-doped $SrTiO_3$. *J. Appl. Phys.* **2005,** *97* (10), 104109.

(37) Sarma, D.; Barman, S.; Kajueter, H.; Kotliar, G. Spectral functions in doped transition metal oxides. *Europhys. Lett.* **1996,** *36* (4), 307.

(38) Choudhury, D.; Mukherjee, S.; Mandal, P.; Sundaresan, A.; Waghmare, U.; Bhattacharjee, S.; Mathieu, R.; Lazor, P.; Eriksson, O.; Sanyal, B. Tuning of dielectric properties and magnetism of $SrTiO_3$ by site-specific doping of Mn. *Phys. Rev. B* **2011,** *84* (12), 125124.

(39) Choudhury, D.; Pal, B.; Sharma, A.; Bhat, S.; Sarma, D. D. Magnetization in electron-and Mn-doped $SrTiO_3$. *Sci. Rep.* **2013,** *3* (1), 1-4.

(40) Zhang, S. Y.; Lin, Y. H.; Nan, C. W.; Zhao, R.; He, J. Magnetic and electrical properties of (Mn,La)‐codoped $SrTiO_3$ thin films. *J. Am. Ceram. Soc.* **2008,** *91* (10), 3263-3266.

(41) Lehuta, K. A.; Kittilstved, K. R. Speciation of Cr(iii) in intermediate phases during the sol–gel processing of Cr-doped $SrTiO_3$ powders. *J. Mater. Chem. A* **2014,** *2* (17), 6138-6145.

(42) Harrigan, W. L.; Michaud, S. E.; Lehuta, K. A.; Kittilstved, K. R. Tunable electronic structure and surface defects in chromium-doped colloidal $SrTiO_{3-\delta}$ nanocrystals. *Chem. Mater.* **2016,** *28* (2), 430-433.

(43) Mansoor, H.; Harrigan, W. L.; Lehuta, K. A.; Kittilstved, K. R. Reversible control of the Mn oxidation state in $SrTiO_3$ bulk powders. *Front. Chem.* **2019,** *7*, 353.

(44) Harrigan, W. L.; Kittilstved, K. R. Reversible modulation of the $Cr^{3+}$ spin dynamics in colloidal $SrTiO_3$ nanocrystals. *J. Phys. Chem. C* **2018,** *122* (46), 26652-26657.

# CHAPTER 2

# ON THE FORMATION OF SUPEROXIDE RADICALS ON COLLOIDAL STRONTIUM AND BARIUM TITANATE NANOCRYSTAL SURFACES

This chapter is published as the following reference: *Nanoscale Adv.* **2020**, 2, 1949-1955

## 2.1 Introduction

$SrTiO_3$ and $BaTiO_3$ are wide-gap semiconductors that have received much attention due to their rich defect chemistries that enable a wide range of electrical properties from insulating to metallic.[1] In addition to exhibiting prototypical quantum paraelectric behavior,[2] these semiconductors are also promising host lattices for visible-light photocatalytic $H_2O$ splitting and $CO_2$ reduction,[3-9] sensors,[10] and memristors.[11,12] Recent advances in the colloidal synthesis[13-20] of ternary metal oxide nanocrystals (NCs), including $SrTiO_3$ and $BaTiO_3$, have generated further interest in emergent phenomena arise in these technologically relevant materials when prepared with nanometer dimensions.

Most of the interesting applications of bulk $SrTiO_3$ result from the presence of two native n-type defects: oxygen vacancies ($V_O$) and self-trapped $Ti^{3+}$ ions. These defects increase the carrier density and mid-gap trapped states which give rise to tunable blue light emission[21] but also greatly influence light absorption in the visible region that has been shown to enhance photocatalytic performance in bulk powders.[22] For example, superoxide radicals ($O_2^{\bullet -}$) present on the surface of Ti(IV)-based metal oxides play an essential role in photocatalysis and degradation of organic pollutants.[23-25] These $O_2^{\bullet -}$ are generally produced by post-synthetic treatments of

reduced titanium oxide-based materials with molecular oxygen ($O_2$) or $H_2O_2$. Yu *et al*. generated surface $O_2^{\bullet-}$ by injecting electrons from photoinduced excited states into adsorbed $O_2$ on the surface of colloidal $TiO_2$ nanoparticles.[26] Another potential use of $O_2^{\bullet-}$ is the catalytical decomposition of $H_2O_2$ on the surface of titanium oxides[27] and oxidative coupling of alkyl radicals.[28] In most of these cases, the metal oxide surface needs to be activated prior to $O_2^{\bullet-}$ formation by irradiation or suitable chemical treatments.

We recently reported the synthesis[29] of colloidal $SrTiO_3$ NCs by modified hydrothermal methods[15,17,18] that are readily suspended in non-polar solvents. Electron paramagnetic resonance (EPR) and optical spectroscopies showed that the $SrTiO_3$ NCs can display spectroscopic signatures that were assigned to an oxygen-related surface defect that is sensitive to the presence of hydrazine hydrate during synthesis. However, the role of hydrazine in the formation of this surface defect remained speculative. Hydrazine has been previously used as an additive during the hydrothermal synthesis of $SrTiO_3$ and $BaTiO_3$ NCs. Sun and co-workers have studied the absorption of hydrazine on the surface of $BaTiO_3$ nanoparticles.[30] Experimental and simulation analysis indicated that only amorphous $BaTiO_3$ particles are obtained without the addition of hydrazine. Similarly, Fujinami *et al*. claimed that $SrTiO_3$ NCs without cubic shape were obtained when synthesis was carried out in the absence of hydrazine.[17] However, our recent report presented evidence that near-cubic colloidal $SrTiO_3$ NCs can be prepared with or without the addition of hydrazine.[29]

Herein we report a systemic investigation of this correlation between hydrazine and the presence of this surface defect in colloidal $SrTiO_3$ NCs. We hypothesize that

the hydrazine may scavenge molecular $O_2$ inside the closed reaction vessel during synthesis, thus providing an inert atmosphere that would inhibit surface $O_2^{\bullet-}$ formation on the NC surface. To test the role of hydrazine, we performed the hydrothermal synthesis both with and without hydrazine prepared in ambient conditions, and also without hydrazine but under anaerobic conditions after purging the reaction solution with argon gas. Reactions performed with hydrazine or under anaerobic conditions produced the same observations and strongly suggest that hydrazine is indeed removing $O_2$ inside the closed reaction vessel. These experiments also strengthen our assignment of the surface-related defect species as $O_2^{\bullet-}$ ions for the $SrTiO_3$ NCs samples prepared aerobically without hydrazine. We propose that lactate ligands of the Ti(IV) precursor reduce $O_2$ to $O_2^{\bullet-}$ ions during the hydrothermal synthesis (200 °C and basic conditions). To support this mechanism and generality of $O_2^{\bullet-}$ formation and the importance of lactate ions, we prepared $BaTiO_3$ NCs from the same lactate-containing Ti(IV) precursors as well as a lactate-free precursor. $O_2^{\bullet-}$ defects are observed only in NCs prepared from a precursor that contains lactate ligands under aerobic conditions. These results provide convincing evidence that the choice of precursor can lead to unique surface chemistry and the formation of $O_2^{\bullet-}$ defects on titanate-based NCs.

## 2.2 Experimental

### 2.2.1 Materials

Strontium hydroxide octahydrate ($Sr(OH)_2{\cdot}8H_2O$, 99%, Alfa Aesar), barium hydroxide octahydrate ($Ba(OH)_2{\cdot}8H_2O$, 99.95%, Acros Organics), titanium(IV) bis(ammonium lactate) dihydroxide (TALH, 50% in water, Alfa Aesar), titanium(IV)

tert-butoxide ($Ti(OBu)_4$, 99%, Acros Organics), 1-butanol (99%, Across Organics), tetramethylammonium hydroxide ($NMe_4OH$, Acros Organics), sodium hydroxide (NaOH, Certified ACS, Fisher Chemical), hydrazine hydrate (99%, Acros Organics), oleic acid (90%, Fisher Chemical), oleylamine (50%, TCI America), ethanol (200 proof, PHARMCO-AAPER) and hexanes (optima grade, Fisher Chemicals) were all used as received.

### 2.2.2 Synthesis of Nanocrystals

**Synthesis of colloidal $SrTiO_3$ NCs from TALH.** Synthesis of colloidal $SrTiO_3$ NCs was carried out by the hydrothermal method as reported previously by our group.[29] In a typical procedure, 1.25 mmol of each of TALH and $Sr(OH)_2$ were dissolved in 30 mL of distilled water in a 45-mL Teflon-lined autoclave. The pH of the solution was then adjusted to 12.1 with a 10 M $NMe_4OH$ solution followed by the addition of oleic acid (2.5 mmol). The reaction vessel was then sealed and heated to 200 °C in the oven for 24 hours. The resulting NCs were collected, washed with ethanol three times, and suspended in hexanes. This procedure described above is referred to herein as method-I.

Method-I was modified to prepare two different sets of colloidal NCs. In the first modification, referred to as method-II, hydrazine hydrate (5 mmol) was added to reaction mixture before adding oleic acid. The pH of the solution remained at 12.1 after the addition of hydrazine hydrate. The last modification, method-III, was identical to method-I but the reaction solution was purged with argon gas for 60 minutes prior to closing the Teflon-lined reaction vessel.

**Synthesis of colloidal $BaTiO_3$ NCs from TALH.** Synthesis of colloidal $BaTiO_3$ NCs was also carried out by a similar hydrothermal method and TALH precursor but included constant magnetic stirring. In a typical preparation, 1.5 mmol of each TALH and $Ba(OH)_2$ were dissolved in 24 mL distilled water followed by the addition of 6 mL of NaOH (5 M). The reaction solution was then transferred to a 45-mL Teflon-lined autoclave and oleylamine (6 mmol) and oleic acid (6 mmol) were added. The pH of the reaction solution was 12. The sealed autoclave was placed in custom-made aluminum block housing heated to 215 °C and constantly stirred for 24 h using a stirring hotplate. After the synthesis, the autoclave was cooled to room temperature and the solid product was collected, washed with EtOH, and dissolved in nonpolar solvents such as hexanes to produce a transparent solution. This procedure described above is referred to herein as method-A. In addition, Method-A was modified to prepare another set of $BaTiO_3$ NCs referred to as method-B. In this modification, hydrazine hydrate (5 mmol) was added before adding the oleylamine and oleic acid. Method-A and -B for $BaTiO_3$ mimic method-I and -II for the $SrTiO_3$ NCs.

**Synthesis of $BaTiO_3$ NCs from $Ti(OBu)_4$.** Synthesis of lactate-free $BaTiO_3$ NCs was done using an aerobic hydrothermal method adopted from the literature.[31] In a typical experiment, aqueous solutions containing 1 mmol of $Ba(OH)_2$ dissolved in 5 mL water and 12.5 mmol of NaOH dissolved in 5 ml water were mixed with 10 mL of 1-butanol containing 1 mmol $Ti(OBu)_4$ and 2.5 mL of oleic acid. The pH of the solution was 12.2. The resulting precursor solution was transferred to a 45-mL autoclave, closed under ambient conditions, and heated to 180 °C for 18 hours. The resulting

product was collected, washed with EtOH several times, and dispersed in non-polar solvents such as hexanes.

### 2.2.3 Physical Characterization

All measurements were collected at room temperature unless specified otherwise. Electronic absorption spectra were collected on colloidal suspensions in air-tight quartz cuvettes with 1-cm pathlengths (Cary 50 Bio). EPR spectra were measured at X-band frequency (9.6 GHz) with a Bruker Elexsys-500 equipped with a Super High QE (ER4123SHQE) cavity. Transmission electron microscopy (TEM) images of NCs deposited onto copper grids (CF400-CU-50, Electron Microscopy Sciences) with a 3 nm carbon coating (JEOL TEM-2000FX). Powder X-ray diffraction patterns were collected in the Bragg-Brentano configuration with a Cu K-α source (Rigaku SmartLab SE). FTIR spectra were collected using Bruker Alpha-P equipped with a diamond attenuated total reflectance (ATR) crystal. High-resolution electrospray ionization mass spectra (ESI-MS) were collected in negative ion mode with Bruker MicroTOF-II. In a typical sample preparation for ESI-MS, the aqueous reaction mixture from the hydrothermal synthesis was centrifuged to separate NCs from the rest of the water-soluble side-products. The aqueous supernatant was used for ESI-MS measurements with no further purification.

## 2.3 Results and Discussion

The crystallinity and phase purity of the $SrTiO_3$ NCs was confirmed by powder X-ray diffraction (see Supporting Information (SI) Figure 2.7 and Table 2.1). All samples matched to cubic $SrTiO_3$ in the $Pm\bar{3}m$ space group.[32] The similar powder patterns among the samples suggest that modification of hydrothermal synthesis either by

adding hydrazine hydrate or degassing the precursor solution has no effect on the crystalline phase or phase purity. TEM images also demonstrate cuboidal morphology of the $SrTiO_3$ NCs prepared by method-III in agreement with previously reported NC shapes made by method-I or method-II (see SI Figure 2.8).[29]

FTIR absorption measurements collected on $SrTiO_3$ NCs prepared from each method are shown in Figure 2.1. The prominent peaks at 1540 $cm^{-1}$ and 1450 $cm^{-1}$ correspond to the symmetric and asymmetric stretches of the bound carboxylate head group of the surface oleate ligand and are observed in each sample. Aliphatic bands from the oleate surface ligands also appear *ca.* 2900 $cm^{-1}$. All samples thus indicate the NC surfaces are passivated by oleate ligands within the sensitivity of the instrument. These spectra are similar to prior reports of $SrTiO_3$ made in a similar method[17] but at pH 13.5. There is no evidence of N-H stretches from hydrazine in the NCs prepared by method-II that would appear around 3400 $cm^{-1}$.[33] This observation suggests that hydrazine is not being adsorbed on the surface of $SrTiO_3$ NCs. Furthermore, hydrazine adsorption is not expected as it is known to decompose rapidly at this reaction temperature (200 °C) in the presence of oxygen to possible products of $N_2$ and $H_2O$.[34] Fujinami *et al*. also observed essentially no change in pH of the reaction solution after $SrTiO_3$ NC synthesis regardless of whether hydrazine was present, which was speculated to play a different role than decomposing to $NH_3$.[17]

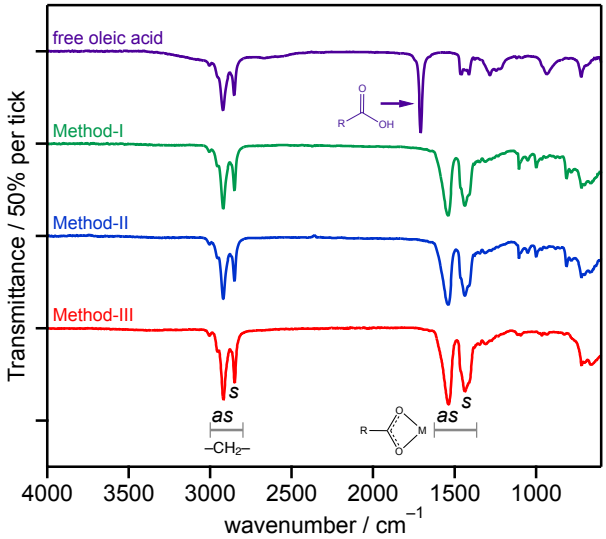


**Figure 2.1** FTIR spectra of solvent-evaporated $SrTiO_3$ NCs prepared by method-I (green), method-II (blue) and method-III (red). The top spectrum belongs to oleic acid (purple). The *s* and *as* next to the peaks refer to the symmetric and asymmetric stretches associated with the aliphatic C-H or carboxylate vibrations.

The electronic absorption spectrum of all colloidal $SrTiO_3$ NCs dispersed in hexanes is dominated by the band edge absorption at *ca*. 3.25 eV consistent with bulk $SrTiO_3$ (see Figure 2.2).[35] However, NCs prepared by the aerobic hydrothermal method-I also exhibit broad absorption throughout the entire visible region and appear reddish-brown (see color photographs shown in Figure 2.2 inset). The broad sub-bandgap absorption is absent in $SrTiO_3$ samples prepared using either method-II or method-III.

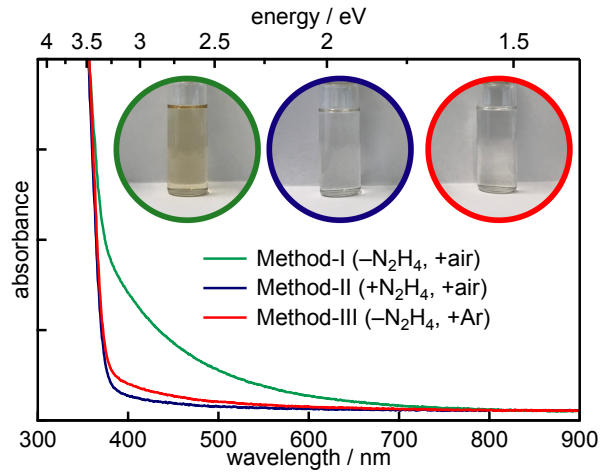

**Figure 2.2** Electronic absorption spectra of colloidal $SrTiO_3$ NCs dispersed in hexanes prepared by method-I (green), method-II (red) and method-III (blue). Optical densities were matched at ~350 nm. Color photographs of NCs dispersed in hexanes are shown in insets.

The origin of the visible absorption in the method-I NCs suggests the presence of defects with sub-bandgap levels. Native point defects such as $V_O$ or $Ti^{3+}$ are also known to give rise to visible light absorption in bulk $SrTiO_3$. Electronic transitions from the valance band to different $V_O$ charge states have been observed between 450 and 550 nm.[36-38] Rice *et al*. recently attributed a transition involving the $V_O$ to an absorption band at *ca*. 405 nm in reduced $SrTiO_3$ crystals.[39] Similar $V_O$ defects have also been described as polarons. However, the electronic transition of the localized electron trapped on $Ti^{3+}$ sites to the conduction band minimum is broad and centered in the near-IR region.[40,41] To explore the origin of the brownish coloration of the $SrTiO_3$ NCs prepared by method-I, we carried out EPR spectroscopy measurements on all three types of $SrTiO_3$ NCs.

The room temperature, X-band EPR spectrum of the $SrTiO_3$ NCs prepared by method-I is shown in Figure 2.3. These NCs exhibit a narrow resonance near 351 mT corresponding to a *g*-value of 2.003. Upon addition of hydrazine (method-II) or purging the precursors with argon (method-III), this EPR signal disappears. Carter *et al*. have identified four types of oxygen-related defects on the surface of $TiO_2$ (anatase-type) using EPR spectroscopy and the signal at $g$=2.003 was assigned to surface-adsorbed paramagnetic superoxide radicals ($O_2^{\bullet-}$, $S$ = 1/2).[42] Those authors also propose the formation involves electron transfer from trapped electrons at $Ti^{3+}$ sites to surface-$O_2$ to produce $O_2^{\bullet-}$. We also tentatively assigned the $g$=2.003 signal to $O_2^{\bullet-}$ in our initial report on the synthesis and characterization of $SrTiO_3$ NCs.[29] We also demonstrated in a more recent report that this $g$ = 2.003 signal can be increased upon

exposing the photochemically reduced ($Ti^{3+}$-rich) $Cr^{3+}$-doped $SrTiO_3$ NCs to air.[41] Others have also reported a $TiO_2$-based NCs treated with $H_2O_2$ that display similar absorption in the visible region originating from surface-adsobed $O_2^{\bullet-}$ defects.[43,44] Based on the similarity to previous reports and observations,[41,43] we attribute the reddish-brown coloration and EPR resonance at $g$=2.003 observed in Figures 2 and 3, respectively, to the presence of $O_2^{\bullet-}$ radicals on the surface of $SrTiO_3$ NCs prepared under aerobic hydrothermal conditions (method-I). We further assign the visible absorption to defect-induced sub-bandgap states that give rise to charge transfer-like transitions.

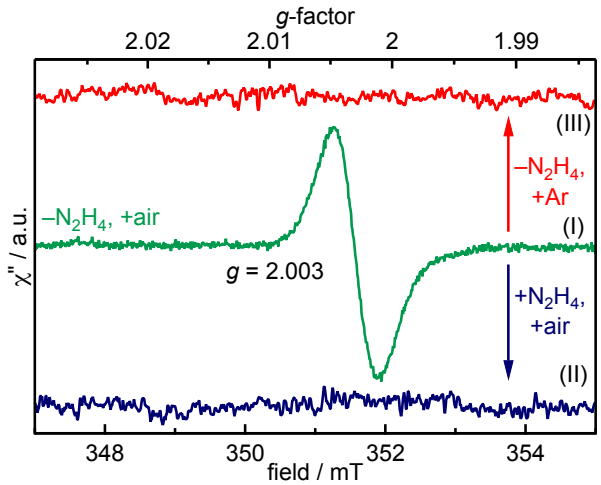


**Figure 2.3** Room temperature EPR spectra of NCs prepared by method-I (middle/green), method-II (bottom/blue), and method-III (top/red).

Our working hypothesis is that the $O_2^{\bullet-}$ ions are formed via reduction of dissolved $O_2$ during the hydrothermal synthesis. The lack of $O_2^{\bullet-}$ formation when prepared by either method-II or method-III is thus presumably due to a very low $O_2$ content in the reaction solution during the hydrothermal synthesis. Despite these results, we do not have a direct mechanistic understanding of how the $O_2^{\bullet-}$ is formed during synthesis. One outstanding question that we sought to answer is the identity of the electron donor. The $O_2^{\bullet-}$ formation at $TiO_2$ surfaces is believed to proceed via electron transfer

from $Ti^{3+}$ sites to adsorbed $O_2$.[45,46] In bulk $SrTiO_3$, oxygen vacancies are thought to exist between adjacent localized $Ti^{3+}$ sites,[47,48] which could serve as an electron donor. However, no spectroscopic evidence for the existence of $V_O$ and any localized $Ti^{3+}$ defects were found in $SrTiO_3$ colloidal NCs. It is possible that these species are only formed under hydrothermal conditions during synthesis but suggests the presence of alternative electron donors such as lactate ions.

The hydrothermal synthesis of $SrTiO_3$ NCs involves the hydrolysis of titanium(IV) bis(ammoniumlactato)dihydroxide (TALH) as the titanium source under basic conditions. Möckel *et al*. have proposed that the hydrolysis of TALH to form $TiO_2$ NCs produces free ammonium lactate in neutral or slightly acidic conditions.[49] Seisenbaeva *et al*. have proposed hydrolysis of TALH forms a stable, tetrameric $(NH_4)_8Ti_4O_4(lactate)_8$ cluster that serves as a precursor to the formation of $TiO_2$ NCs under basic conditions.[50] In both of above-mentioned references, lactate ions are commonly observed as hydrolysis by-product. Lactate ions have been shown to serve as electron donors in various chemical and biological systems to produce $O_2$-based radicals.[51,52] Therefore, we hypothesize that the lactate ions reduce dissolved $O_2$ under extremely high pH to produce $O_2^{\bullet-}$ and the corresponding by-product pyruvate anions as described by Figure 2.4 shown below.

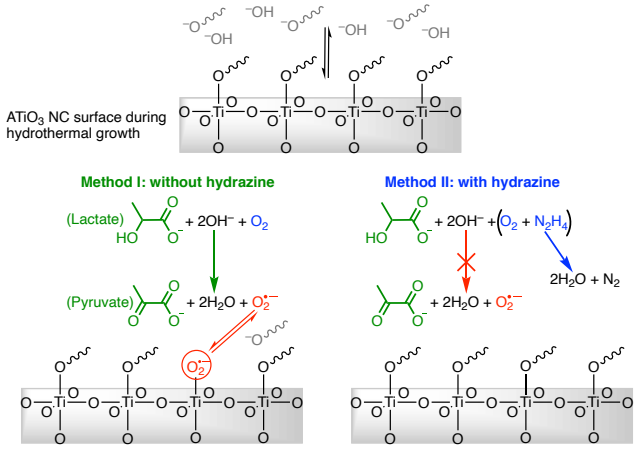


**Figure 2.4** Proposed mechanism of superoxide formation and adsorption onto the dynamic $ATiO_3$ surface during hydrothermal synthesis.

In Figure 2.1, we depict $ATiO_3$ surface that is stabilized by oleate ligands under hydrothermal conditions (pH 12 and 200 °C). At this high temperature, we expect the surface ligands to rapidly exchange between bound and free. This dynamics surface would allow for $O_2^{\bullet-}$ to bind to the surface in Method-I and become stabilized upon cooling to room temperature. In the anaerobic cases, Method-II and Method-III, there is no direct way to produce $O_2^{\bullet-}$ in solution and therefore rule out the possibility of $O_2^{\bullet-}$ adsorption on NC surface.

To confirm the presence of lactate and pyruvate anions, we performed mass spectrometry analysis of reaction supernatants from the various syntheses without purification. Figure 2.5 shows a zoomed-in region of the negative ion mode ESI-MS spectra collected from all three methods. The dominant peak at $m/z$ 89 is attributed to lactate ions which are formed in all three methods consistent with our hypothesis. Despite being weak, the presence of a minority peak at $m/z$ 87 is detected in each of the samples and corresponds to pyruvate ions. When normalized to the lactate signals for the three methods, we detect about a three-fold higher relative intensity of pyruvate anion signal from the supernatant from method-I. While not absolutely

quantitative, the ESI-MS results suggest this conversion yield is <1%. Despite this limitation, the observation is consistent with the proposed mechanism that at least some fraction of the lactate ions undergo the conversion shown in Figure 2.4. The lower $O_2$ content in method-III precludes the $O_2^{\bullet-}$ formation which in turn can be supported by observing relatively a lower pyruvate concentration. However, the absence of any $O_2^{\bullet-}$ defects together with much lower pyruvate content in method-II questions the role of hydrazine in controlling the $O_2^{\bullet-}$ formation during hydrothermal synthesis.

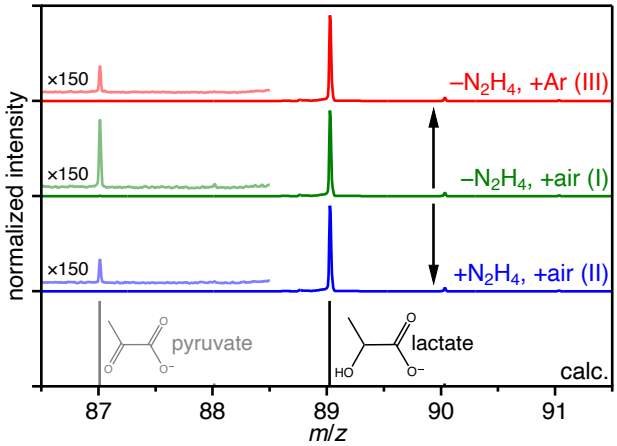


**Figure 2.5** Negative-ion mode ESI-MS of supernatants from the various reactions in the region of the lactate ($[C_3H_5O_3]^{\bullet-}$) and pyruvate ($[C_3H_3O_3]^{\bullet-}$) anions. The spectra are normalized to the major peak from the lactate anion at *m/z* 89.

Based on the results above, hydrazine appears to control the formation of $O_2^{\bullet-}$ defects by limiting the available $O_2$ in the synthesis. Hydrazine has been used to remove $O_2$ in industrial-scale reactors for decades.[53,54] The reaction between hydrazine and $O_2$ produces $N_2$ and $2H_2O$, which provides the inert atmosphere during synthesis as shown in Figure 2.4.[34] Post-synthetic attempts to control the concentration of defects on the surface of the $SrTiO_3$ NCs prepared by Method-I were also performed. When an excess of hydrazine hydrate is added to an aqueous mixture of defect-rich NCs and heated under aerobic hydrothermal conditions, no change in

the appearance of the NCs was observed suggesting no change in surface defects (data not shown).

To test the generality of this approach, we extended the study to $BaTiO_3$ NCs using a similar hydrothermal-based synthesis with TALH and a literature solvothermal method (see SI Figure 2.9-2.12 and Table 2.2). The room temperature EPR spectra of $BaTiO_3$ NCs prepared from all methods is shown in Figure 2.6. Similar to the results for $SrTiO_3$, the appearance of a $O_2^{\bullet-}$ resonance at $g$=2.003 is observed in $BaTiO_3$ samples prepared using TALH and air. The formation of these $O_2^{\bullet-}$ defects can be inhibited by adding hydrazine to remove $O_2$ from the reaction that is consistent with our proposed mechanism.

To confirm the critical role of lactate ions in the formation of these surface $O_2^{\bullet-}$ defects, we synthesized $BaTiO_3$ NCs from a lactate-free titanium precursor, $Ti(OBu)_4$, using similar hydrothermal conditions as used above with TALH.[31] The resulting lactate-free $BaTiO_3$ NCs are transparent below the band gap and do not display any detectable EPR signal as shown in Figure 2.6 and in the SI. This result is entirely consistent with the critical role that lactate ions play in the formation of $O_2^{\bullet-}$ defects during hydrothermal synthesis of $ATiO_3$ and likely also $TiO_2$ NCs.

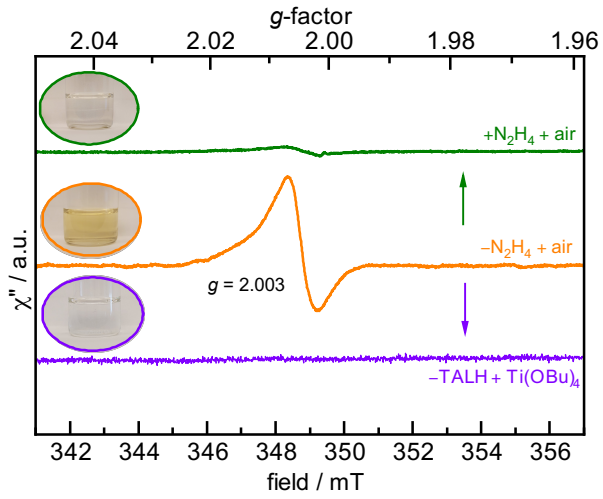


**Figure 2.6** Room temperature EPR spectra of BaTiO3 NCs prepared without hydrazine (orange/middle), with hydrazine (top/green) and from lactate-free precursor (bottom/purple). The color photographs of colloidal solution in hexanes for NCs prepared from all three methods are shown in insets.

## 2.4 Supporting Information

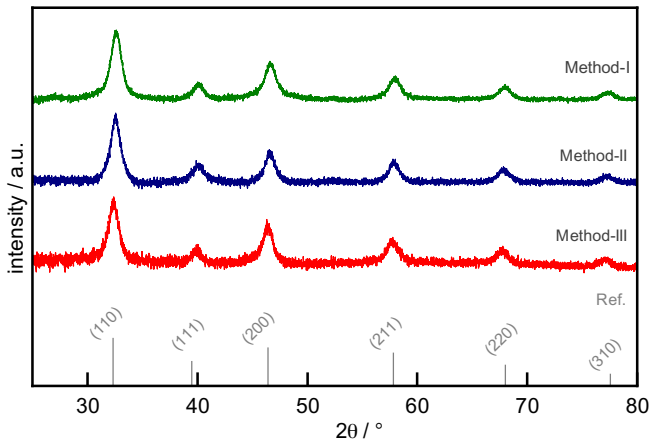


**Figure 2.7** Powder X-ray diffraction patterns of $SrTiO_3$ NCs prepared from all three methods indexed to the cubic phase of bulk $SrTiO_3$ with $Pm\bar{3}m$ space group.[55]

**Table 2.1** The average lattice parameter and crystallite size calculated using Rigaku SmartLab Studio II for all three samples.

| Preparation Method | Lattice parameter (Å) | Crystallite size (nm)† |
|---|---|---|
| I (aerobic without hydrazine) | 3.9069 | 7.3 ± 0.3 |
| II (aerobic with hydrazine) | 3.9162 | 7.5 ± 0.4 |
| III (anaerobic without hydrazine) | 3.9163 | 7.6 ± 0.7 |

†Crystallite size is the average size calculated from the three most intense reflections: (110), (200) and (211).

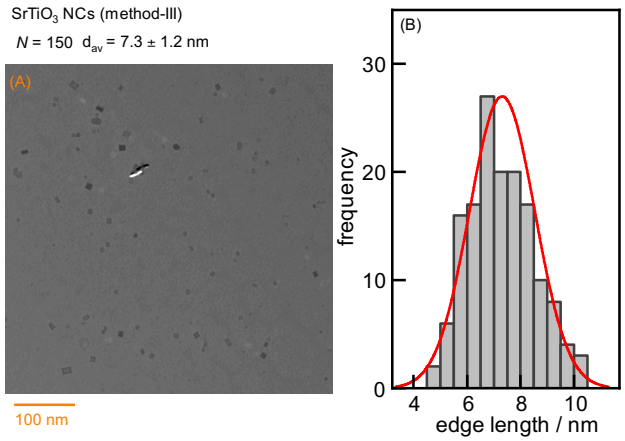


**Figure 2.8** Representative transmission electron microscopy (TEM) image of $SrTiO_3$ NCs prepared from method III (degassed with argon) showing a clear cubic morphology of NCs. The size distribution plot from analyzing over hundred different particles in raw TEM images using ImageJ software displays an average size of 7.3 ± 1.2 nm in good agreement with crystallite size calculated from the diffraction pattern in Figure S1. The cubic morphology of NCs prepared from the method I and method II is already confirmed in our previous report.[56]

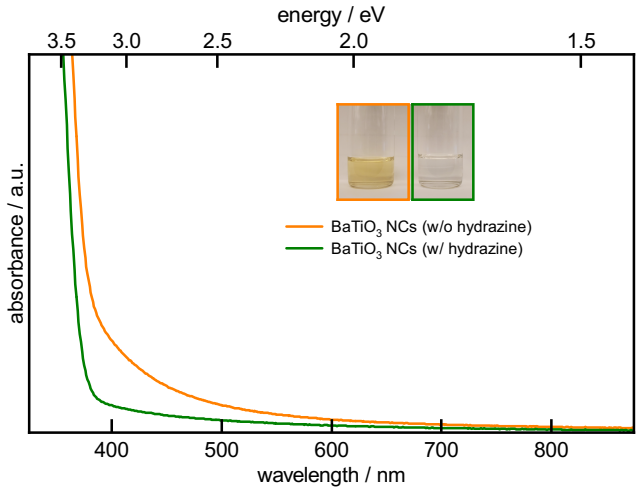


**Figure 2.9** Room temperature electronic absorption spectra of $BaTiO_3$ NCs prepared from method-A (without hydrazine/orange) and method-B (with hydrazine/green). The color photographs of both samples are shown in inset.

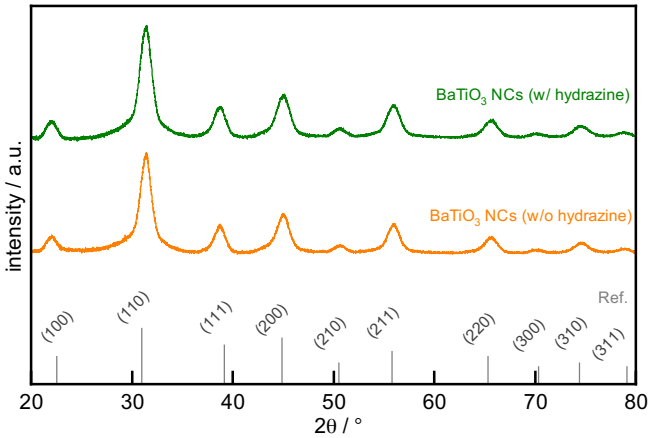


**Figure 2.10** Powder X-ray diffraction pattern of $BaTiO_3$ NCs prepared from method-A (without hydrazine/orange) and method-B (with hydrazine/green) indexed to the cubic phase of $BaTiO_3$.[57]

**Table 2.2** The average lattice parameter and crystallite size calculated using Rigaku SmartLab Studio II for both samples.

| Sample NCs | Lattice parameter (Å) | Crystallite size (nm)† |
|---|---|---|
| With hydrazine | 4.0230 | 5.66 ± 0.50 |
| Without hydrazine | 4.0335 | 6.54 ± 0.53 |

†Crystallite size is the average size calculated from the three most intense reflections: (110), (200) and (211).

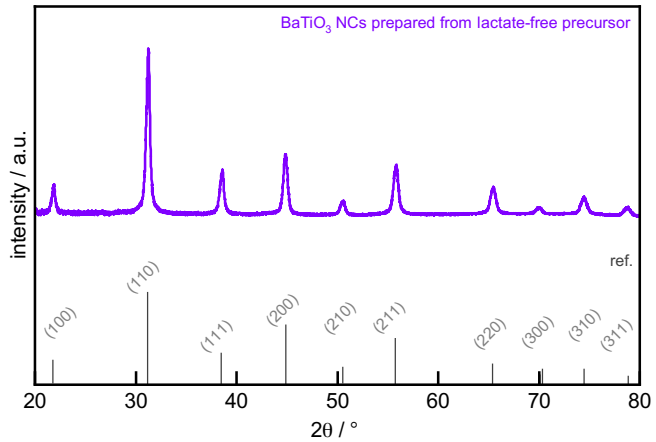


**Figure 2.11** Powder X-ray diffraction pattern of $BaTiO_3$ NCs prepared from lactate-free method indexed to the cubic phase of single-crystal $BaTiO_3$.

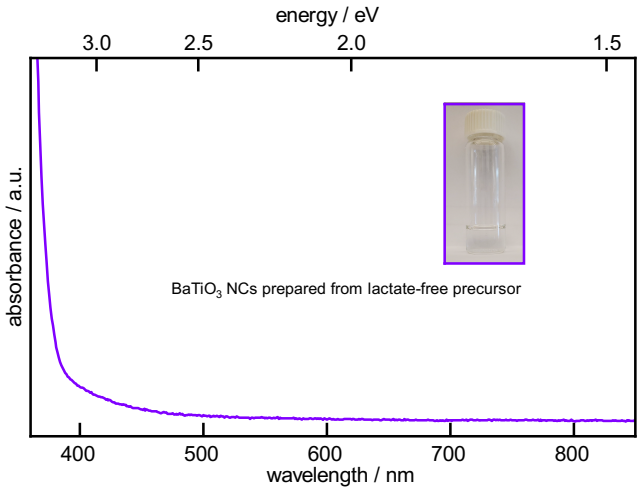


**Figure 2.12** Room temperature electronic absorption spectrum of $BaTiO_3$ NCs prepared from the lactate-free precursor. The color photograph of hexanes solutions of as-prepared NCs is shown in inset.

## 2.5 References

(1) Son, J.; Moetakef, P.; Jalan, B.; Bierwagen, O.; Wright, N. J.; Engel-Herbert, R.; Stemmer, S. Epitaxial $SrTiO_3$ films with electron mobilities exceeding 30,000 $cm^2 V^{-1} s^{-1}$. *Nat. Mater.* **2010,** *9*, 482.

(2) Müller, K.; Burkard, H. $SrTiO_3$: An intrinsic quantum paraelectric below 4 K. *Phys. Rev. B* **1979,** *19* (7), 3593-3602.

(3) Wang, Q.; Hisatomi, T.; Jia, Q.; Tokudome, H.; Zhong, M.; Wang, C.; Pan, Z.; Takata, T.; Nakabayashi, M.; Shibata, N.; Li, Y.; Sharp, I. D.; Kudo, A.; Yamada, T.; Domen, K. Scalable water splitting on particulate photocatalyst sheets with a solar-to-hydrogen energy conversion efficiency exceeding 1%. *Nat. Mater.* **2016,** *15* (6), 611-615.

(4) Shoji, S.; Yamaguchi, A.; Sakai, E.; Miyauchi, M. Strontium titanate based artificial leaf loaded with reduction and oxidation cocatalysts for selective $CO_2$ reduction using water as an electron donor. *ACS Appl. Mater. Interfaces* **2017,** *9* (24), 20613-20619.

(5) Townsend, T. K.; Browning, N. D.; Osterloh, F. E. Nanoscale strontium titanate photocatalysts for overall water splitting. *ACS Nano* **2012,** *6* (8), 7420-7426.

(6) Kato, H.; Kudo, A. Visible-light-response and photocatalytic activities of $TiO_2$ and $SrTiO_3$ photocatalysts codoped with antimony and chromium. *J. Phys. Chem. B* **2002,** *106* (19), 5029-5034.

(7) Ishii, T.; Kato, H.; Kudo, A. $H_2$ evolution from an aqueous methanol solution on $SrTiO_3$ photocatalysts codoped with chromium and tantalum ions under visible light irradiation. *J. Photochem. Photobiol. A* **2004,** *163* (1-2), 181-186.

(8) Niishiro, R.; Kato, H.; Kudo, A. Nickel and either tantalum or niobium-codoped $TiO_2$ and $SrTiO_3$ photocatalysts with visible-light response for $H_2$ or $O_2$ evolution from aqueous solutions. *Phys. Chem. Chem. Phys.* **2005,** *7* (10), 2241.

(9) Kato, H.; Sasaki, Y.; Shirakura, N.; Kudo, A. Synthesis of highly active rhodium-doped $SrTiO_3$ powders in Z-scheme systems for visible-light-driven photocatalytic overall water splitting. *J. Mater. Chem. A* **2013,** *1* (39), 12327.

(10) Sarin, N.; Mishra, M.; Gupta, G.; Parkin, I. P.; Luthra, V. Elucidating iron doping induced n- to p-characteristics of strontium titanate based ethanol sensors. *Curr. Appl. Phys.* **2018,** *18* (2), 246-253.

(11) Baeumer, C.; Schmitz, C.; Ramadan, A. H.; Du, H.; Skaja, K.; Feyer, V.; Muller, P.; Arndt, B.; Jia, C. L.; Mayer, J.; De Souza, R. A.; Michael Schneider, C.; Waser, R.; Dittmann, R. Spectromicroscopic insights for rational design of redox-based memristive devices. *Nat. Commun.* **2015,** *6*, 8610.

(12) Wang, J.; Choudhary, S.; Harrigan, W. L.; Crosby, A. J.; Kittilstved, K. R.; Nonnenmann, S. S. Transferable memristive nanoribbons comprising solution-processed strontium titanate nanocubes. *ACS Appl. Mater. Interfaces* **2017,** *9* (12), 10847-10854.

(13) Beier, C. W.; Cuevas, M. A.; Brutchey, R. L. Low-temperature synthesis of solid-solution $Ba_xSr_{1-x}TiO_3$ nanocrystals. *J. Mater. Chem.* **2010,** *20* (24), 5074-5079.

(14) Ma, Q.; Kato, K. Nucleation and growth mechanism of barium titanate nanoblocks in hydrothermal process using aqueous titanium compound. *Cryst. Growth Des.* **2017,** *17* (5), 2507-2512.

(15) Dang, F.; Mimura, K.-I.; Kato, K.; Imai, H.; Wada, S.; Haneda, H.; Kuwabara, M. Growth of monodispersed $SrTiO_3$ nanocubes by thermohydrolysis method. *CrystEngComm* **2011,** *13* (11), 3878-3883.

(16) Canu, G.; Buscaglia, V. Hydrothermal synthesis of strontium titanate: thermodynamic considerations, morphology control and crystallisation mechanisms. *CrystEngComm* **2017,** *19* (28), 3867-3891.

(17) Fujinami, K.; Katagiri, K.; Kamiya, J.; Hamanaka, T.; Koumoto, K. Sub-10 nm strontium titanate nanocubes highly dispersed in non-polar organic solvents. *Nanoscale* **2010,** *2* (10), 2080-2083.

(18) Park, K.; Son, J. S.; Woo, S. I.; Shin, K.; Oh, M.-W.; Park, S.-D.; Hyeon, T. Colloidal synthesis and thermoelectric properties of La-doped $SrTiO_3$ nanoparticles. *J. Mater. Chem. A* **2014,** *2* (12), 4217-4224.

(19) O'Brien, S.; Brus, L.; Murray, C. B. Synthesis of monodisperse nanoparticles of barium titanate: toward a generalized strategy of oxide nanoparticle synthesis. *J. Am. Chem. Soc.* **2001,** *123* (48), 12085-12086.

(20) Rabuffetti, F. A.; Brutchey, R. L. Complex perovskite oxide nanocrystals: low-temperature synthesis and crystal structure. *Dalton Trans.* **2014,** *43* (39), 14499-14513.

(21) Kan, D.; Terashima, T.; Kanda, R.; Masuno, A.; Tanaka, K.; Chu, S.; Kan, H.; Ishizumi, A.; Kanemitsu, Y.; Shimakawa, Y.; Takano, M. Blue-light emission at room temperature from $Ar^+$-irradiated $SrTiO_3$. *Nat. Mater.* **2005,** *4* (11), 816-819.

(22) Tan, H.; Zhao, Z.; Zhu, W. B.; Coker, E. N.; Li, B.; Zheng, M.; Yu, W.; Fan, H.; Sun, Z. Oxygen vacancy enhanced photocatalytic activity of pervoskite $SrTiO_3$. *ACS Appl. Mater. Interfaces* **2014,** *6* (21), 19184-19190.

(23) Wang, D.; Zhao, L.; Ma, H.; Zhang, H.; Guo, L. H. Quantitative analysis of reactive oxygen species photogenerated on metal oxide nanoparticles and their bacteria toxicity: The role of superoxide radicals. *Environ. Sci. Technol.* **2017,** *51* (17), 10137-10145.

(24) Li, Y.; Zhang, W.; Niu, J.; Chen, Y. Mechanism of photogenerated reactive oxygen species and correlation with the antibacterial properties of engineered metal-oxide nanoparticles. *ACS Nano* **2012,** *6* (6), 5164-5173.

(25) Hayyan, M.; Hashim, M. A.; AlNashef, I. M. Superoxide ion: Generation and chemical implications. *Chem. Rev.* **2016,** *116* (5), 3029-3085.

(26) Yu, J.; Chen, J.; Li, C.; Wang, X.; Zhang, B.; Ding, H. ESR signal of superoxide radical anion adsorbed on $TiO_2$ generated at room temperature. *J. Phys. Chem. B* **2004,** *108* (9), 2781-2783.

(27) Mumtaz, S.; Wang, L. S.; Hussain, S. Z.; Abdullah, M.; Huma, Z.; Iqbal, Z.; Creran, B.; Rotello, V. M.; Hussain, I. Dopamine coated $Fe_3O_4$ nanoparticles as enzyme mimics for the sensitive detection of bacteria. *Chem. Commun.* **2017,** *53* (91), 12306-12308.

(28) Ma, D.; Liu, A.; Li, S.; Lu, C.; Chen, C. $TiO_2$ photocatalysis for C–C bond formation. *Catal. Sci. Technol.* **2018,** *8* (8), 2030-2045.

(29) Harrigan, W. L.; Michaud, S. E.; Lehuta, K. A.; Kittilstved, K. R. Tunable electronic structure and surface defects in chromium-doped colloidal $SrTiO_{3-\delta}$ nanocrystals. *Chem. Mater.* **2016,** *28* (2), 430-433.

(30) Sun, Z.; Zhang, L.; Dang, F.; Liu, Y.; Fei, Z.; Shao, Q.; Lin, H.; Guo, J.; Xiang, L.; Yerra, N.; Guo, Z. Experimental and simulation-based understanding of morphology controlled barium titanate nanoparticles under co-adsorption of surfactants. *CrystEngComm* **2017,** *19* (24), 3288-3298.

(31) Adireddy, S.; Lin, C.; Cao, B.; Zhou, W.; Caruntu, G. Solution-Based Growth of Monodisperse Cube-Like $BaTiO_3$ Colloidal Nanocrystals. *Chem. Mater.* **2010,** *22* (6), 1946-1948.

(32) Mitchell, R. H.; Chakhmouradian, A. R.; Woodward, P. M. Crystal chemistry of perovskite-type compounds in the tausonite-loparite series, $(Sr_{1-2x}Na_xLa_x)TiO_3$. *Phys. Chem. Minerals* **2000,** *27* (8), 583-589.

(33) Giguère, P. A.; Liu, I. D. On the infrared spectrum of hydrazine. *J. Chem. Phys.* **1952,** *20* (1), 136-140.

(34) Bowen, E. J.; Birley, A. W. The vapour phase reaction between hydrazine and oxygen. *Trans. Faraday Soc.* **1951,** *47*, 580-583.

(35) van Benthem, K.; Elsässer, C.; French, R. H. Bulk electronic structure of $SrTiO_3$: Experiment and theory. *J. Appl. Phys.* **2001,** *90* (12), 6156-6164.

(36) Lehuta, K. A.; Kittilstved, K. R. Reversible control of the chromium valence in chemically reduced Cr-doped $SrTiO_3$ bulk powders. *Dalton Trans.* **2016,** *45* (24), 10034-10041.

(37) Zuo, F.; Wang, L.; Wu, T.; Zhang, Z.; Borchardt, D.; Feng, P. Self-doped $Ti^{3+}$ enhanced photocatalyst for hydrogen production under visible light. *J. Am. Chem. Soc.* **2010,** *132* (34), 11856-11857.

(38) Mitra, C.; Lin, C.; Robertson, J.; Demkov, A. A. Electronic structure of oxygen vacancies in $SrTiO_3$ and $LaAlO_3$. *Phys. Rev. B* **2012,** *86* (15), 155105.

(39) Rice, W. D.; Ambwani, P.; Bombeck, M.; Thompson, J. D.; Haugstad, G.; Leighton, C.; Crooker, S. A. Persistent optically induced magnetism in oxygen-deficient strontium titanate. *Nat. Mater.* **2014,** *13* (5), 481-487.

(40) Henglein, A. Colloidal $TiO_2$ catalyzed photo- and radiation chemical processes in aqueous solution. *Ber. Bunsenges. Phys. Chem.* **1982,** *86* (3), 241-246.

(41) Harrigan, W. L.; Kittilstved, K. R. Reversible modulation of the $Cr^{3+}$ spin dynamics in colloidal $SrTiO_3$ nanocrystals. *J. Phys. Chem. C* **2018,** *122* (46), 26652-26657.

(42) Carter, E.; Carley, A. F.; Murphy, D. M. Evidence for $O_2^-$ radical stabilization at surface oxygen vacancies on polycrystalline $TiO_2$. *J. Phys. Chem. C* **2007,** *111* (28), 10630-10638.

(43) Pallavi D, B.; Deu S, B.; Gavisiddappa S, G. Visible light active superoxide modified nanocrystalline anatase titania. *J. Nanoeng. Nanomanuf.* **2015,** *5*, 216-220.

(44) Wei, Z.; Liu, D.; Wei, W.; Chen, X.; Han, Q.; Yao, W.; Ma, X.; Zhu, Y. Ultrathin $TiO_2$(B) Nanosheets as the Inductive Agent for Transfrering $H_2O_2$ into Superoxide Radicals. *ACS Appl. Mater. Interfaces* **2017,** *9* (18), 15533-15540.

(45) Attwood, A. L.; Murphy, D. M.; Edwards, J. L.; Egerton, T. A.; Harrison, R. W. An EPR study of thermally and photochemically generated oxygen radicals on hydrated and dehydrated titania surfaces. *Res. Chem. Intermed.* **2003,** *29* (5), 449-465.

(46) Green, J.; Carter, E.; Murphy, D. M. Interaction of molecular oxygen with oxygen vacancies on reduced $TiO_2$: Site specific blocking by probe molecules. *Chem. Phys. Lett.* **2009,** *477* (4-6), 340-344.

(47) Komaguchi, K.; Maruoka, T.; Nakano, H.; Imae, I.; Ooyama, Y.; Harima, Y. Electron-transfer reaction of oxygen species on $TiO_2$ nanoparticles induced by sub-band-gap illumination. *J. Phys. Chem. C* **2010,** *114* (2), 1240-1245.

(48) Komaguchi, K.; Maruoka, T.; Nakano, H.; Imae, I.; Ooyama, Y.; Harima, Y. ESR study on the reversible electron transfer from $O_2^{2-}$ to $Ti^{4+}$ on $TiO_2$ nanoparticles induced by visible-light illumination. *J. Phys. Chem. C* **2009,** *113* (4), 1160-1163.

(49) Mo, H.; Giersig, M.; Willig, F. Formation of uniform size anatase nanocrystals from bis(ammonium lactato)titanium dihydroxide by thermohydrolysis. *J. Mater. Chem.* **1999,** *9*, 3051-3056.

(50) Seisenbaeva, G. A.; Daniel, G.; Nedelec, J. M.; Kessler, V. G. Solution equilibrium behind the room-temperature synthesis of nanocrystalline titanium dioxide. *Nanoscale* **2013,** *5* (8), 3330-3336.

(51) Bertolino, S. M.; Melgaco, L. A.; Sa, R. G.; Leao, V. A. Comparing lactate and glycerol as a single-electron donor for sulfate reduction in fluidized bed reactors. *Biodegradation* **2014,** *25* (5), 719-733.

(52) Vandieken, V.; Finke, N.; Thamdrup, B. Hydrogen, acetate, and lactate as electron donors for microbial manganese reduction in a manganese-rich coastal marine sediment. *FEMS Microbiol. Ecol.* **2014,** *87* (3), 733-745.

(53) Tsubakizaki, S.; Gotou, H.; Ishihara, N.; Takada, M.; Mawatari, K.; Kai, R. Alternatives to hydrazine in water treatment at thermal power plants. *Mitsubishi Heavy Ind. Tech. Rev.* **2009,** *46* (2), 43-47.

(54) Scrivenand, B.; Winter, T. R. Chemical oxygen scavengers - Use of hydrazine and tannins for boiler water treatment. *Anti-Corros. Method Mater.* **1978,** *25* (10), 10-11.

(55) Mitchell, R.; Chakhmouradian, A.; Woodward, P. Crystal chemistry of perovskite-type compounds in the tausonite-loparite series,$(Sr_{1-2x}Na_x La_x)TiO_3$. *Phys. Chem. Miner.* **2000,** *27* (8), 583-589.

(56) Harrigan, W. L.; Michaud, S. E.; Lehuta, K. A.; Kittilstved, K. R. Tunable electronic structure and surface defects in chromium-doped colloidal $SrTiO_{3-\delta}$ nanocrystals. *Chem. Mater.* **2016,** *28* (2), 430-433.

(57) Smith, M. B.; Page, K.; Siegrist, T.; Redmond, P. L.; Walter, E. C.; Seshadri, R.; Brus, L. E.; Steigerwald, M. L. Crystal structure and the paraelectric-to-ferroelectric phase transition of nanoscale $BaTiO_3$. *J. Am. Chem. Soc.* **2008,** *130* (22), 6955-6963.

# CHAPTER 3

# TUNABLE REDOX ACTIVITY AT IRON CENTERS IN COLLOIDAL STRONTIUM AND BARIUM TITANATE NANOCRYSTALS

This chapter is published as following reference: *Chem. Mater.* **2021**, *33*, 4196-4203

## 3.1 Introduction

Exploiting the properties of semiconductor nanomaterials by incorporating impurities constitutes a long-standing challenge to materials chemistry that has hindered their implementation in various technologies.[1-4] Numerous studies have focused on the design of high-quality colloidal nanocrystals (NCs) with controlled incorporation of either aliovalent dopants to tune the carrier concentration or magnetic dopants for spin-based electronic or quantum information processing applications.[5-8] Significant progress has occurred in recent years with respect to introducing excess charge carriers into metal oxide semiconductors through aliovalent doping,[9,10] control over material stoichiometry,[11,12] photochemical (also known as photodoping),[13,14] doping via electron transfer from a chemical reductant,[15] and electrochemical doping.[16]

An emerging class of substitutional dopants that function simultaneously as aliovalent dopants and paramagnets has received much attention due to their multifunctionality. Examples of such dopants in oxide semiconductors are $Fe^{3+}$-doped ZnO ($Fe^{3+}$:ZnO),[10,17] where $Fe^{3+}$ dopant acts as an electron donor, and $Cr^{3+}$:$SrTiO_3$ where $Cr^{3+}$ substitutes at the $Ti^{4+}$ site and behaves as an acceptor.[18,19] The aliovalent magnetic dopants of relevance to our studies are the 3d transition metal ions in Ti-based oxide semiconductors. $SrTiO_3$ is a wide-gap semiconductor with the bottom of

the conduction band having primarily empty Ti-3d character. This electronic structure feature is common with so-called $d^0$ semiconductors and can be exploited to produce quasi-delocalized $Ti^{3+}$ defect centers (self-trapped electrons) after an increase in carrier concentration.[15,20] Magnetic ordering has also been reported in Ti-based oxide semiconductors containing aliovalent magnetic dopants including $Cr^{3+}$:$TiO_2$, $Co^{2+}$:$TiO_2$, Fe:$SrTiO_{3-\delta}$, and $Co^{2+}$:(La,Sr)$TiO_3$.[21-24]

We recently reported that the spin relaxation time of $Cr^{3+}$ dopants in colloidal $SrTiO_3$ NCs is accelerated by the presence of photochemically introduced $Ti^{3+}$ defects.[25] We demonstrated an apparent enhancement of this effect specifically in the $Cr^{3+}$:$SrTiO_3$ NCs, relative to the $Cr^{3+}$-doped bulk powders.[15] The discovery of this efficient and reversible control over the spin-relaxation time of localized $Cr^{3+}$ motivated our current work to explore the behavior of additional aliovalent magnetic dopants in $d^0$ semiconductor NCs. Herein we report the preparation of sub-10 nm Fe-doped $SrTiO_3$ and $BaTiO_3$ colloidal NCs using hydrothermal methods described previously by our group.[26,27] We confirm that the Fe is in $Fe^{3+}$ state and is located at the octahedral $Ti^{4+}$ sites in as-prepared NCs by electron paramagnetic resonance (EPR) spectroscopy. Upon anaerobic photodoping of colloidal NCs, the EPR signal of $Fe^{3+}$ disappears with increasing $Ti^{3+}$ concentration. The lack of $Fe^{3+}$ EPR signal in the photodoped $SrTiO_3$ and $BaTiO_3$ persists down to 100 K, where the $Ti^{3+}$ EPR signal is observed. These results are consistent with the electrons trapping at the $Fe^{3+}$ sites prior to accumulating at $Ti^{3+}$ defects in these NCs. This electron trapping phenomenon reduces $Fe^{3+}$ to EPR-silent $Fe^{2+}$ centers and can be effectively manipulated as a

function of irradiation time. All of the spectroscopic changes induced by photodoping are fully reversible upon aerobic oxidation of the photodoped sample.

## 3.2 Experimental

### 3.2.1 Materials

Strontium hydroxide octahydrate ($Sr(OH)_2 \cdot 8H_2O$, 99%, Alfa Aesar), barium hydroxide octahydrate ($Ba(OH)_2 \cdot 8H_2O$, 99%, Alfa Aesar), titanium(IV) bis(ammonium lactate) hydroxide (TALH, 50% in water, Alfa Aesar), tetramethylammonium hydroxide ($NMe_4OH$, Acros Organics), sodium hydroxide (NaOH, Certified ACS, Fisher Chemical), hydrazine hydrate ($N_2H_4 \cdot H_2O$, 99%, Acros Organics), oleylamine (>50%, TCI America), oleic acid (>95%, Fisher Chemical), iron nitrate nonahydrate ($Fe(NO_3)_3 \cdot 9H_2O$, 99.99% Sigma Aldrich), ethanol (200 proof, PHARMCO-AAPER), QC-21 elements standard (PerkinElmer, 5% $HNO_3$), nitric acid (Certified ACS Plus, Fisher Chemical), hydrochloric acid (Certified ACS Plus, Fisher Chemical), toluene (Optima, Fisher Chemicals) and hexanes (Optima, Fisher Chemicals) were all used as received.

### 3.2.2 Synthesis of Nanocrystals

**Pure and Fe-doped $SrTiO_3$ colloidal NCs.** Synthesis of colloidal $SrTiO_3$ NCs was carried out by a modified hydrothermal method reported earlier by Harrigan *et al.*[26] In a typical synthesis, 1.25 mmol of TALH and 1.25 mmol of $Sr(OH)_2 \cdot 8H_2O$ were dissolved in 30 mL of distilled water. The pH of the solution was then adjusted to 12.1 with an aqueous solution of $NMe_4OH$ (10 M) followed by the addition of oleic acid (2.5 mmol) and hydrazine (5 mmol). The resulting solution was transferred to a 45 mL Teflon-lined autoclave (4744 General Purpose Acid Digestion Vessel, Parr Instrument Company) and heated to 200 °C in an oven for 24 hours. The resulting NCs were

collected, washed with ethanol several times, suspended in hexanes, and sonicated for about 30 minutes to produce a cloudy suspension. Finally, a transparent hexane layer containing NCs was extracted by centrifuging the cloudy suspension (5 min at 4000 rpm). These NCs can be further purified by precipitation with ethanol. Synthesis of nominally 0.5% Fe-doped $SrTiO_3$ NCs was carried out by adding 625 μL of 0.01 M aqueous solution of $Fe(NO_3)_3 \cdot 9H_2O$ right after adjusting the pH of the precursor solution. Similarly, nominally 1% Fe-doped $SrTiO_3$ NCs were prepared by adding 1.25 mL of 0.01 M aqueous solution of $Fe(NO_3)_3 \cdot 9H_2O$.

**Pure and Fe-doped $BaTiO_3$ colloidal NCs.** Synthesis of $BaTiO_3$ NCs was carried out by a similar hydrothermal method but included constant magnetic stirring.[27] In a typical synthesis, 1.5 mmol of each of TALH and $Ba(OH)_2$ were dissolved in 24 mL distilled water followed by 6 mL of 5 M NaOH aqueous solution. The reaction mixture was then transferred to a 45 mL Teflon-lined autoclave, and oleylamine (6 mmol), oleic acid (6 mmol), and hydrazine (6 mmol) were added. The sealed autoclave was placed in custom-made aluminum block housing heated to 215 °C and stirred continuously for 24 hours using a stirring hotplate. After the synthesis, the autoclave was cooled down to room temperature, and the crude product was collected along with water into two separate test tubes and washed with ethanol (33% by volume) twice. The solid product was then dissolved in hexanes to produce a cloudy suspension with sonication (15 minutes). Finally, the hexane layer containing the NCs was extracted by centrifuging the suspension. Synthesis of nominally 0.5% Fe-doped $BaTiO_3$ NCs was carried out by adding 750 μL of 0.01 M aqueous solution of $Fe(NO_3)_3 \cdot 9H_2O$ before adding NaOH.

### 3.2.3 Physical characterization

All measurements presented below were collected on either pure or 0.5% Fe-doped $SrTiO_3$ NCs (referred to as Fe:$SrTiO_3$ hereafter) and pure or 0.5% Fe-doped $BaTiO_3$ NCs (referred to as Fe:$BaTiO_3$ hereafter) unless specified otherwise. Electronic absorption and emission spectra were collected at room temperature on colloidal NCs in air-tight quartz cuvette on Cary 50 Bio and Cary Eclipse, respectively. Near-IR absorption measurements were collected on Varian 670 FT spectrometer equipped with an InGaAs detector and near-IR quartz beam splitter using a 1-mm pathlength quartz cuvette. The functional groups and surface chemistry analysis of solvent-free NCs were carried out on a Bruker Alpha-P FTIR spectrophotometer equipped with an attenuated total reflectance (ATR) platinum diamond optic. EPR measurements were carried out on continuous wave (CW) Bruker Elexsys-500 fitted with Super High QE X-band cavity (ER4123SHQE) and cryostat (ESR-900, Oxford) for low-temperature measurements. For the photodoping experiments, a 75 W xenon lamp was used (60000 Q series, Oriel Corporation). Transmission electron microscopy (TEM, JEOL 2000FX) images were measured from freshly prepared NCs drop-casted onto carbon-coated (3nm) copper grids (CF400-CU-50, Electron Microscopy Sciences). The average size distribution and standard deviation were generated by analyzing a few hundred particles from TEM images using ImageJ software. Powder X-ray diffraction patterns were collected in a Bragg-Brentano configuration and Cu K-source (Rigaku Smart Lab SE). Metal ion stoichiometry was measured on dissolved ensembles of NCs and measured by an inductively coupled plasma - optical emission spectrometer (ICP-OES, Perkin Elmer Optima 4300 DV).

### 3.2.4 Photodoping

Photodoping experiments were performed to introduce excess electrons in as-prepared NCs. Sample preparation was completed in the argon-filled glove box where NCs suspended in hexanes were transferred to a 1 cm air-tight cuvette before removal. Samples were photodoped by prolonged exposure to unfocused irradiation from 75 W xenon lamp in the presence of EtOH (0.5 mL, >100 eq/NC) as a sacrificial reductant. The electronic absorption spectra were taken periodically during the entire photodoping process. It was estimated that the NCs were photodoped to their saturation limit when no further spectroscopic changes could be observed following prolonged exposure. For in-situ EPR measurements, NCs were transferred to a 4-mm air-free EPR tube, and photodoping procedure inside the EPR resonator was carried out by UV irradiation via fiber optics. The lamp was warmed up 30 min before each photodoping experiment in order to achieve uniform temperature and irradiation intensity.

## 3.3 Results and Discussion

The crystallinity and phase purity of as-prepared undoped and Fe-doped $SrTiO_3$ NCs were confirmed by powder X-ray diffraction measurements (see SI Figure 3.6). The diffraction patterns of both samples are indexed to cubic $SrTiO_3$ (space group: $Pm\bar{3}m$) with no additional secondary phases.[28] A slight increase of the lattice parameter was observed in the Fe:$SrTiO_3$ NCs (see Table 3.1). This typical lattice expansion is attributed to the substitution of a relatively larger $Fe^{3+}$ ion (0.79 Å) at the $Ti^{4+}$ (0.74 Å) sites and is consistent with other spectroscopic evidence of $Fe^{3+}$ substitution shown below.[29,30] TEM images also confirmed that the as-prepared

product is nanocrystalline and exhibits cubic morphology with an average edge length of 7.7 nm ± 1.9 nm in good agreement with the size calculated from the diffraction pattern (see Figure 3.7). The elemental analysis showed a total of 1.03 % Fe content in the nominally 0.5% Fe-doped $SrTiO_3$ NCs (see Figure 3.8 and Table 3.2). The titanium precursor (TALH) also contains small amounts of $TiO_2$ impurities due to slow hydrolysis at pH 8.5. The presence of such impurities thus overestimates the concentration of $Ti^{4+}$ in the reaction solution.

Figure 3.1A shows the electronic absorption spectra and the corresponding color photographs of concentrated solutions of $SrTiO_3$ and Fe:$SrTiO_3$ NCs in hexanes. The absorbance at *ca.* 3.25 eV dominates the electronic absorption spectra of both the samples, consistent with the bandgap transition energy of $SrTiO_3$.[31] Fe:$SrTiO_3$ NCs exhibit an additional broad sub-bandgap absorption that tails into the visible region that is responsible for the yellowish-brown color of the concentrated suspensions (see photographs in Figure 3.1A insets). This absorption tail was previously observed in bulk Fe:$SrTiO_3$ involving deep $Fe^{3+}$ impurity levels and explicitly attributed to a valence band-to-metal charge transfer transition.[32,33]

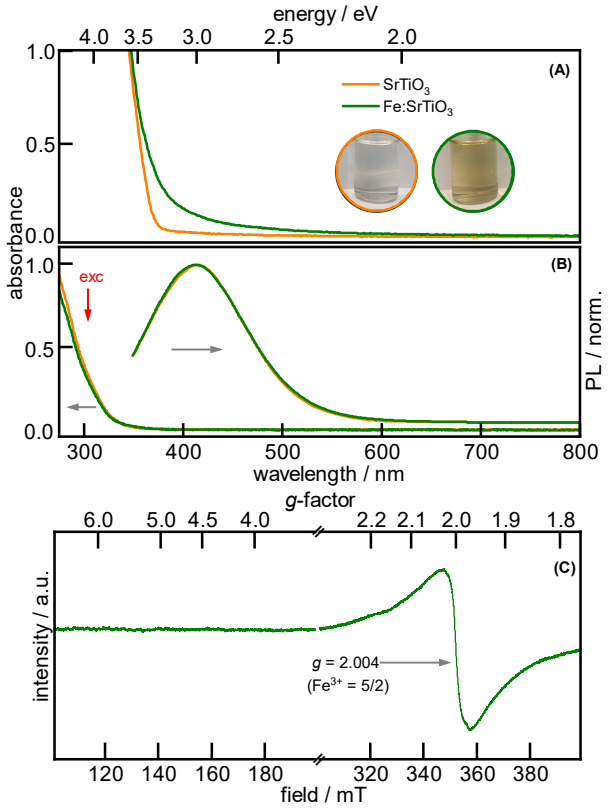


**Figure 3.1** (A) Room temperature electronic absorption spectra and color photographs of concentrated solutions of $SrTiO_3$ (orange) and Fe:$SrTiO_3$ (green) in hexanes. (B) Absorption and PL spectra of dilute solutions of both samples excited at 300 nm. The left axis represents the optical density of dilute solutions that is ≤0.5 at the excitation wavelength, while that normalized PL intensity is displayed on the right axis. (C) Room temperature EPR spectrum of as-prepared Fe:$SrTiO_3$ NCs showing a single, broad resonance at ~350 mT ($g$ = 2.004).

Figure 3.1B displays the electronic absorption and photoluminescence (PL) spectra of dilute suspensions of $SrTiO_3$ and Fe:$SrTiO_3$ NCs excited at 300 nm. The normalized PL spectra of both the samples appear identical, with a broad emission feature centered around ~3.0 eV. This PL energy is in agreement with the previously reported emission described as self-trapped excitons' (STE) recombination at the surface of $SrTiO_3$.[34,35] There is no discernable variance between the PL energy of $SrTiO_3$ and Fe:$SrTiO_3$ NCs. This observation suggests that both the samples possess similar surface chemistry and that radiative recombination from the STE state is faster than the energy transfer to Fe-centered excited states. FTIR measurements

were also utilized on solvent evaporated NCs (see Figure 3.9) to understand the surface coordination environment. The FTIR spectra display the characteristic symmetric and asymmetric carboxylate stretches (doublet at 1540 $cm^{-1}$ and 1450 $cm^{-1}$) and aliphatic bands around 2900 $cm^{-1}$ that are consistent with oleate passivation of the NC surface.

To probe the local environment of $Fe^{3+}$ dopants in as-prepared Fe:$SrTiO_3$ NCs, we employed conventional X-band EPR spectroscopy, which is well-reported to replace octahedral $Ti^{4+}$ in $SrTiO_3$ lattice.[36,37] For $Fe^{3+}$ ($3d^5$) in an environment of cubic symmetry (ground state term $^6A_{1g}$), the spin degeneracy can only be lifted by a magnetic field, thus making $Fe^{3+}$ a suitable dopant for investigation by EPR spectroscopy. Figure 3.1C shows the room temperature EPR spectrum of Fe:$SrTiO_3$ NCs. The broad isotropic resonance at ~350 mT ($g$ = 2.004) corresponds to high-spin $Fe^{3+}$ electronic states at the octahedral site in correspondence with literature.[38-40] No evidence of pseudo-octahedral $Fe^{3+}$ at the $SrTiO_3$ NC surface was detected in the low-field region.

We previously showed that both the spin-lattice ($T_1$) and spin-spin ($T_2$) relaxation times of $Cr^{3+}$ ions in Cr-doped $SrTiO_3$ colloidal NCs could be effectively accelerated by the presence of fast-relaxing paramagnetic $Ti^{3+}$ defects.[25] To probe the interaction between excess electrons and substitutional $Fe^{3+}$, we performed photodoping experiments on Fe:$SrTiO_3$ NCs. A detailed procedure for introducing excess electrons via photodoping is described in the experimental section. Briefly, UV irradiation of an anaerobic solution of as-prepared NCs creates electron/hole pairs

(excitons) followed by the rapid quenching of holes with ethanol which leaves excess electrons in NCs.

Figure 3.2 shows the electronic absorption spectra of Fe:$SrTiO_3$ NCs as a function of photodoping time. The absorption spectrum of as-prepared NCs is dominated by $SrTiO_3$ bandgap transition above ~3.25 eV. With increased photodoping time, a new absorption feature extending throughout the entire visible region and centered at ~1.5 eV (900 nm) appears, and the physical appearance of the sample changes to dark blue (see Figure 2 insets). This broad near-IR transition is assigned to the metal-to-metal charge transfer (MMCT) transition from localized $Ti^{3+}$ sites to the conduction band reported previously in photodoped Cr-doped $SrTiO_3$ and $TiO_2$.[25,41] The only change in the electronic absorption spectrum with increasing photodoping time is the growth of this MMCT transition. We have no evidence that photodoping creates delocalized electrons in the conduction band ($e_{CB}^-$). Recent reports showed that n-type doping of small anatase $TiO_2$ NCs can lead to accumulation of $e_{CB}^-$ as observed spectroscopically by significant blue-shifts in the band-edge energy from the Moss-Burstein effect and formation of a localized surface plasmon resonance (LSPR) in the mid-IR region.[5] Milliron reported similar spectroscopic changes caused by $e_{CB}^-$ accumulation in $Nb^{5+}$-doped $TiO_2$ NCs.[6,42] The lack of absorption in the mid-IR region further confirms that $e_{CB}^-$ are absent in our photodoped $SrTiO_3$ NCs (see Figure 3.10).

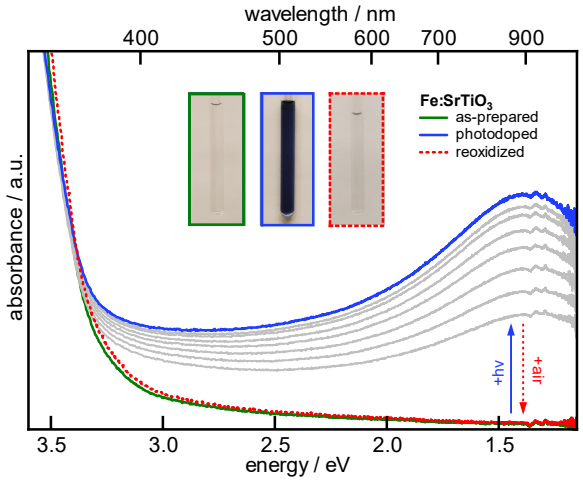


**Figure 3.2** Electronic absorption spectra of an air-free solution of Fe:$SrTiO_3$ NCs in hexanes as a function of photodoping time. The green spectrum corresponds to as-prepared NCs. The intermediate grey lines show the data collected at various stages of photo-irradiation in the presence of EtOH. The blue spectrum belongs to maximally photodoped NCs, and the dotted red line overlapping the as-prepared data represents the reoxidized NCs upon opening the sample to air. The color photographs for as-prepared, photodoped, and reoxidized NCs are shown in insets.

EPR spectroscopy was also utilized to monitor any associated changes in substitutional $Fe^{3+}$ with the concomitant occurrence of $Ti^{3+}$ ($3d^1$, $^2T_{2g}$ ground term) throughout the photodoping duration. Figure 3.3A shows the room temperature EPR spectra of Fe:$SrTiO_3$ NCs collected before and after photodoping. As shown in Figure 3.1C, the EPR spectrum of as-prepared Fe:$SrTiO_3$ NCs (green) exhibits only a single, broad resonance at $g$ = 2.004 assigned to substitutional $Fe^{3+}$ ions. However, after photodoping for 20 min, the $Fe^{3+}$ signal completely disappears, and a new signal at ~355 mT ($g$ = 1.94) is detected that is attributed to the formation of paramagnetic $Ti^{3+}$ consistent with absorption measurements shown in Figure 3.2. The $Ti^{3+}$ EPR signal in photodoped $SrTiO_3$ NCs is nearly isotropic. The disappearance of the $Fe^{3+}$ signal and the simultaneous emergence of $Ti^{3+}$ in the photodoped Fe:$SrTiO_3$ samples are entirely reversible processes. The above-mentioned spectroscopic changes were quantitatively recovered by exposing the photodoped sample to air, as shown by the red dotted spectra in Figures 3.2 and 3.3

These observations are similar to our recent report on $Cr^{3+}$-doped $SrTiO_3$ NCs, where photodoping results in the disappearance of the $Cr^{3+}$ EPR signal at room temperature.[25] The $Cr^{3+}$ signal in that study reappeared after lowering the sample temperature to slow down the accelerated spin-relaxation. However, the EPR spectrum of photodoped Fe:$SrTiO_3$ NCs collected at 100 K (Figure 3.3A) indicates a permanent elimination of $Fe^{3+}$ signal even at the cryogenic temperature. This observation suggests that $Fe^{3+}$ may not have any spin-interactions with $Ti^{3+}$ defects, unlike $Cr^{3+}$ in photodoped $SrTiO_3$ NCs. The change in spin relaxation is caused by the near-resonant cross-relaxation phenomenon between $Ti^{3+}$ and $Cr^{3+}$ with similar *g*-values ($Ti^{3+}$:1.945, $Cr^{3+}$:1.978).[43,44] We speculate that the $Fe^{3+}$ signal at a much higher *g*-value (2.004) can make the spin cross-relaxation process with $Ti^{3+}$ defects non-resonant and, therefore, less effective.

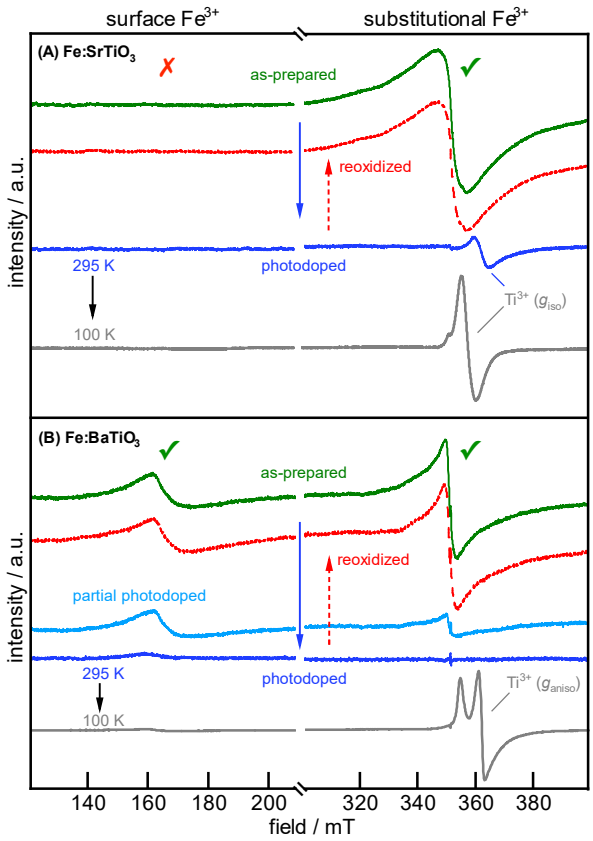


**Figure 3.3** Room-temperature and cryogenic EPR spectra of an air-free solution of (A) Fe:$SrTiO_3$ and (B) Fe:$BaTiO_3$ NCs in hexanes. The green spectra in both samples correspond to as-prepared NCs, and the blue spectra denote the photodoped NCs. The dotted red lines overlapping the as-prepared data represent the reoxidized NCs upon opening the samples to air.

The observation of total disappearance of the $Fe^{3+}$ signal in the $SrTiO_3$ NCs is consistent with at least some, if not all, of the substitutional $Fe^{3+}$ dopants being reduced to EPR-silent $Fe^{2+}$ dopants. This observation is also similar to our recent results on n-type Fe-doped ZnO NCs.[9,45,46] To probe the relative positions of the $Fe^{3+/2+}$ and $Ti^{3+}$ energy levels in $SrTiO_3$ bandgap, we performed *in-situ* photodoping experiments (see SI Figure 3.11). The sequential disappearance of the $Fe^{3+}$ EPR signal within a few seconds of photodoping followed by the appearance of the $Ti^{3+}$ signal suggests (a) there is a gradual rise in Fermi level and (b) that the $Fe^{3+/2+}$ redox level is situated deeper than the $Ti^{3+}$ level. Figure 3.4 illustrates the proposed mechanism of electron trapping in Fe:$SrTiO_3$ NCs. The photoexcitation of charge carriers followed

by rapid hole quenching with EtOH raises the Fermi level below the conduction band, which results in the reduction of substitutional $Fe^{3+}$ to $Fe^{2+}$ prior to self-trapping at the $Ti^{3+}$ defects. Upon exposing the photodoped sample to air, these changes are then reversed, and $Fe^{3+}$ is quantitatively recovered.

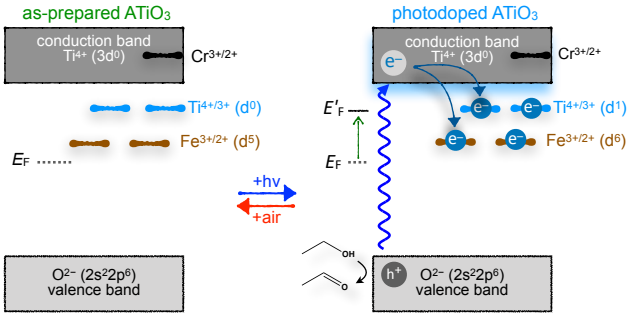


**Figure 3.4** A schematic representation of reversible electron trapping at $Fe^{3+/2+}$ redox level in photodoped Fe:$ATiO_3$ NCs.

To validate the generality of this reversible electron trapping, we extended the study to $Fe^{3+}$-doped $BaTiO_3$ colloidal NCs prepared from a similar hydrothermal method (see SI Figure 3.12 and Table 3.3). Electronic absorption spectra of photodoped NCs of $BaTiO_3$ and Fe:$BaTiO_3$ show a similar but slightly blue-shifted broad absorption feature observed in photodoped $SrTiO_3$ NCs (see SI Figure 3.13). The EPR spectrum of as-prepared Fe:$BaTiO_3$ NCs is shown in Figure 3.3B is similar to the spectrum of Fe:$SrTiO_3$ but also displays an additional intense broad signal at ~160 mT ($g$ = 4.23). This feature increases in relative intensity compared to the substitutional $Fe^{3+}$ signal and is observed in nominally 1% Fe:$SrTiO_3$ NCs (see SI Figure 3.14). This feature at $g$ = 4.23 is attributed to a fraction of $Fe^{3+}$ dopants located near the surface of NCs with pseudo-octahedral symmetry. We attribute the higher relative intensity of this surface $Fe^{3+}$ EPR signal to the smaller size of $BaTiO_3$ (~5 nm) that results in a larger fraction of $Fe^{3+}$ dopants either on the surface or in near-surface sites compared to $SrTiO_3$ NCs (~8 nm). These surface $Fe^{3+}$ sites have variation in the

coordinating ligands on the $SrTiO_3$ and $BaTiO_3$ NC surfaces. The alkylamine surface ligands used during the synthesis of the Fe:$BaTiO_3$ NCs are also known to remove surface $Fe^{3+}$ dopants as observed in a post-synthetic ligand exchange process in $Fe^{3+}$:ZnO NCs.[10]

Further support for the distinction between surface and substitutional $Fe^{3+}$ in the $BaTiO_3$ NCs is based on a comparison of the spectral changes of this low-symmetry surface $Fe^{3+}$ and substitutional $Fe^{3+}$ at $g$ = 2.004 as a function of photodoping time (see Figure 3.3B). Initially, the EPR signal for substitutional $Fe^{3+}$ is more intense than the surface $Fe^{3+}$; however, after photodoping for a short time (~5 min), the relative EPR signal intensities flip. Further photodoping leads to the complete disappearance of the substitutional $Fe^{3+}$ with some residual surface $Fe^{3+}$ signal still observed albeit weaker. The EPR spectrum of the photodoped Fe:$BaTiO_3$ NCs collected at 100 K also shows an anisotropic $Ti^{3+}$ defect signal centered around ~355 mT as shown in Figure 3.3B. The anisotropy of the $g$-values observed for the $Ti^{3+}$-related defect in photodoped colloidal Fe:$BaTiO_3$ NCs presented here ($g_{x,y}$ = 1.94, $g_z$ = 1.97) is exactly opposite to that reported in bulk $BaTiO_3$ powders and single crystals ($g_{x,y}$ = 1.97, $g_z$ = 1.94).[47] Both $SrTiO_3$ and $BaTiO_3$ NCs possess cubic structures by powder XRD. Therefore, the crystal field surrounding a self-trapped electron at the B-site ($Ti^{3+}$) should be isotropic; however, $Ti^{3+}$ is Jahn-Teller active and will distort to axial symmetry in both photodoped $SrTiO_3$ and $BaTiO_3$ albeit to varying extents.[48] The likelihood of $Ti^{3+}$ defects being near or at the NC surface in the smaller $BaTiO_3$ NCs would also lead to distortion of the $Ti^{3+}$ EPR signal due to mixed coordination with the lattice and surface ligands that adds a rhombic component to the $g$-anisotropy.

The anisotropic lineshape is less resolved in the photodoped $SrTiO_3$ and Fe:$SrTiO_3$ NCs and may be the result of the larger average particle size.

The existence of both axial and rhombic EPR signals associated with two distinct $Ti^{3+}$ centers in thermal equilibrium was recently reported in photodoped $TiO_2$ nanoparticles.[49] This observation is unique to photodoped $TiO_2$ nanoparticles and has not been observed in the bulk. We postulate that the variation of the $Ti^{3+}$ EPR signals in photodoped Fe:$SrTiO_3$ and Fe:$SrTiO_3$ NCs compared to the bulk n-type $BaTiO_3$ and Fe:$SrTiO_3$ is caused by differences in (1) the microenvironment surrounding the $Ti^{3+}$ center and (2) its proximity to the NC surface. We are currently investigating the microscopic origins of the EPR signal in photodoped $d^0$ semiconductor NCs. Nevertheless, there is no evidence of $Fe^{3+}$ in photodoped Fe:$BaTiO_3$ NCs, which is consistent with our proposed model of electron trapping on $Fe^{3+}$ in $SrTiO_3$ NCs. The drastic decrease in substitutional $Fe^{3+}$ before surface $Fe^{3+}$ suggests that the former is situated deeper than surface $Fe^{3+/2+}$ redox level in $BaTiO_3$ NCs or that electronic coupling between surface $Fe^{3+}$ and the self-trapped $Ti^{3+}$ defects is weaker. Similar step-wise reductions were also observed in the recent report on n-type $Fe^{3+}$:ZnO NCs containing both substitutional and surface $Fe^{3+}$ species.[9,46] Suzuki *et al*. have reported that the $Fe^{3+/2+}$ redox level is located ~0.7-0.8 eV below the conduction band minimum in $BaTiO_3$ single crystals, while in $SrTiO_3$ the $Fe^{3+/2+}$ level is nearly degenerate with the conduction band.[50] Our results are consistent with the $Fe^{3+/2+}$ energy level lying at a more positive potential than the conduction band and $Ti^{3+}$ level in both $SrTiO_3$ and $BaTiO_3$ NCs.

Several other reports show that at least some of the $Fe^{3+}$ can be reduced to $Fe^{2+}$ in $SrTiO_3$ and $BaTiO_3$ bulk powder and thin films under reducing conditions.[51-53] However, most of these reductions are limited to the surface and sub-surface Fe dopants and typically require elevated temperatures. Stabilization of $Fe^{2+}$ in reduced $SrTiO_3$ and $BaTiO_3$ is also challenging as it requires additional charge compensation that could include the formation of oxygen vacancies.[54] The requirement of oxygen vacancies and effect on the lattice may be responsible for the reduction of only some of the $Fe^{3+}$ dopants in bulk $ATiO_3$. In contrast, the charge compensation during photodoping is accomplished by proton ($H^+$) adsorption at the surfaces, as reported in $TiO_2$ and other oxide NCs.[14,55] Furthermore, photodoping can be achieved at room temperature with just UV photons and a sacrificial hole scavenger. This facile method offers a controlled and reversible reduction of every $Fe^{3+}$ dopant throughout the entire $ATiO_3$ NC.

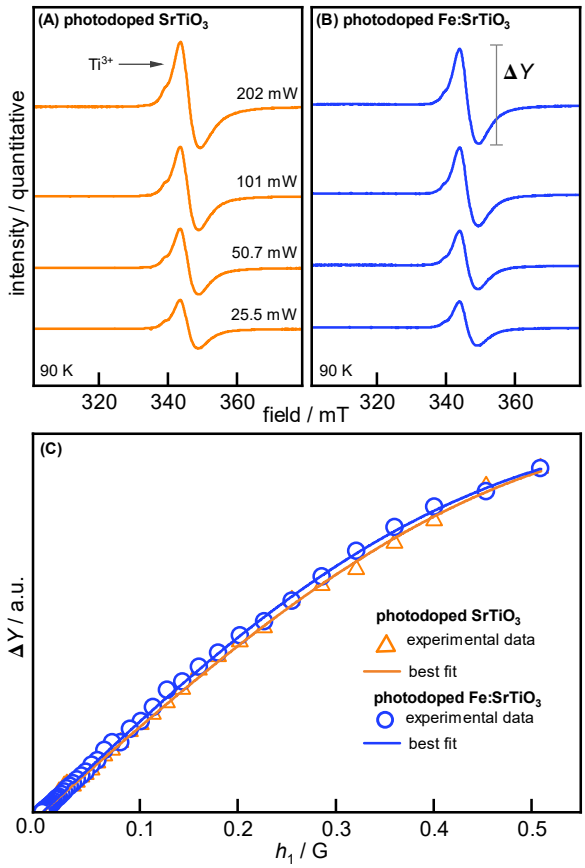


**Figure 3.5** Representative CW-EPR spectra of maximally photodoped (A) $SrTiO_3$ and (B) $Fe:SrTiO_3$ NCs at 90 K at selected microwave powers. The signal intensity defined as ΔY and best fits to equation 3.3 (see Figure 3.16 and Table 3.4) for each measurement plotted as a function of microwave power ($h_1$) is shown in the bottom panel C.

These results provide sufficient evidence that photochemically introduced n-type carriers reduce the $Fe^{3+}$ dopants to EPR-silent $Fe^{2+}$ ions, in contrast to the acceleration of spin-relaxation time of $Cr^{3+}$ dopants.[25] However, they do not rule out the possible cross-relaxation between $Fe^{3+}$ and $Fe^{2+}$ or $Ti^{3+}$ and $Fe^{2+}$ centers in photodoped $ATiO_3$ NCs. High-field EPR measurements to directly observe $Fe^{2+}$ dopants are planned. However, with X-band CW-EPR, we were able to study the effect of $Fe^{2+}$ on $Ti^{3+}$ spin-dynamics. To probe this, we performed power saturation rollover experiments and linewidth analysis of $Ti^{3+}$ signal in the absence and presence of $Fe^{2+}$. These experiments were performed on photodoped $SrTiO_3$ (no $Fe^{2+}$) and $Fe:SrTiO_3$ ($Fe^{3+}$

fully reduced to $Fe^{2+}$) at 90 K (See Figures 3.5A-C, 3.15-3.16 and Table 3.4). No significant difference in saturation rollover behavior or $T_2$ time of the $Ti^{3+}$ defects in both photodoped $SrTiO_3$ (2.65 ± 0.06 ns) and photodoped Fe:$SrTiO_3$ (2.50 ± 0.04 ns) was observed. The slight difference in $T_2$ can be attributed to variation in average $Ti^{3+}$ concentrations in the photodoped NCs. These results suggest that the spin properties of $Ti^{3+}$ defects are not affected by the presence of $Fe^{2+}$ dopants in photodoped $SrTiO_3$ NCs.

### 3.4 Supporting Information

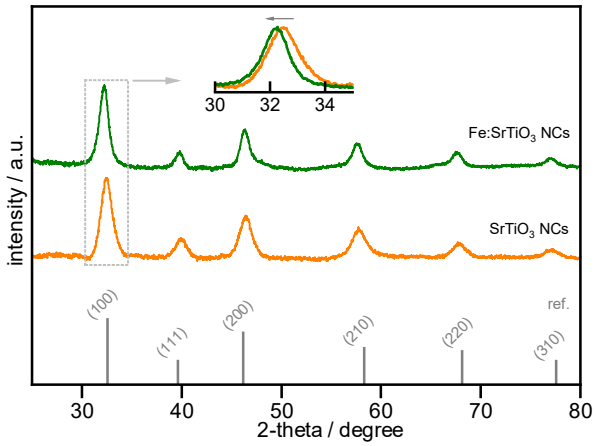


**Figure 3.6** Powder X-ray diffraction pattern of as-prepared $SrTiO_3$ (bottom/black) and Fe:$SrTiO_3$ NCs (top/green) indexed to cubic phase of bulk $SrTiO_3$ with space group of $Pm\bar{3}m$.[56] The baseline was carefully subtracted from both patterns. A slight shift to lower $2\theta$ value in Fe:$SrTiO_3$ NCs displayed in the inset is attributed to a typical lattice expansion due to the incorporation of relatively larger size $Fe^{3+}$ (0.79 Å) cation at cubic $Ti^{4+}$ (0.75 Å) site.

**Table 3.1** The average lattice parameter and crystallite size calculated using Rigaku SmartLab Studio II for both samples.

| Sample NCs | Lattice parameter (Å) | Crystallite size (nm)† |
|---|---|---|
| $SrTiO_3$ | 3.9197 | 5.92 ± 0.42 |
| Fe:$SrTiO_3$ | 3.9256 | 8.02 ± 0.54 |

†Crystallite size is the average size calculated from the three most intense reflections: (110), (200) and (211).

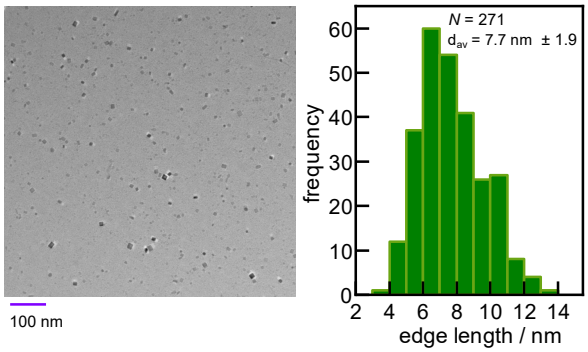


**Figure 3.7** Representative transmission electron microscopy (TEM) image of as-prepared Fe:$SrTiO_3$ NCs deposited on 3 mm copper grid exhibiting a cubic morphology. The size distribution plot from analyzing a few hundred different crystals using ImageJ is shown in the right panel.

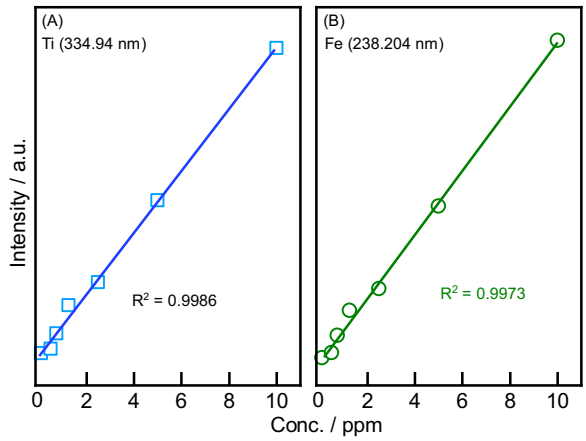


**Figure 3.8** Calibration plots for Ti (left/blue) and Fe (right/green) for ICP-OES measurements using multielement QC-21 Perkin Elmer standard solution to determine percentage in Fe:$SrTiO_3$ NCs. In a typical sample preparation for ICP-OES analysis, solvent-evaporated NCs were digested in aqua regia (~1-2 mL) followed by the dilution in 5% $HNO_3$ solution.

Table 3.2 ICP-OES analysis of Fe content in Fe:$SrTiO_3$ NCs

| Sample NCs | Nominal Fe content (%) | Fe from ICP-OES (%) |
|---|---|---|
| Fe:$SrTiO_3$ | 1.0 | 1.70 |
| Fe:$SrTiO_3$ | 0.5 | 1.03 |

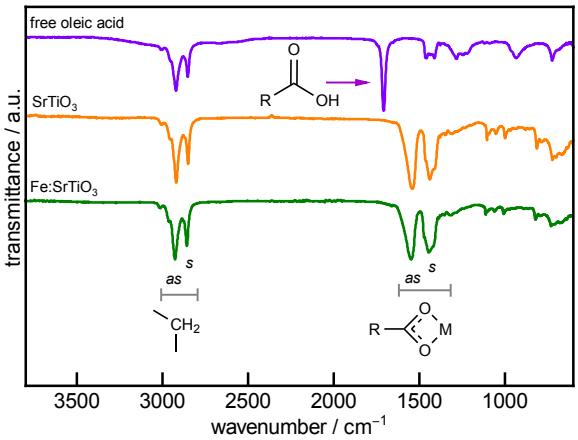


**Figure 3.9** FTIR spectra of solvent evaporated $SrTiO_3$ (orange) and Fe:$SrTiO_3$ (green) NCs. The top purple spectrum belongs to free oleic acid. The pair of peaks at 1450 $cm^{-1}$ and 1550 $cm^{-1}$ corresponding to the symmetric (*s*) and asymmetric (*as*) stretches of bound carboxylate head group of oleate ligand is observed in both NCs. Aliphatic bands of oleate ligands are also present *ca.* 2900 $cm^{-1}$, which indicate the NCs surfaces are passivated by oleate ligands.

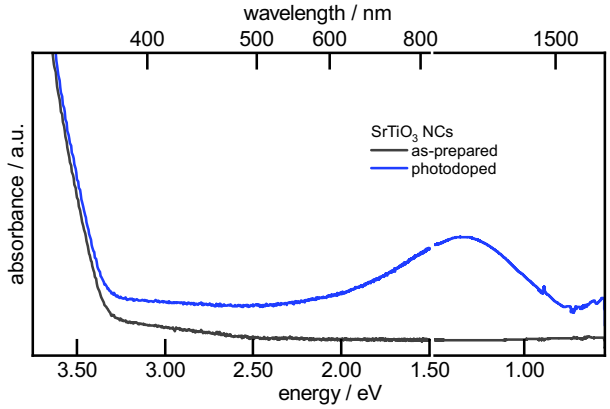


**Figure 3.10** Electronic absorption spectrum of as-prepared and photodoped $SrTiO_3$ NCs. The full spectrum was made by splicing the spectra collected on a Cary 50 for $\lambda < 900$ nm and a Varian 670 for $\lambda > 900$ nm.

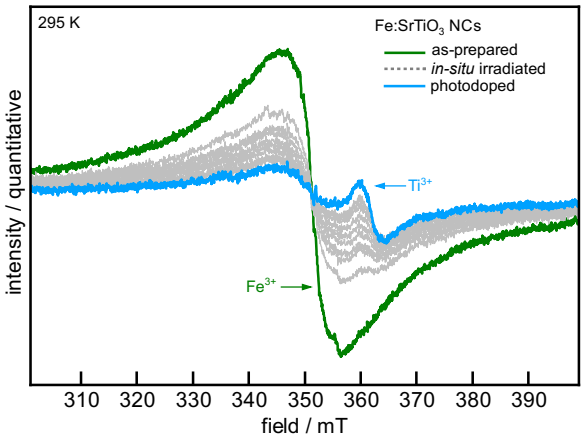


**Figure 3.11** Room temperature in situ EPR spectra of Fe:$SrTiO_3$ NCs as a function of photodoping time. The green spectrum belongs to as-prepared NCs before turning on the Xe lamp. After turning on the lamp, the broad $Fe^{3+}$ signal decreases in intensity and linewidth while a new feature at ~360 mT appears (grey lines). This new signal is assigned to $Ti^{3+}$ defects. The blue spectrum shows the photodoped NCs with some residual $Fe^{3+}$ signal which can be completely eliminated upon prolonged photodoping as discussed in the main paper.

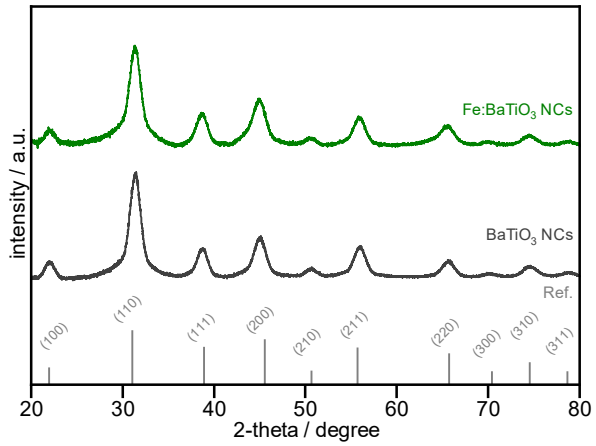


**Figure 3.12** Powder X-ray diffraction pattern of as-prepared $BaTiO_3$ (bottom/black) and Fe:$BaTiO_3$ NCs (top/green) indexed to cubic phase of bulk $BaTiO_3$ with space group of $Pm\bar{3}m$.[57] The average particle size calculated from peak analysis is shown below.

**Table 3.3** The average lattice parameter and crystallite size calculated using Rigaku SmartLab Studio II for both samples.

| Sample NCs | Lattice parameter (Å) | Crystallite size (nm)† |
|---|---|---|
| $BaTiO_3$ | 4.0230 | 6.10 ± 0.4 |
| Fe:$BaTiO_3$ | 4.0523 | 5.04 ± 0.9 |

†Crystallite size is the average size calculated from the three most intense reflections: (110), (200) and (211).

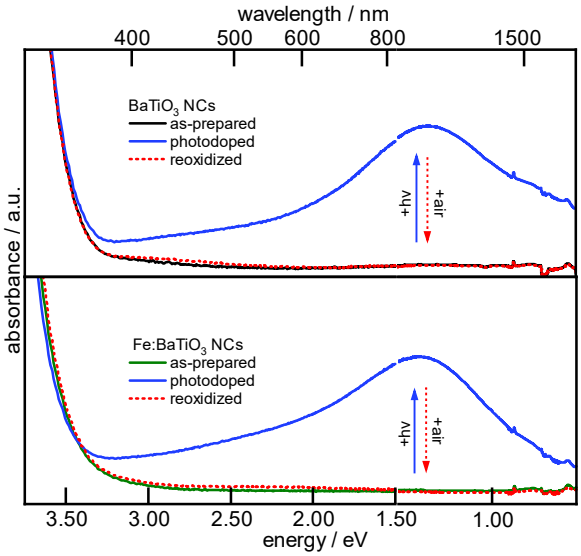


**Figure 3.13** Electronic absorption spectra of an air-free solution of $BaTiO_3$ and Fe:$BaTiO_3$ NCs in hexanes before and after photodoping.

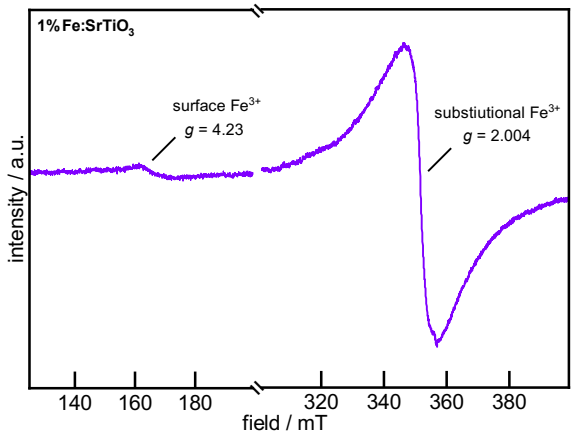


**Figure 3.14** Room temperature EPR spectrum of nominally 1% Fe-doped $SrTiO_3$ NCs.

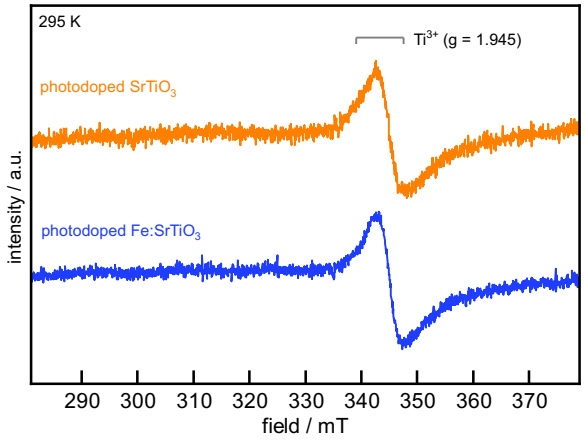


**Figure 3.15** The CW-EPR spectra of collected at room temperature of maximally photodoped $SrTiO_3$ (top/orange) and Fe:$SrTiO_3$ NCs (bottom/blue) displaying the characteristics resonance at $g$ = 1.945 attributed to $Ti^{3+}$ defects. The concentration of NCs in each sample was kept the same, approximated from the combination of ICP-EOS and particle size analysis.

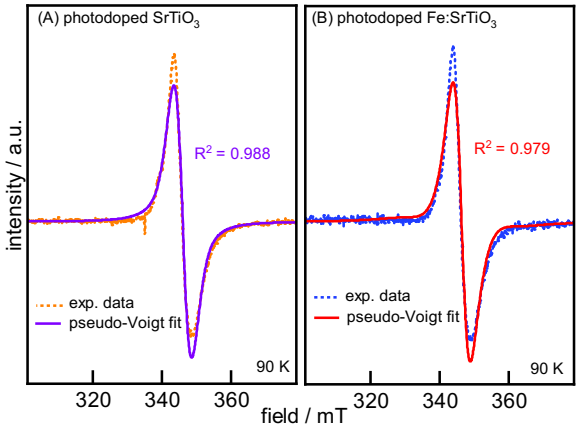


**Figure 3.16** CW-EPR spectra collected well below the saturation power at 90 K of (A) photodoped $SrTiO_3$ and (B) photodoped Fe:$SrTiO_3$ NCs. The purple and red lines are best fits to pseudo-Voigt line profile in origin (Equation 3.1) to obtain the Lorentzian width ($\Gamma_L$) to calculate the spin-spin relaxation time ($T_2$) using equation 3.2.

y0+(-Ag*((x-x0)/(Wg^2))*exp(-0.5*((x-x0)/Wg)^2))+(-2*Al*(x-x0))/((Wl^2)*(1+((x-x0)/Wl)^2)^2) (eq. 3.1)

$$T_2 = 2/(\gamma_e \Gamma_L) \quad \text{(eq. 3.2)}$$

Where $\gamma$ is the electron gyromagnetic ratio ($1.760859708 \times 10^{11}$ $s^{-1}T^{-1}$).

Equation 3.3 shown below was used to fit the power saturation data shown in Figures 4A-C in the main text to determine the term $P_2$ which is the product of the spin-lattice ($1/T_1$) and spin-spin relaxation rate ($1/T_2$) as shown in equation 3.4. Where c is a scaler and ε is a measure of line homogeneity.

$$\Delta Y = c \cdot h_1 \left(1 + \frac{(h_1)^2}{P_2}\right)^{-\varepsilon} \qquad \text{(eq. 3.3)}$$

$$P_2 = (\gamma_e^2 T_1 T_2)^{-1} \qquad \text{(eq. 3.4)}$$

**Table 3.4** Spin-spin relaxation time ($T_2$) calculated from Lorentzian width ($\Gamma_L$) from fitting EPR spectra of both samples to first derivative pseudo-Voigt line profile as displayed in figure 3.16.

| Sample NCs | $\Gamma_L$ (G) | $T_2$ (ns) |
|---|---|---|
| $SrTiO_3$ | 42.88 ± 1.11 | 2.65 ± 0.06 |
| Fe:$SrTiO_3$ | 45.75 ± 0.62 | 2.50 ± 0.04 |

## 3.5 References


(1) Mocatta, D.; Cohen, G.; Schattner, J.; Millo, O.; Rabani, E.; Banin, U. Heavily doped semiconductor nanocrystal quantum dots. *Science* **2011,** *332* (6025), 77-81.

(2) Queisser, H. J.; Haller, E. E. Defects in semiconductors: some fatal, some vital. *Science* **1998,** *281* (5379), 945-950.

(3) Ohno, H. A window on the future of spintronics. *Nat. Mater.* **2010,** *9* (12), 952-954.

(4) Han, W.; Kawakami, R. K.; Gmitra, M.; Fabian, J. Graphene spintronics. *Nat. Nanotech.* **2014,** *9* (10), 794-807.

(5) Cao, S.; Zhang, S.; Zhang, T.; Fisher, A.; Lee, J. Y. Metal-doped $TiO_2$ colloidal nanocrystals with broadly tunable plasmon resonance absorption. *J. Mater. Chem. C* **2018,** *6* (15), 4007-4014.

(6) De Trizio, L.; Buonsanti, R.; Schimpf, A. M.; Llordes, A.; Gamelin, D. R.; Simonutti, R.; Milliron, D. J. Nb-doped colloidal $TiO_2$ nanocrystals with tunable infrared absorption. *Chem. Mater.* **2013,** *25* (16), 3383-3390.

(7) Shah, J.; Kotnala, R. K. Induced magnetism and magnetoelectric coupling in ferroelectric $BaTiO_3$ by Cr-doping synthesized by a facile chemical route. *J. Mater. Chem. A* **2013,** *1* (30), 8601-8608.

(8) Norberg, N. S.; Kittilstved, K. R.; Amonette, J. E.; Kukkadapu, R. K.; Schwartz, D. A.; Gamelin, D. R. Synthesis of colloidal $Mn^{2+}$: ZnO quantum dots and high-$T_C$ ferromagnetic nanocrystalline thin films. *J. Am. Chem. Soc.* **2004,** *126* (30), 9387-9398.

(9) Buz, E.; Zhou, D. M.; Kittilstved, K. R. Air-stable n-type Fe-doped ZnO colloidal nanocrystals. *J. Chem. Phys.* **2019,** *151* (13), 134702.

(10) Zhou, D.; Kittilstved, K. R. Control over $Fe^{3+}$ speciation in colloidal ZnO nanocrystals. *J. Mater. Chem. C* **2015,** *3* (17), 4352-4358.

(11) Luther, J. M.; Jain, P. K.; Ewers, T.; Alivisatos, A. P. Localized surface plasmon resonances arising from free carriers in doped quantum dots. *Nat. Mater.* **2011,** *10* (5), 361-366.

(12) Manthiram, K.; Alivisatos, A. P. Tunable localized surface plasmon resonances in tungsten oxide nanocrystals. *J. Am. Chem. Soc.* **2012,** *134* (9), 3995-3998.

(13) Liu, W. K.; Whitaker, K. M.; Kittilstved, K. R.; Gamelin, D. R. Stable photogenerated carriers in magnetic semiconductor nanocrystals. *J. Am. Chem. Soc.* **2006,** *128* (12), 3910-3911.

(14) Schimpf, A. M.; Gunthardt, C. E.; Rinehart, J. D.; Mayer, J. M.; Gamelin, D. R. Controlling carrier densities in photochemically reduced colloidal ZnO nanocrystals: size dependence and role of the hole quencher. *J. Am. Chem. Soc.* **2013,** *135* (44), 16569-16577.

(15) Lehuta, K. A.; Kittilstved, K. R. Reversible control of the chromium valence in chemically reduced Cr-doped $SrTiO_3$ bulk powders. *Dalton Trans.* **2016,** *45* (24), 10034-10041.

(16) Wang, C.; Shim, M.; Guyot-Sionnest, P. Electrochromic nanocrystal quantum dots. *Science* **2001,** *291* (5512), 2390-2392.

(17) Karmakar, D.; Mandal, S.; Kadam, R.; Paulose, P.; Rajarajan, A.; Nath, T. K.; Das, A. K.; Dasgupta, I.; Das, G. Ferromagnetism in Fe-doped ZnO nanocrystals: experiment and theory. *Phys. Rev. B* **2007,** *75* (14), 144404.

(18) Soledade, L.; Longo, E.; Leite, E.; Pontes, F.; Lanciotti Jr, F.; Campos, C.; Pizani, P.; Varela, J. A. Room-temperature photoluminescence in amorphous $SrTiO_3$–the influence of acceptor-type dopants. *Appl. Phys. A* **2002,** *75* (5), 629-632.

(19) Eror, N.; Balachandran, U. High-temperature defect structure of acceptor-doped strontium titanate. *J. Am. Ceram. Soc.* **1982,** *65* (9), 426-431.

(20) Mansoor, H.; Harrigan, W. L.; Lehuta, K. A.; Kittilstved, K. R. Reversible Control of the Mn Oxidation State in $SrTiO_3$ Bulk Powders. *Front. Chem.* **2019,** *7*, 353.

(21) Kaspar, T. C.; Droubay, T.; Shutthanandan, V.; Heald, S. M.; Wang, C. M.; McCready, D. E.; Thevuthasan, S.; Bryan, J.; Gamelin, D. R.; Kellock, A. Ferromagnetism and structure of epitaxial Cr-doped anatase $TiO_2$ thin films. *Phys. Rev. B* **2006,** *73* (15), 155327.

(22) Matsumoto, Y.; Murakami, M.; Shono, T.; Hasegawa, T.; Fukumura, T.; Kawasaki, M.; Ahmet, P.; Chikyow, T.; Koshihara, S.-y.; Koinuma, H. Room-temperature ferromagnetism in transparent transition metal-doped titanium dioxide. *Science* **2001,** *291* (5505), 854-856.

(23) Pei, Y.; Zhang, R.; Song, Y.; Bi, J.; Xu, W.; Zhou, C.; Duan, J.; Yang, J.; Cao, Y. Emergent magnetic phase transitions in Fe-doped $SrTiO_{3-\delta}$. *AIP Adv.* **2019,** *9* (12), 125302.

(24) Fix, T.; Liberati, M.; Aubriet, H.; Sahonta, S.; Bali, R.; Becker, C.; Ruch, D.; MacManus-Driscoll, J.; Arenholz, E.; Blamire, M. Ferromagnetism in Co-doped (La,Sr)$TiO_3$. *New J. Phys.* **2009,** *11* (7), 073042.

(25) Harrigan, W. L.; Kittilstved, K. R. Reversible modulation of the $Cr^{3+}$ spin dynamics in colloidal $SrTiO_3$ nanocrystals. *J. Phys. Chem. C* **2018,** *122* (46), 26652-26657.

(26) Harrigan, W. L.; Michaud, S. E.; Lehuta, K. A.; Kittilstved, K. R. Tunable electronic structure and surface defects in chromium-doped colloidal $SrTiO_{3-\delta}$ nanocrystals. *Chem. Mater.* **2016,** *28* (2), 430-433.

(27) Abdullah, M.; Nelson, R. J.; Kittilstved, K. R. On the formation of superoxide radicals on colloidal $ATiO_3$ (A= Sr and Ba) nanocrystal surfaces. *Nanoscale Adv.* **2020,** *2*, 1949-1955.

(28) Mitchell, R.; Chakhmouradian, A.; Woodward, P. Crystal chemistry of perovskite-type compounds in the tausonite-loparite series,$(Sr_{1-2x}Na_xLa_x)TiO_3$. *Phys. Chem. Miner.* **2000,** *27* (8), 583-589.

(29) Shannon, R. D. Revised effective ionic radii and systematic studies of interatomic distances in halides and chalcogenides. *Acta Crystallogr.* **1976,** *32* (5), 751-767.

(30) Drahus, M. D.; Jakes, P.; Erdem, E.; Eichel, R.-A. Defect structure of the mixed ionic electronic conducting $Sr[Ti,Fe]O_x$ solid solution system-change in iron oxidation states and defect complexation. *Solid State Ionics* **2011,** *184* (1), 47-51.

(31) Noland, J. A. Optical absorption of single-crystal strontium titanate. *Phys. Rev.* **1954,** *94* (3), 724-724.

(32) Morin, F.; Oliver, J. Energy levels of iron and aluminum in $SrTiO_3$. *Phys. Rev. B* **1973,** *8* (12), 5847-5854.

(33) Berney, R.; Cowan, D. Photochromism of three photosensitive Fe centers in $SrTiO_3$. *Phys. Rev. B* **1981,** *23* (1), 37-50.

(34) Leonelli, R.; Brebner, J. Time-resolved spectroscopy of the visible emission band in strontium titanate. *Phys. Rev. B* **1986,** *33* (12), 8649-8656.

(35) Kan, D. S.; Terashima, T.; Kanda, R.; Masuno, A.; Tanaka, K.; Chu, S. C.; Kan, H.; Ishizumi, A.; Kanemitsu, Y.; Shimakawa, Y.; Takano, M. Blue-light emission at room temperature from $Ar^+$-irradiated $SrTiO_3$. *Nat. Mater.* **2005,** *4* (11), 816-819.

(36) Zhang, Q.; Huang, Y.; Peng, S.; Huang, T.; Cao, J.-j.; Ho, W.; Lee, S. Synthesis of $SrFe_xTi_{1-x}O_{3-\delta}$ nanocubes with tunable oxygen vacancies for selective and efficient photocatalytic NO oxidation. *Appl. Catal., B* **2018,** *239*, 1-9.

(37) Muller, K. Paramagnetische Resonanz von $Fe^{3+}$ in $SrTiO_3$-Einkristallen. *Helv. Phys. Acta* **1958,** *31*, 173-204.

(38) Faughnan, B.; Kiss, Z. Optical and EPR studies of photochromic $SrTiO_3$ doped with Fe/Mo and Ni/Mo. *IEEE J. Quantum Electron.* **1969,** *5* (1), 17-21.

(39) Merkle, R.; Maier, J. Defect association in acceptor-doped $SrTiO_3$: case study for $Fe'_{Ti}V_O$ and $Mn''_{Ti}V_O^{\cdot\cdot}O$. *Phys. Chem. Chem. Phys.* **2003,** *5* (11), 2297-2303.

(40) Lenser, C.; Kalinko, A.; Kuzmin, A.; Berzins, D.; Purans, J.; Szot, K.; Waser, R.; Dittmann, R. Spectroscopic study of the electric field induced valence change of Fe-defect centers in $SrTiO_3$. *Phys. Chem. Chem. Phys.* **2011,** *13* (46), 20779-20786.

(41) Joost, U.; Šutka, A.; Oja, M.; Smits, K.; Döbelin, N.; Loot, A.; Järvekülg, M.; Hirsimäki, M.; Valden, M.; Nõmmiste, E. Reversible photodoping of $TiO_2$ nanoparticles for photochromic applications. *Chem. Mater.* **2018,** *30* (24), 8968-8974.

(42) Dahlman, C. J.; Agrawal, A.; Staller, C. M.; Adair, J.; Milliron, D. J. Anisotropic Origins of Localized Surface Plasmon Resonance in n-Type Anatase $TiO_2$ Nanocrystals. *Chem. Mater.* **2019,** *31* (2), 502-511.

(43) Nisida, Y. Spin-lattice relaxation of $Cr^{3+}$ in coexistence with $Ti^{3+}$ in $Al_2O_3$. *J. Phys. Soc. Japan* **1965,** *20* (8), 1390-1399.

(44) Dionne, G. F. Spin-Lattice relaxation of $Ti^{3+}$ ions in $RbAl(SO_4)_2{\cdot}12H_2O$. *Phys. Rev.* **1965,** *139* (5A), A1648.

(45) Brozek, C. K.; Zhou, D.; Liu, H.; Li, X.; Kittilstved, K. R.; Gamelin, D. R. Soluble supercapacitors: large and reversible charge storage in colloidal iron-doped ZnO nanocrystals. *Nano Lett.* **2018,** *18* (5), 3297-3302.

(46) Zhou, D.; Kittilstved, K. R. Electron trapping on $Fe^{3+}$ sites in photodoped ZnO colloidal nanocrystals. *Chem. Commun.* **2016,** *52* (58), 9101-9104.

(47) Schrader, M.; Mienert, D.; Oh, T.-S.; Yoo, H.-I.; Becker, K. D. An optical, EPR and electrical conductivity study of blue barium titanate, $BaTiO_{3-\delta}$. *Solid State Sci.* **2008,** *10* (6), 768-775.

(48) Bersuker, I. B.; Polinger, V. Perovskite Crystals: Unique Pseudo-Jahn–Teller Origin of Ferroelectricity, Multiferroicity, Permittivity, Flexoelectricity, and Polar Nanoregions. *Condens. Matter* **2020,** *5* (4), 68.

(49) Peper, J. L.; Vinyard, D. J.; Brudvig, G. W.; Mayer, J. M. Slow Equilibration between Spectroscopically Distinct Trap States in Reduced $TiO_2$ Nanoparticles. *J. Am. Chem. Soc.* **2017,** *139* (8), 2868-2871.

(50) Suzuki, I.; Gura, L.; Klein, A. The energy level of the $Fe^{2+/3+}$ transition in $BaTiO_3$ and $SrTiO_3$ single crystals. *Phys. Chem. Chem. Phys.* **2019,** *21* (11), 6238-6246.

(51) Wechsler, B.; Klein, M. B. Thermodynamic point defect model of barium titanate and application to the photorefractive effect. *J. Opt. Soc. Am. B* **1988,** *5* (8), 1711-1723.

(52) Koehl, A.; Kajewski, D.; Kubacki, J.; Lenser, C.; Dittmann, R.; Meuffels, P.; Szot, K.; Waser, R.; Szade, J. Detection of $Fe^{2+}$ valence states in Fe doped $SrTiO_3$ epitaxial thin films grown by pulsed laser deposition. *Phys. Chem. Chem. Phys.* **2013,** *15* (21), 8311-8317.

(53) Kubacki, J.; Kajewski, D.; Koehl, A.; Lenser, C.; Dittmann, R.; Szade, J. X‐ray absorption and resonant photoemission studies of electroforming process in Fe‐doped $SrTiO_3$ epitaxial films. *X-Ray Spectrometry* **2015,** *44* (5), 339-343.

(54) Comes, R. B.; Kaspar, T. C.; Heald, S. M.; Bowden, M. E.; Chambers, S. A. Infrared optical absorption in low-spin $Fe^{2+}$-doped $SrTiO_3$. *J. Phys. Cond. Matter* **2016,** *28* (3), 035901.

(55) Schrauben, J. N.; Hayoun, R.; Valdez, C. N.; Braten, M.; Fridley, L.; Mayer, J. M. Titanium and zinc oxide nanoparticles are proton-coupled electron transfer agents. *Science* **2012,** *336* (6086), 1298-1301.

(56) Mitchell, R.; Chakhmouradian, A.; Woodward, P. Crystal chemistry of perovskite-type compounds in the tausonite-loparite series,$(Sr_{1-2x}Na_x\ La_x)TiO_3$. *Phys. Chem. Miner.* **2000,** *27* (8), 583-589.

(57) Kwei, G.; Lawson, A.; Billinge, S.; Cheong, S.-W. Structures of the ferroelectric phases of barium titanate. *J. Phys. Chem.* **1993,** *97* (10), 2368-2377.

# CHAPTER 4

# CONTROLLING THE VALENCE STATE OF IRON DOPANTS IN COLLOIDAL TITANIUM DIOXIDE NANOCRYSTALS

## 4.1 Introduction

The intentional incorporation of impurities or dopants in semiconductors is fundamental to manipulate the properties that render them useful for various applications.[1] The example of such impurities in semiconductors includes the magnetic dopants such as $Mn^{2+}$ and $Ni^{2+}$ in ZnO to activate the room temperature ferromagnetism for their potential use in spin-based applications[2,3] and the Cr dopants in $TiO_2$ to improve its optical properties.[4] The changes in the electronic structure of semiconductors are very sensitive to the individual dopants properties such as the energy level alignment, oxidation states, and their speciation within the host lattices. As an example, the substitution of $Al^{3+}$ in ZnO acts as an n-type dopant while the same dopant produces p-type carriers in $SnO_2$.[5,6]

Our understanding of the dopant-induced properties particularly in free-standing nanoscale semiconductors is incomplete because of the unavailability of robust synthetic methods to prepare doped nanocrystals and their complicated surface and defect chemistries.[7] Moreover, many of the transition metal dopants exist in multiple oxidation states within the host lattices.[8,9] The origin of the dopant-induced properties oftentimes remains elusive as each oxidation state imparts unique changes to the electronic structure. For example, the correlation between the mixed-oxidation states of redox-active dopants such as $Mn^{3+/2+}$ and $Fe^{3+/2+}$ and the room temperature ferromagnetic ordering in oxide lattices has been a long-standing

debate.[10-12] Controlling the properties of individual dopants within the host lattice is, therefore, a key to understand the underlying mechanisms for the dopant-induced changes in semiconductors.

In our recent report, we demonstrated that the oxidation state of Fe dopants in $SrTiO_3$ and $BaTiO_3$ nanocrystals (NCs) can be reversibly modulated between $Fe^{3+}$ and $Fe^{2+}$ using a photodoping method.[13] However, these changes in the dopant oxidation state required EtOH as sacrificial reductant and UV photons under extremely inert conditions. The traces of air can make the photodoping process completely ineffective. Here, we present an alternative method to control the oxidation state of Fe dopants in $TiO_2$ NCs under ambient conditions without requiring any sacrificial reductant or UV photons. We prepared and characterized $Fe^{3+}$-doped $TiO_2$ colloidal NCs using a solvothermal method. The spectroscopic analysis shows that $Fe^{3+}$ dopant is substituted at $Ti^{4+}$ site in as-prepared NCs. The introduction of excess electrons using the photodoping method in as-prepared NCs shows a reversible electron trapping at $Fe^{3+}$ dopants converting it into $Fe^{2+}$. This observation consistent with our previous report on Ti-based oxide NCs[13] helped to build the electronic structure of Fe-doped $TiO_2$ NCs. We further extended this work to incorporate the air-table excess electrons by co-doping the NCs with aliovalent $Nb^{5+}$ dopants. The substitutional $Nb^{5+}$ dopants add n-type carriers in the $TiO_2$ NCs which are stable under the ambient condition as confirmed through electronic absorption and electron paramagnetic resonance (EPR) spectroscopies. The presence of n-type carriers is correlated with the complete disappearance of $Fe^{3+}$-related EPR signal that we attribute to the reduction of $Fe^{3+}$ to EPR-silent $Fe^{2+}$.

## 4.2 Experimental

### 4.2.1 Materials

Titanium(iv) *n*-butoxide ($Ti(OBu)_4$, 99%, Acros Organics), oleylamine (>50%, TCI America), oleic acid (>95%, Fisher Chemical), iron nitrate nonahydrate ($Fe(NO_3)_3 \cdot 9H_2O$, 99.99% Sigma Aldrich), niobium(v) chloride ($NbCl_5$, 99.95%, Alfa Aesar), ethanol (200 proof, PHARMCO-AAPER), QC standard, 21 elements (5% $HNO_3$, PerkinElmer), nitric acid (Certified ACS Plus – Safe Cote, Fisher Chemical), hydrochloric acid (Certified ACS Plus, Fisher Chemical), toluene (optima, Fisher Chemicals) and hexanes (optima, Fisher Chemicals) were all used as received.

### 4.2.2 Synthesis of Nanocrystals

The synthesis of colloidal $TiO_2$ NCs was carried out by a solvothermal method. In a typical preparation, 1.5 mmol of $Ti(OBu)_4$ was mixed with 7.5 mmol of oleic acid and 7.5 mmol of oleylamine in 6 mL of 99% EtOH in water (v/v). The obtained mixture was then transferred to a 45 mL Teflon-lined autoclave and heated to 200 °C for 18 h. After the synthesis, the autoclave was cooled down to room temperature and the solid product was collected, washed with ethanol several times, and suspended in non-polar solvents such as toluene to produce a turbid solution. Finally, a transparent layer containing NCs was extracted by centrifuging (5 min at 4000 rpm) the cloudy solution. The synthesis of nominally 0.2% Fe-doped $TiO_2$ NCs was carried out by adding 30 µL of 0.1 M aqueous solution of the $Fe(NO_3)_3$. Similarly, for the preparation of 8% Nb-doped $TiO_2$ NCs, 32 mg of $NbCl_5$ was added before closing the autoclave.

### 4.2.3 Physical Characterization

All measurements presented below were collected on either undoped or 0.2% Fe-doped $TiO_2$ NCs at room temperature unless specified otherwise. Electronic

absorption and emission spectra were collected at room temperature on colloidal NCs in an air-tight quartz cuvette on a Cary 50 Bio and Cary Eclipse, respectively. Near-IR absorption measurements were collected on a Varian 670 FT spectrometer equipped with an InGaAs detector and near-IR quartz beam splitter using a 1-mm pathlength quartz cuvette. The functional groups and surface chemistry analysis of solvent-free NCs were carried out on a Bruker Alpha-P Fourier transform infrared (FTIR) spectrophotometer equipped with an attenuated total reflectance (ATR) platinum diamond optic. EPR measurements were carried out on a continuous wave (CW) Bruker Elexsys-500 fitted with Super High QE X-band cavity (ER4123SHQE) and cryostat (ESR-900, Oxford) for low-temperature measurements. For the photodoping experiments, a 75 W xenon lamp was used (60000 Q series, Oriel Corporation). Transmission electron microscopy (TEM, JEOL 2000FX) images were measured from freshly prepared NCs drop-casted onto carbon-coated (3nm) copper grids (CF400-CU-50, Electron Microscopy Sciences). The average size distribution and standard deviation were generated by analyzing a few hundred particles from TEM images using ImageJ software. Powder X-ray diffraction patterns were collected in a Bragg-Brentano configuration and Cu K- source (Rigaku Smart Lab SE). Metal ion stoichiometry was measured on dissolved ensembles of NCs and measured by inductively coupled plasma-optical emission spectrometry (ICP-OES, Perkin Elmer Optima 4300 DV).

**4.3 Results and Discussion**

The synthesis of nominally 0.2% Fe-doped $TiO_2$ NCs (to referred as Fe:$TiO_2$ hereafter) was carried out using a solvothermal method by modifying a literature

procedure[14] as described in experimental section. This synthesis employs water vapor to hydrolyze the $Ti(OBu)_4$ precursor over 24 h that allows the successful dopant incorporation. The as-prepared NCs are soluble in non-polar solvents such as toluene to produce a transparent colloidal solution. The powder X-ray diffraction (PXRD) pattern of the as-prepared product is indexed to anatase crystal structure of $TiO_2$ ($I4_1/amd$) with no detectable secondary phases (see SI Figure 4.5).[15] The small increase in the lattice parameters of Fe:$TiO_2$ compared to undoped $TiO_2$ NCs (see SI Table 4.1) is attributed to the substitution of a larger size $Fe^{3+}$ (0.79 Å) dopants at $Ti^{4+}$ (0.74 Å) sites consistent with other spectroscopic evidence discussed below.[16] The TEM images of $TiO_2$ and Fe:$TiO_2$ NCs (see SI Figures 4.6 and 4.7) show an average size of 10.4 ±2.2 and 7.45 ±1.5 nm, respectively. The size of NCs measured from TEM images agrees well with the crystallite size calculated from PXRD analysis shown in Table 4.1.

The electronic absorption spectra of as-prepared $TiO_2$ (black) and Fe:$TiO_2$ NCs (green) are shown in Figure 4.1A-B. Both samples are dominated with the bandgap absorption above ~3.25 eV consistent with bandgap energy of single crystal of $TiO_2$.[17] However, Fe:$TiO_2$ NCs show an absorption smearing out of the band edge. This absorption feature has been previously observed in Fe-doped $TiO_2$ nanoparticles and is assigned to the charge transfer transitions from the valence band to the $Fe^{3+}$ impurity levels located below the conduction band.[18] To probe the local environment of $Fe^{3+}$ dopants in $TiO_2$, we employed the X-band EPR spectroscopy. The room temperature EPR spectrum of as-prepared Fe:$TiO_2$ NCs shown in Figure 4.2 (green) displays a broad anisotropic signal centered around 350 mT. Although the shape and

the $g$-value for this EPR signal agree with the substitutional $Fe^{3+}$ dopants in anatase,[19-22] we observe much resolved features spread around the central peak at $g$-value = 1.992. To confirm the identity of all these features, we simulated the EPR spectrum of $Fe^{3+}$ ($S = 5/2$) in $TiO_2$ with both the axial ($D$) and rhombic ($E$) components to the zero-field splitting (ZFS) using the spin-Hamiltonian (eq. 4.1) shown below in EasySpin software.

$$H = \boldsymbol{g}\beta BS + \boldsymbol{D}\left(\hat{S}_z^2 - \frac{1}{3}(S^2 + S)\right) + \boldsymbol{E}\left(\hat{S}_x^2 - \hat{S}_y^2\right) + \sum_k \sum_{q=-k}^{k} B_k^q O_k^q \qquad \text{(eq. 4.1)}$$

where $g$ is the Landé $g$-factor, $\beta$ is the Bohr magneton and $B$ represents the applied magnetic field. The last term in the equation represents the fine structure parameters ($a$ and $F$). With the initial parameters for Fe-doped $TiO_2$ taken from the literature,[23] the simulated spectrum is displayed as a pink dotted line in Figure 4.2. A good agreement between experimental and simulated EPR spectrum identifies this broad signal including the satellite features spanning through 300-400 mT as a substitutional $Fe^{3+}$ dopant with prominent axial ZFS ($D$ = 151.758 x $10^{-4}$ $cm^{-1}$) and a negligible rhombic anisotropy ($E$ = 7.35 x $10^{-10}$ $cm^{-1}$). The fine structures around the central peak are originating from cubic parameters $a$ (−63.5026 MHz) and $F$ (−529.5953 MHz). No evidence of surface $Fe^{3+}$ species was detected in the low-field region of EPR spectrum collected on a few different samples (see SI Figure 4.8).

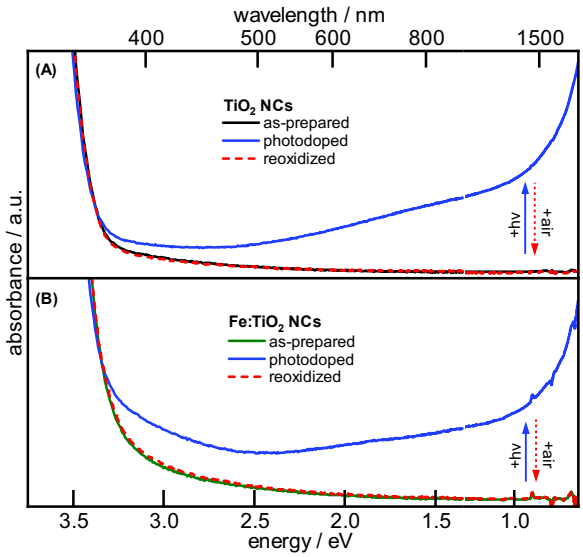


**Figure 4.1** Electronic absorption spectra of (A) $TiO_2$ and (B) Fe:$TiO_2$ NCs before and after the photodoping. The full absorption spectra were generated by splicing the data collected on a Cary 50 for energy > 1.2 eV and a Varian 670 for energy < 1.2 eV.

To probe the effect of excess electrons on the substitutional $Fe^{3+}$ dopants, photodoping of as-prepared samples was performed. The detailed procedure for the photodoping experiments is adopted from our previous report.[13] Briefly, UV irradiation of air-free solution of NCs creates electron-hole pairs. The rapid hole quenching with EtOH as a sacrificial reductant leaves excess electrons in the NCs. The electronic absorption spectra displayed in Figure 4.1A-B show the appearance of a broad absorption feature tailing through the band-edge with photodoping both $TiO_2$ and Fe:$TiO_2$ NCs. This characteristic broad absorption that maximizes in the mid-IR along with the deep blue coloration of photodoped samples (see SI Figure 4.9) has been previously observed in n-type $TiO_2$ nanoparticles and is attributed to the localized surface plasmon resonance (LSPR).[24,25] A clear blue-shift in the band-edge absorption with photodoping due to the Moss-Burstein effect is also indicative of the free electrons in the conduction band ($e^-_{CB}$). It is worth noticing that in addition to the LSPR-related broad absorption, a weak feature around ~1.75 eV (800 nm) also

appears with the photodoping. The energy of this feature is consistent with the trapped electrons at $Ti^{3+}$ sites as reported by Mayer and co-workers in photodoped $TiO_2$ amorphous nanoparticles.[26] The amorphous $TiO_2$ does not have any well-defined bands. Therefore, added electrons did not produce any free electrons or surface plasmon but $Ti^{3+}$ trap sites in photodoped TiO2 nanoparticles in that study. However, $TiO_2$ employed in current work is phase pure crystalline anatase and possess well-defined valence and conduction band as depicted from band edge absorption. Valentin et al., found that quasi-localized or localized $Ti^{3+}$ states in crystalline n-type $TiO_2$ thin films are very close in energy (~0.1 eV) to the delocalized electrons that can be thermally excited to the conduction band.[27] We speculate that a fraction of electrons in photodoped NCs creates thermally-detrapped $Ti^{3+}$ defects, and the charge transfer transition from these $Ti^{3+}$ trap states to the conduction band gives rise to this small absorption feature at ~1.75 eV. The electronic absorption spectra taken periodically during the whole photodoping process on both the $TiO_2$ and Fe:$TiO_2$ NCs show the immediate appearance of the broad plasmonic absorption followed by the weak feature at ~1.75 eV (see SI Figures 4.10 and 4.11). This observation suggests that the majority of photoexcited electrons are delocalized in the conduction band while that a fraction of them creates quasi-localized $Ti^{3+}$ defects with increased photodoping time.

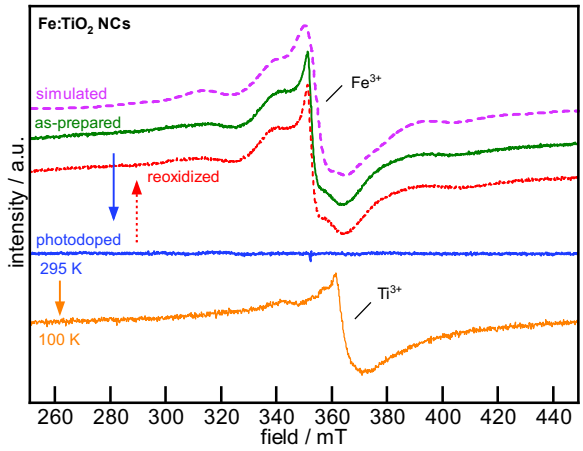


**Figure 4.2** The EPR spectrum of as-prepared NCs (green) compared to the simulated (pink/dotted), the photodoped NCs at room temperature (blue) and the 100 K (orange), and the EPR spectrum of reoxidized NCs represented with the red dotted line.

We further employed EPR spectroscopy to explore the effect of added electrons on $Fe^{3+}$ dopants. The room temperature EPR spectra of as-prepared and photodoped $Fe:TiO_2$ NCs are shown in Figure 4.2. As discussed in the earlier section, the as-prepared sample exhibits only a broad signal associated with the substitutional $Fe^{3+}$ dopants. With a short photodoping time (~20 min), the $Fe^{3+}$-related EPR signal is completely disappeared. This observation persists down to 100 K where a new axial signal at ~365 mT is detected. This broad and poorly resolved anisotropic signal is associated with the formation of $Ti^{3+}$ ($d^1$) defects consistent with absorption measurements and the literature.[24,26] The $Ti^{3+}$ signal is observed only at cryogenic temperature owing to its short spin relaxation times. The increased spin-spin relaxation pathways in the photodoped NCs with excess electrons cause the broadening of this $Ti^{3+}$ signal. The disappearance of the $Fe^{3+}$ signal with the simultaneous appearance of $Ti^{3+}$ defects is consistent with our recent report on Fe dopants in $SrTiO_3$ and $BaTiO_3$ NCs.[13] The $Fe^{3+}$ dopants in $TiO_2$ have been reported to create electron trap states below the conduction band.[28-30] We propose that photochemically added electrons reduce these trap states to EPR-silent $Fe^{2+}$ as

illustrated in Figure 4.3. The photoexcitation of charge carriers followed by the rapid hole quenching with EtOH raises the Fermi level into the conduction band. The substitutional $Fe^{3+}$ dopants act as trap states below the conduction band and get reduced to $Fe^{2+}$ during photodoping. Upon reopening the sample to air, these changes are reversed and the $Fe^{3+}$ signal is quantitatively recovered.

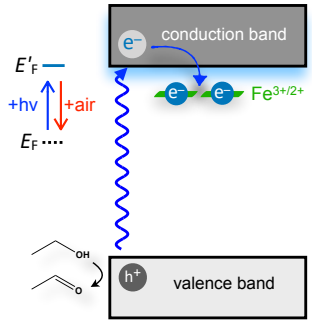


**Figure 4.3** Reversible electron trapping at the $Fe^{3+/2+}$ in Fe:$TiO_2$ colloidal NCs with photodoping.

Although the photodoping method offers a tunable and reversible control of the valance state of $Fe^{3+}$ dopants, the whole process is very sensitive to the presence of air. The traces of oxygen can make the photodoping process completely ineffective. The photochemically added electrons are typically stabilized by the adsorption of protons at the surface of NCs.[26,31] Upon exposing the sample to air, these electrons can easily react with molecular oxygen near the surfaces to produce superoxide radicals which we also observed in our previous report on Cr-doped $SrTiO_3$ NCs.[32] This instability of the added electrons limits the exploration of the photodoped NCs, and thus requires alternative methods. The incorporation of stable carriers in $TiO_2$ has been studied using anaerobic annealing methods and the aliovalent doping such as $Nb^{5+}$ and $Mo^{5+}$ etc., at substitutional $Ti^{4+}$ sites.[33,34] Although both approaches produce free electrons, we find post-synthetic annealing a least suitable method as it requires extreme temperatures and may affect the morphology and crystalline phase

of the NCs. Preparation of n-type $TiO_2$ NCs on the other hand using aliovalent doping can be achieved by simply adding appropriate metal salt during the synthesis without requiring any additional steps.

The synthesis of nominally 0.2% Fe 8% Nb (high enough to produce excess electrons) co-doped $TiO_2$ (to referred as (Fe,Nb):$TiO_2$ hereafter) NCs was carried out following the solvothermal procedure described in experimental section. The as-prepared NCs exhibit the crystal structure of anatase evident from the PXRD pattern (see SI Figure 4.5). Although no detectable secondary phases are observed, there is a significant elongation along the z-axis as summarized in Table 4.1. Such elongation has been previously observed in Nb-doped $TiO_2$ NCs and is related to changes in the morphology of NCs from cubic to "peanut" shape.[25] However, the TEM images in our work (see SI Figure 4.12) do not show any significant changes in the morphology of (Fe,Nb):$TiO_2$ NCs compared to undoped $TiO_2$ or Fe:$TiO_2$ NCs. Alternatively, we propose that a fraction of the added electrons with $Nb^{5+}$ doping can create localized $Ti^{3+}$ defects like what we observed in photodoped $TiO_2$ NCs. The $Ti^{3+}$ with electrons primarily occupying the ground state $d_{xz}$ and $d_{yz}$ orbitals can contribute to the elongation along the z-axis in the crystal structure.

The electronic absorption spectrum of colloidal solution of as-prepared (Fe,Nb):$TiO_2$ NCs exhibits a broad absorption feature tailing from the band-edge into the mid-IR region (Figure 4.4A) similar to photodoped NCs. We assign this characteristic broad absorption to the LSPR consistent with the other reports on Nb-doped $TiO_2$ NCs.[25,34] There is also clear evidence of a blue shift in the band-edge energy due to the Moss-Burstein effect which further confirms the incorporation of

$e^-_{CB}$ with Nb-doping (Figure 4.4A inset). In contrast to the photodoping method, we do not observe any additional absorption feature related to the $Ti^{3+}$ defects at ~1.75 eV. Despite the absence of this feature, we cannot rule out the exitance of $Ti^{3+}$ defects because the plasmonic absorption typically have a large oscillator strength that can occlude the absorption feature from trapped electrons. Nevertheless, these results provide convincing evidence that the substitution of $Nb^{5+}$ adds air-stable electrons and majority of which are free carriers in the conduction band of $TiO_2$ NCs.

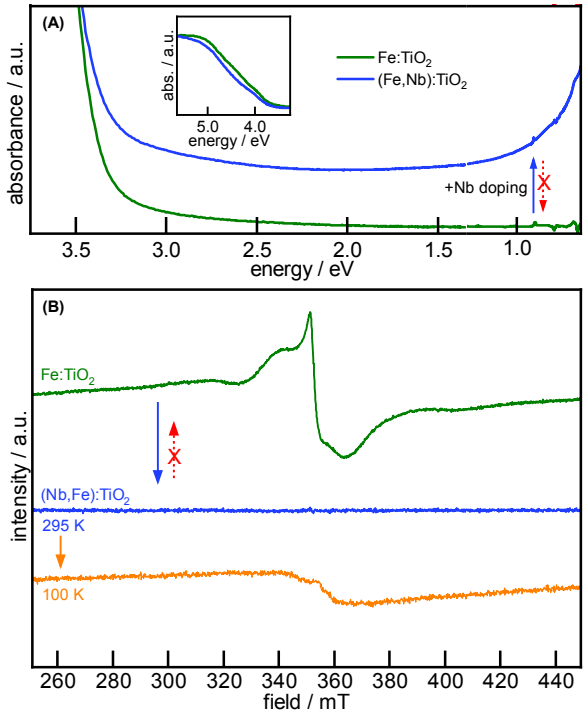


**Figure 4.4** The EPR spectra of as-prepared Fe:$TiO_2$ (green/top) and 0.2% Fe 8% Nb co-doped $TiO_2$ NCs collected at room temperature (blue/middle) and 100 K (orange/bottom).

To exploit the effect of the added electrons on $Fe^{3+}$ dopants, EPR measurements were carried out. The room temperature EPR spectrum of (Fe,Nb):$TiO_2$ compared to Fe:$TiO_2$ NCs shows the complete disappearance of $Fe^{3+}$ related EPR signal (see Figure 4.4B). This observation persists down to 100 K where a weak broad absorption feature corresponding to $Ti^{3+}$ defects is observed. We attribute the broadening of the

$Ti^{3+}$ signal to the increased spin-spin interactions in these heavily $Nb^{5+}$ doped $TiO_2$ NCs. The controlled experiments on nominally 2% and 5% Nb-doped $TiO_2$ NC further support the broadening of $Ti^{3+}$ signal with increased dopant concentration as shown in Figure 4.13. The disappearance of $Fe^{3+}$ signal both at room temperature and 100 K consistent with the absorption measurement in Figure 4.4A suggests that excess carriers introduced through aliovalent $Nb^{5+}$ doping reduces the $Fe^{3+}$ dopant to $Fe^{2+}$. This reduction process is completely *irreversible and stable* under ambient conditions compared to photodoping method. This observation opens the avenue for further exploration of mixed-valence states of $Fe^{3+}$ and other redox-active dopants in oxide lattices.

## 4.5 Supporting Information

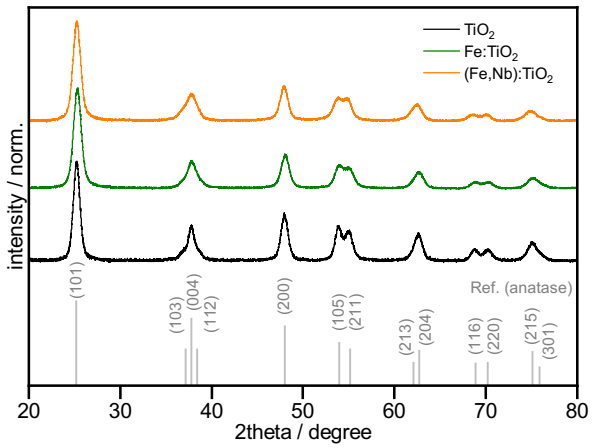


**Figure 4.5** Powder x-ray diffraction patterns of $TiO_2$ (black/bottom), Fe:$TiO_2$ (green/middle) and (Fe,Nb):$TiO_2$ (orange/top) NCs indexed to anatase.

**Table 4.1** The average lattice parameter and crystallite size calculated using Rigaku SmartLab Studio II on diffraction data shown in Figure 4.5.

| Sample NCs | Lattice parameters (Å) | | | Crystallite size (nm)† |
|---|---|---|---|---|
| | a | b | c | |
| $TiO_2$ | 3.7865 | 3.7865 | 9.5067 | 10.03 ± 0.024 |
| Fe:$TiO_2$ | 3.7902 | 3.7902 | 9.5158 | 8.63 ± 0.113 |
| (Fe,Nb):$TiO_2$ | 3.8009 | 3.8009 | 9.5430 | 8.93 ± 0.431 |

†Crystallite size is the average size calculated from (101) and (200) reflections.

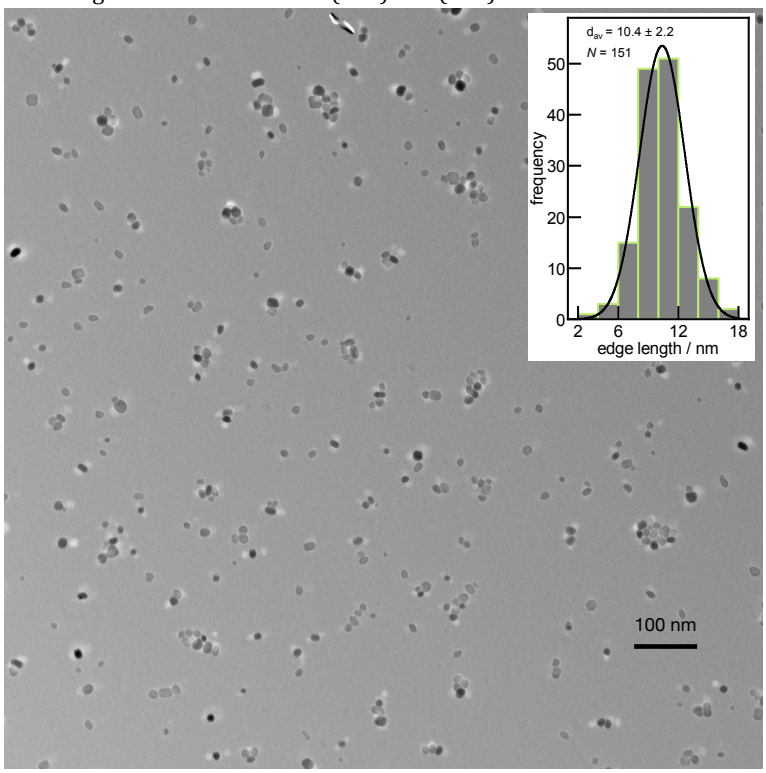


**Figure 4.6** Transmission electron microscopy (TEM) image of as-prepared $TiO_2$ NCs and the size distribution plot from analyzing crystals using ImageJ software.

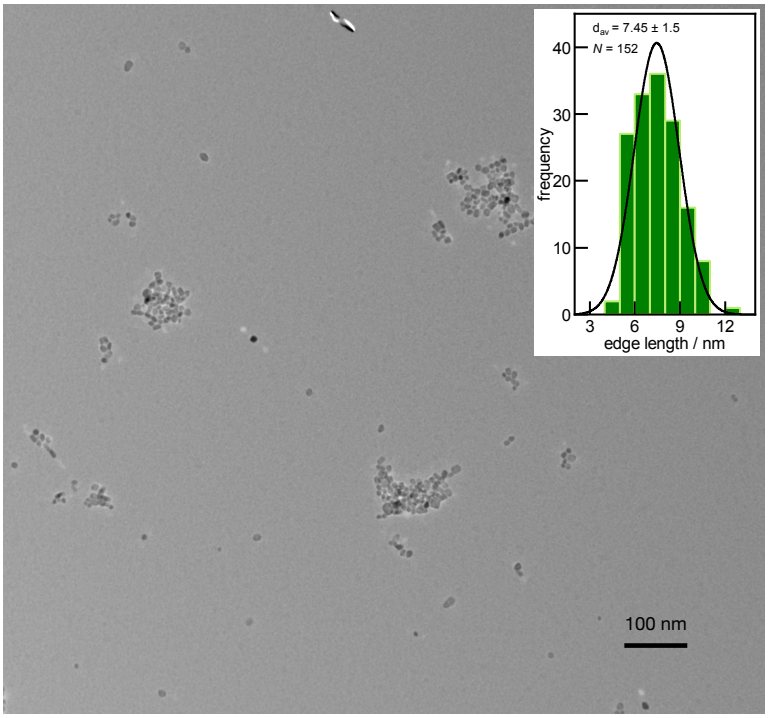


**Figure 4.7** The TEM image and the size distribution plot of as-prepared Fe:$TiO_2$ NCs.

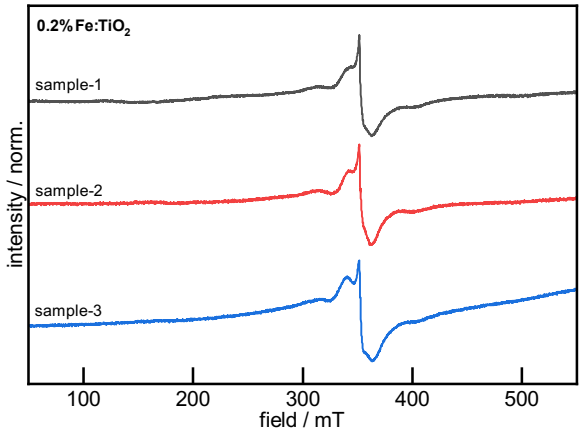


**Figure 4.8** EPR spectrum of as-prepared Fe:$TiO_2$ NCs collected with a wide field range. All the samples were prepared under identical condictiones to validate the reproducibility of EPR spectrum. No baseline correction was performed on the date.

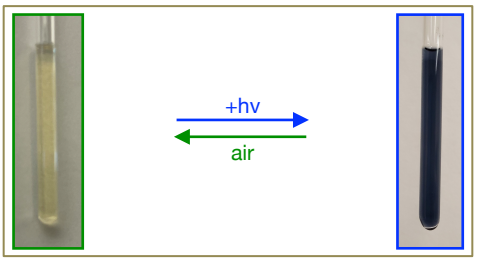


**Figure 4.9** Photographs of air-free solution of Fe:$TiO_2$ NCs before (green/left) and after photodoping (blue/right) showing a clear change in color.

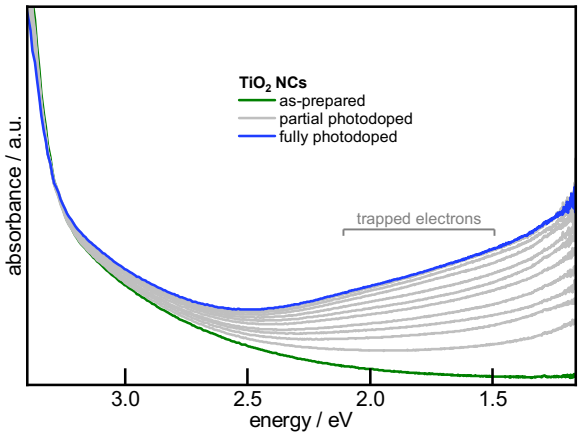


**Figure 4.10** UV-Vis spectra of as-prepared (green), partially photodoped (grey line collected at various stages) and fully photodoped (blue) $TiO_2$ NCs.

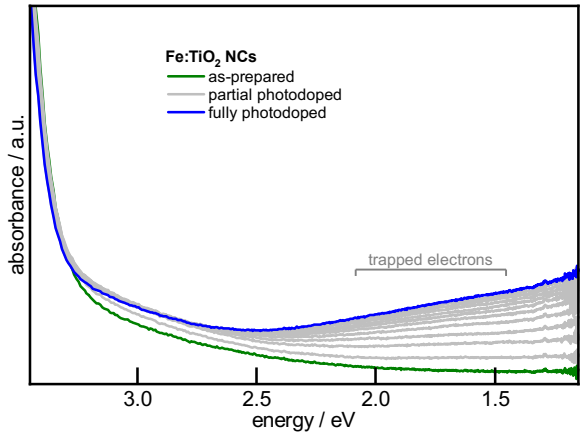


**Figure 4.11** UV-Vis spectra of as-prepared (green), partially photodoped (grey line collected at various stages) and fully photodoped (blue) Fe:$TiO_2$ NCs.

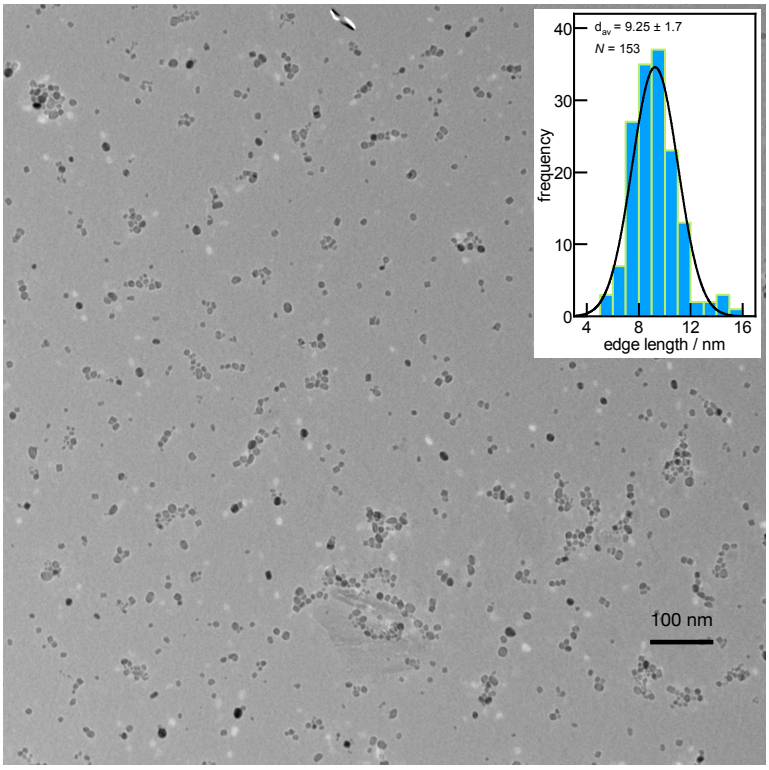


**Figure 4.12** The TEM image and the size distribution plot of as-prepared (Nb,Fe):$TiO_2$ NCs.

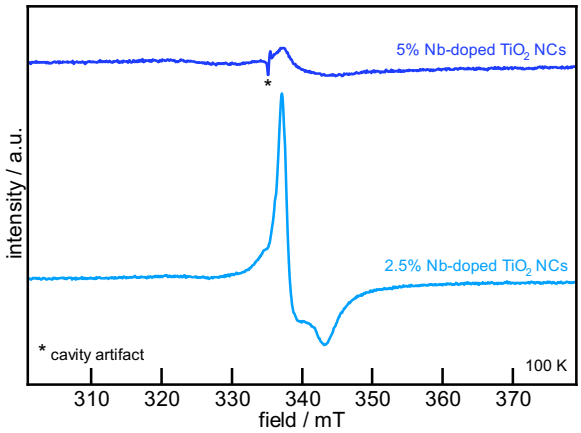


**Figure 4.13** EPR spectra of nominally 2.5% Nb (light blue/bottom) and 5% Nb-doped $TiO_2$ NCs (dark blue/top) collected at 100 K.

## 4.6 References

(1) Queisser, H. J.; Haller, E. E. Defects in semiconductors: some fatal, some vital. *Science* **1998,** *281* (5379), 945-950.

(2) Schwartz, D. A.; Kittilstved, K. R.; Gamelin, D. R. Above-room-temperature ferromagnetic $Ni^{2+}$-doped ZnO thin films prepared from colloidal diluted magnetic semiconductor quantum dots. *Appl. Phys. Lett.* **2004,** *85* (8), 1395-1397.

(3) Norberg, N. S.; Kittilstved, K. R.; Amonette, J. E.; Kukkadapu, R. K.; Schwartz, D. A.; Gamelin, D. R. Synthesis of colloidal $Mn^{2+}$: ZnO quantum dots and high-$T_C$ ferromagnetic nanocrystalline thin films. *J. Am. Chem. Soc.* **2004,** *126* (30), 9387-9398.

(4) Zhu, H.; Tao, J.; Dong, X. Preparation and photoelectrochemical activity of Cr-doped $TiO_2$ nanorods with nanocavities. *J. Phys. Chem. C* **2010,** *114* (7), 2873-2879.

(5) Benouis, C.; Benhaliliba, M.; Mouffak, Z.; Avila-Garcia, A.; Tiburcio-Silver, A.; Lopez, M. O.; Trujillo, R. R.; Ocak, Y. The low resistive and transparent Al-doped $SnO_2$ films: p-type conductivity, nanostructures and photoluminescence. *J. Alloys Compd.* **2014,** *603*, 213-223.

(6) Zhou, D. M.; Wang, P. J.; Roy, C. R.; Barnes, M. D.; Kittilstved, K. R. Direct evidence of surface charges in n-type Al-doped ZnO. *J. Phys. Chem. C* **2018,** *122* (32), 18596-18602.

(7) Cao, Y. C. Impurities enhance semiconductor nanocrystal performance. *Science* **2011,** *332* (6025), 48-49.

(8) Mansoor, H.; Harrigan, W. L.; Lehuta, K. A.; Kittilstved, K. R. Reversible control of the Mn oxidation state in $SrTiO_3$ bulk powders. *Front. Chem.* **2019,** *7*, 353.

(9) Lehuta, K. A.; Kittilstved, K. R. Reversible control of the chromium valence in chemically reduced Cr-doped $SrTiO_3$ bulk powders. *Dalton Trans.* **2016,** *45* (24), 10034-10041.

(10) Glais, E.; Massuyeau, F.; Gautier, R. Tuning the oxidation states of dopants: a strategy for the modulation of material photoluminescence properties. *Chem. Eur. J.* **2020**.

(11) Garnet, N. S.; Ghodsi, V.; Hutfluss, L. N.; Yin, P.; Hegde, M.; Radovanovic, P. V. Probing the role of dopant oxidation state in the magnetism of diluted magnetic oxides using Fe-doped $In_2O_3$ and $SnO_2$ nanocrystals. *J. Phys. Chem. C* **2017,** *121* (3), 1918-1927.

(12) Farvid, S. S.; Sabergharesou, T.; Hutfluss, L. N.; Hegde, M.; Prouzet, E.; Radovanovic, P. V. Evidence of charge-transfer ferromagnetism in transparent diluted magnetic oxide nanocrystals: switching the mechanism of magnetic interactions. *J. Am. Chem. Soc.* **2014,** *136* (21), 7669-7679.

(13) Abdullah, M.; Kittilstved, K. R.; Nelson, R. J. Tunable redox activity at $Fe^{3+}$ centers in colloidal $ATiO_3$ (A = Sr and Ba) nanocrystals. *Chem. Mater.* **2021**.

(14) Dinh, C.-T.; Nguyen, T.-D.; Kleitz, F.; Do, T.-O. Shape-controlled synthesis of highly crystalline titania nanocrystals. *ACS Nano* **2009,** *3* (11), 3737-3743.

(15) Liu, M.; Piao, L.; Zhao, L.; Ju, S.; Yan, Z.; He, T.; Zhou, C.; Wang, W. Anatase $TiO_2$ single crystals with exposed {001} and {110} facets: facile synthesis and enhanced photocatalysis. *Chem. Commun.* **2010,** *46* (10), 1664-1666.

(16) Shannon, R. D. Revised effective ionic radii and systematic studies of interatomic distances in halides and chalcogenides. *Acta Crystallogr. Sect. A: Found. Crystallogr.* **1976,** *32* (5), 751-767.

(17) Sekiya, T.; Ichimura, K.; Igarashi, M.; Kurita, S. Absorption spectra of anatase $TiO_2$ single crystals heat-treated under oxygen atmosphere. *J. Phys. Chem. Solids* **2000,** *61* (8), 1237-1242.

(18) Moradi, H.; Eshaghi, A.; Hosseini, S. R.; Ghani, K. Fabrication of Fe-doped $TiO_2$ nanoparticles and investigation of photocatalytic decolorization of reactive red 198 under visible light irradiation. *Ultrason. Sonochem.* **2016,** *32*, 314-319.

(19) Pecchi, G.; Reyes, P.; Lopez, T.; Gomez, R.; Moreno, A.; Fierro, J.; Martínez-Arias, A. Catalytic combustion of methane on Fe-$TiO_2$ catalysts prepared by sol-gel method. *J. Sol-Gel Sci. Technol.* **2003,** *27* (2), 205-214.

(20) Yermakov, A. Y.; Gubkin, A. F.; Korolev, A. V.; Molochnikov, L. S.; Uimin, M. A.; Rosenfeld, E. V.; Kurkin, M. I.; Minin, A. S.; Volegov, A. S.; Boukhvalov, D. W. Formation of Fe–Fe antiferromagnetic dimers in doped $TiO_2$:Fe nanoparticles. *J. Phys. Chem. C* **2018,** *123* (2), 1494-1505.

(21) Yu, S.; Yun, H. J.; Lee, D. M.; Yi, J. Preparation and characterization of Fe-doped $TiO_2$ nanoparticles as a support for a high performance CO oxidation catalyst. *J. Mater. Chem.* **2012,** *22* (25), 12629-12635.

(22) Cheng, G.; Liu, X.; Song, X.; Chen, X.; Dai, W.; Yuan, R.; Fu, X. Visible-light-driven deep oxidation of NO over Fe doped $TiO_2$ catalyst: Synergic effect of Fe and oxygen vacancies. *Appl. Catal., B* **2020,** *277*, 119196.

(23) Açıkgöz, M.; Gnutek, P.; Rudowicz, C. Modeling zero-field splitting parameters for dopant $Mn^{2+}$ and $Fe^{3+}$ ions in anatase $TiO_2$ crystal using superposition model analysis. *Chem. Phys. Lett.* **2012,** *524*, 49-55.

(24) Joost, U.; Šutka, A.; Oja, M.; Smits, K.; Döbelin, N.; Loot, A.; Järvekülg, M.; Hirsimäki, M.; Valden, M.; Nõmmiste, E. Reversible photodoping of $TiO_2$ nanoparticles for photochromic applications. *Chem. Mater.* **2018,** *30* (24), 8968-8974.

(25) De Trizio, L.; Buonsanti, R.; Schimpf, A. M.; Llordes, A.; Gamelin, D. R.; Simonutti, R.; Milliron, D. J. Nb-doped colloidal $TiO_2$ nanocrystals with tunable infrared absorption. *Chem. Mater.* **2013,** *25* (16), 3383-3390.

(26) Schrauben, J. N.; Hayoun, R.; Valdez, C. N.; Braten, M.; Fridley, L.; Mayer, J. M. Titanium and zinc oxide nanoparticles are proton-coupled electron transfer agents. *Science* **2012,** *336* (6086), 1298-1301.

(27) Di Valentin, C.; Pacchioni, G.; Selloni, A. Reduced and n-type doped $TiO_2$: nature of $Ti^{3+}$ species. *J. Phys. Chem. C* **2009,** *113* (48), 20543-20552.

(28) Sood, S.; Umar, A.; Mehta, S. K.; Kansal, S. K. Highly effective Fe-doped $TiO_2$ nanoparticles photocatalysts for visible-light driven photocatalytic degradation of toxic organic compounds. *J. Colloid Interface Sci.* **2015,** *450*, 213-223.

(29) Carneiro, J.; Azevedo, S.; Fernandes, F.; Freitas, E.; Pereira, M.; Tavares, C.; Lanceros-Méndez, S.; Teixeira, V. Synthesis of iron-doped $TiO_2$ nanoparticles by ball-milling process: the influence of process parameters on the structural, optical, magnetic, and photocatalytic properties. *J. Mater. Sci.* **2014,** *49* (21), 7476-7488.

(30) Ali, T.; Tripathi, P.; Azam, A.; Raza, W.; Ahmed, A. S.; Ahmed, A.; Muneer, M. Photocatalytic performance of Fe-doped $TiO_2$ nanoparticles under visible-light irradiation. *Mater. Res. Express* **2017,** *4* (1), 015022.

(31) Schimpf, A. M.; Gunthardt, C. E.; Rinehart, J. D.; Mayer, J. M.; Gamelin, D. R. Controlling carrier densities in photochemically reduced colloidal ZnO nanocrystals: size dependence and role of the hole quencher. *J. Am. Chem. Soc.* **2013,** *135* (44), 16569-16577.

(32) Harrigan, W. L.; Kittilstved, K. R. Reversible modulation of the $Cr^{3+}$ spin dynamics in colloidal $SrTiO_3$ nanocrystals. *J. Phys. Chem. C* **2018,** *122* (46), 26652-26657.

(33) Naldoni, A.; Altomare, M.; Zoppellaro, G.; Liu, N.; Kment, S. t. p. n.; Zbořil, R.; Schmuki, P. Photocatalysis with reduced $TiO_2$: from black $TiO_2$ to cocatalyst-free hydrogen production. *ACS Catalysis* **2018,** *9* (1), 345-364.

(34) Cao, S.; Zhang, S.; Zhang, T.; Fisher, A.; Lee, J. Y. Metal-doped $TiO_2$ colloidal nanocrystals with broadly tunable plasmon resonance absorption. *J. Mater. Chem. C* **2018,** *6* (15), 4007-4014.

# CHAPTER 5

# EFFECT OF N-TYPE CARRIERS ON SUBSTITUTIONAL CHROMIUM DOPANTS IN TI(IV)-BASED OXIDE NANOCRYSTALS

## 5.1 Introduction

The introduction of paramagnetic defects into semiconducting materials has recently attracted a great deal of attention for developing the field of quantum computing – where a spin degree of freedom is exploited in addition to electronic charge to create new functionalities.[1,2] The advancement of magnetic semiconductors has succeeded in creating intrinsic defects such as vacancies[3,4] and doping the paramagnetic impurity ions into semiconducting host-lattices.[5-7] The coexistence of magnetism and semiconducting properties leads to exchange interactions between localized magnetic moments and the charge carriers resulting in new magneto-optical properties.[8,9] Similarly, multiferroic materials that exhibit ferroelectricity and magnetism are also widely investigated for various spin-based applications.[10] Despite the substantial progress made over the past few decades, the quest for new materials with unique magnetic properties, particularly at room temperature, continues.

Barium titanate ($BaTiO_3$), a ternary oxide perovskite, has emerged as one of the prime candidates for spintronics owing to its multifunctional properties.[11] In addition to its intrinsic high dielectric constant and ferroelectricity, magnetism by substituting paramagnetic ions at B-site or n-type conductivity by partial reduction of $Ti^{4+}$ to $Ti^{3+}$ has also been well studied.[12,13] Though significant progress has been made to achieve various properties, the interaction between paramagnetic dopants

and n-type charge carriers in a single host-lattice, particularly at nanoscale, remains elusive.

We recently reported that the introduction of n-type carriers could control the spin-relaxation time of $Cr^{3+}$ dopants in $SrTiO_3$.[14] The discovery of this tunability over spin properties has led to our current work to explore such spin interactions in other Ti-based lattices to probe the role of host crystal structure and the site symmetry. Herein we report the synthesis and characterization of colloidal $Cr^{3+}$-doped $BaTiO_3$ NCs using a hydrothermal method. The dopant-specific spectroscopic studies show that dopant exists in the $Cr^{3+}$ valence state occupying the octahedral $Ti^{4+}$ site. The post-synthetic introduction of n-type charge carriers using the photodoping method shows that these carriers are localized at $Ti^{3+}$ defects creating a small-polaron. Furthermore, the presence of two paramagnetic centers ($Cr^{3+}$ and $Ti^{3+}$) in the same lattice structure shows a spin cross-relaxation phenomenon where fast-relaxing $Ti^{3+}$ accelerates the $Cr^{3+}$ spin-relaxation time. We further validate the existence of such spin processes in colloidal Cr-doped $TiO_2$ NCs. The added electrons in $TiO_2$ are delocalized in the conduction band yet show spin cross-relaxation with substitutional $Cr^{3+}$ dopants.

## 5.2 Experimental

### 5.2.1 Materials

Barium hydroxide octahydrate ($Ba(OH)_2{\cdot}8H_2O$, 99%, Alfa Aesar), titanium(IV) bis(ammonium lactate)dihyroxide (TALH, 50% in water, Alfa Aesar), sodium hydroxide (NaOH, ACS Certified, Fisher Chemical), Titanium(iv) *n*-butoxide ($Ti(OBu)_4$, 99%, Acros Organics), oleylamine (>50%, TCI America), oleic acid (90%,

Fisher Chemicals), chromium nitrate nonahydrate ($Cr(NO_3)_3 \cdot 9H_2O$, 99.99% Sigma Aldrich), ethanol (200 proof, PHARMCO-AAPER), 21 elements standard (5% $HNO_3$, PerkinElmer), hydrazine hydrate (100% Acros Organics), nitric acid ($HNO_3$, Certified ACS Plus – Safe Cote, Fisher Chemicals), hydrochloric acid (HCl, Certified ACS Plus, Fisher Chemical), toluene (optima, Fisher Chemicals) and hexanes (optima, Fisher Chemicals) were used as received.

### 5.2.2 Synthesis of Nanocrystals

**Pure and Cr-doped $BaTiO_3$ nanocrystals.** The Synthesis of colloidal $BaTiO_3$ NCs was also carried out by a hydrothermal method reported in our recent study. In a typical preparation, 1.5 mmol of each TALH and $Ba(OH)_2$ were dissolved in 24 mL distilled water, followed by 6 mL of NaOH (5 M). The reaction solution was then transferred to a 45-mL Teflon-lined autoclave, and then hydrazine hydrate (5 mmol), oleylamine (6 mmol), and oleic acid (6 mmol) were added. The pH of the reaction solution was 12. The sealed autoclave was placed in custom-made aluminum block housing that was heated to 215 °C and constantly stirred for 24 h using a stirring hotplate. After the synthesis, the autoclave was cooled to room temperature. The solid product was collected, washed with EtOH, and dissolved in nonpolar solvents such as hexanes to produce a transparent solution. To synthesize nominally 0.1% Cr-doped $BaTiO_3$ colloidal NCs, 1.5 mL of 0.001 M aqueous solution of $Cr(NO_3)_3$ was added before adding the NaOH solution.

**Pure and Cr-doped $TiO_2$ NCs.** Synthesis of colloidal $TiO_2$ NCs was carried out by a modified solvothermal method. In a typical preparation, 1.5 mmol of $Ti(OBu)_4$ were mixed with 7.5 mmol of oleic acid and 7.5 mmol of oleylamine in 1.1 mL of ethanol.

The obtained mixture was then transferred to a 50 mL Teflon-lined autoclave containing 6 mL of 98% ethanol in water (v/v) and heated to 200 °C for 18 hours. After the synthesis, the autoclave was cooled down to room temperature, and the solid product was collected, washed with ethanol several times, and suspended in nonpolar solvents such as toluene to produce colloidal solutions. For the synthesis of 0.1% Cr-doped $TiO_2$, 1.5 mL of 0.001 M aqueous solution of $Cr(NO_3)_3$ was added before closing the autoclave.

### 5.2.3 Physical Characterization

All measurements were collected at room temperature and either on undoped or 0.1% Cr-doped $BaTiO_3$ and undoped or 0.1% Cr-doped $TiO_2$ NCs unless specified otherwise. Electronic absorption and emission spectra were obtained on colloidal suspensions in an air-tight quartz cuvette with 1-cm pathlength on Cary 50 Bio and Cary Eclipse, respectively. Near-IR absorption measurements were collected on colloidal solutions in a custom-made 1-mm pathlength quartz cuvette on Varian 670 Fourier transform infrared (FTIR) spectrometer equipped with InGaAs detector and a near-IR quartz beam splitter. The functional groups and surface chemistry analysis of solvent-free NCs were carried out on Bruker Alpha-P spectrophotometer equipped with a diamond attenuated total reflectance (ATR) crystal. Electron paramagnetic resonance (EPR) spectra were measured at X-band frequency (9.6 GHz) with a Bruker Elexsys-500 equipped with a Super High QE (ER4123SHQE) cavity. Transmission electron microscopy (TEM) images of freshly prepared NCs drop-casted onto carbon-coated (3nm) copper grids (CF400-CU-50, Electron Microscopy Sciences) were collected on JEOL 2000FX electron microscopy. The average size distribution and

standard deviation were generated by analyzing particles using ImageJ software. Powder X-ray diffraction patterns were collected on Rigaku Smart Lab SE in the Bragg-Brentano configuration with a Cu K-source. An inductively coupled plasma optical emission spectrometer (ICP-OES, Optima 4300 DV - PerkinElmer) was employed to analyze the stoichiometry of metal ions in NCs.

### 5.2.4 Photochemical Reduction

Photochemical reduction, also known as photodoping, was performed to introduce extra electrons in as-prepared colloidal NCs. Sample preparation was completed in the Argon-filled glove box where NCs suspended in hexanes with ~5% EtOH as sacrificial reductant were transferred to a 1 mm air-tight cuvette before removal. Samples were photodoped by prolonged exposure to irradiation from 75 W xenon lamp. The electronic absorption measurements were taken periodically during the entire photodoping process. When absorption did not change over an exposure of a few hours, samples were considered to have reached their maximum photodoping level. For EPR measurements, NCs were transferred to a 4 mm air-tight customized quartz tube, and photodoping inside the EPR resonator was carried out by UV irradiation using fiber optics. To maintain a similar irradiation intensity, the lamp was warmed up for about 30 minutes before each photodoping experiment.

## 5.3 Results and Discussion

The synthesis of $BaTiO_3$ and 0.1% Cr-doped $BaTiO_3$ NCs (referred to as Cr:$BaTiO_3$ hereafter) was carried out by a facile hydrothermal method developed previously by our group.[15,16] Various optimization parameters such as pH, temperature, and time are summarized in supporting information (see SI Figure 5.6-

5.10 and Table 5.1-5.4). The crystallinity and phase purity of as-prepared NCs were confirmed by powder X-ray diffraction measurements. The diffraction patterns of both samples are indexed to the cubic phase of $BaTiO_3$ with space group Pm$\underline{3}$m and no considerable secondary phases were observed (see SI Figure 5.11).[17,18] The TEM images shown in the supporting information (see SI Figure 5.12) and its analysis confirmed that NCs exhibit cuboidal morphology with an average diameter of 12.8 ± 1.8 nm. FTIR measurements showed that the surface of NCs is passivated with oleic acid and oleylamine to provide colloidal stability (see SI Figure 5.13).

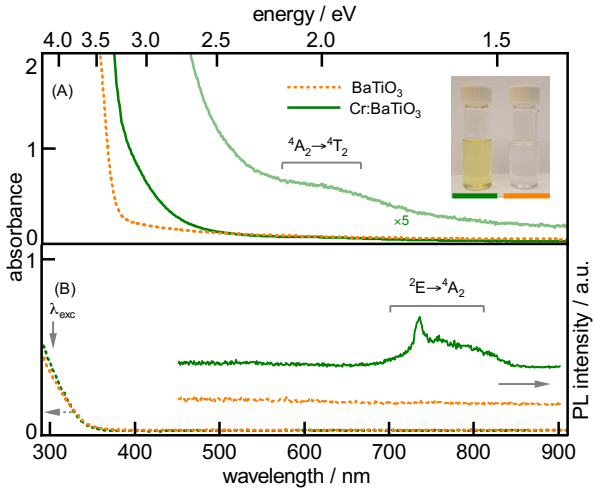


**Figure 5.1** (A) Electronic absorption spectra of a concentrated solution of as-prepared $BaTiO_3$ and Cr:$BaTiO_3$ NCs in hexanes. The color photographs of both samples are shown in the inset. (B) Photoluminescence spectra of dilute samples excited at 300 nm. The absorption spectra of both samples with absorbance less than 0.5 at the excitation wavelength, as shown on the left-axis.

Figure 5.1A shows the room temperature UV-Vis spectra and color photographs of concentrated suspensions of $BaTiO_3$ and Cr:$BaTiO_3$ NCs in hexanes. The electronic absorption spectra of both samples are dominated by the band-edge transition *ca*. 3.25 eV in good agreement with single-crystal $BaTiO_3$.[14] However, Cr:$BaTiO_3$ NCs also exhibit an absorption tail into the visible region and appear crispy yellow as depicted from color photographs shown in Figure 5.1A inset. This absorption smearing out of the band-edge is attributed to a combination of charge

transfer transition involving $Cr^{3+}$ sub-bandgap impurity levels and ligand-field $^4A_2 \rightarrow {}^4T_1$ transition of $Cr^{3+}$ in cubic symmetry.[15] The low energy $^4A_2 \rightarrow {}^4T_2$ transition of $Cr^{3+}$ is also weakly observed, as shown in enlarged magnification *ca*. 2.0 eV. Figure 5.1B shows the room temperature emission spectra of dilute solutions of both NCs excited at 300 nm. The characteristic emission at ~1.68 eV originates from spin-forbidden $^2E \rightarrow {}^4A_2$ transition of octahedral $Cr^{3+}$ in Cr:$BaTiO_3$ NCs.[16,17]

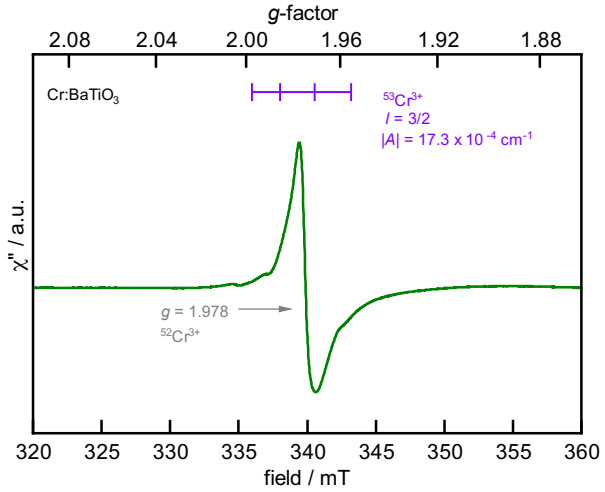


**Figure 5.2** Room temperature EPR spectrum of as-prepared Cr:$BaTiO_3$ NCs. A weak hyperfine from $^{53}Cr^{3+}$ nuclear spin ($I$ = ¾) is represented with a four-line bar around broad resonance.

To probe the $Cr^{3+}$ speciation, we employed EPR spectroscopy at X-band frequency (9.5 GHz). $Cr^{3+}$ dopants in the $BaTiO_3$ lattices preferentially substitute $Ti^{3+}$ ions because of the similar ionic radii in octahedral cubic symmetry [($Cr^{3+}$) = 0.62 Å, ($Ti^{4+}$) = 0.61 Å].[18] Figure 5.2 shows the room temperature EPR spectrum of as-prepared Cr:$BaTiO_3$ NCs. The broad isotropic resonance at $g$ = 1.978 corresponds to spin-allowed ($\Delta m_s = \pm 1$) transition of $^{52}Cr^{3+}$ ($S$ = 3/2) in octahedral symmetry consistent with Cr-doped $SrTiO_3$ NCs.[19,20] A weak 4-line hyperfine (|A| = 17.3 x $10^{-1}$ $cm^{-1}$) originating from $^{53}Cr^{3+}$ ($I$ = 3/2) nuclei with natural abundance of 9.5% is displayed with a top bar above broad resonance.

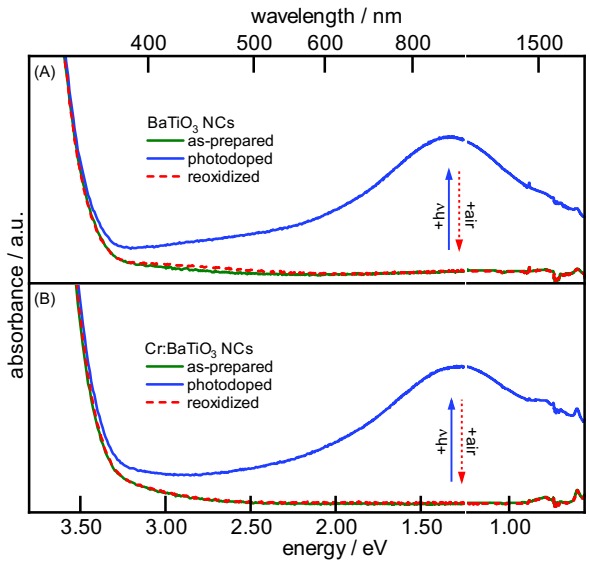


**Figure 5.3** Electronic absorption spectra of (A) $BaTiO_3$ and (B) $Cr:BaTiO_3$ NCs solution in hexanes as a function of photodoping time. The green spectrum belongs to as-prepared NCs, and the blue spectrum corresponds to maximally photodoped NCs. The red dotted line overlapping the as-prepared NCs belongs to the reoxidized sample.

To introduce n-type charge carriers, photodoping experiments were performed (see the experimental section for detailed procedure). Briefly, UV irradiation of anaerobic solution of as-prepared NCs creates electron/hole pairs (excitons), and the rapid quenching of holes with ethanol leaves extra electrons in the NCs. Figure 5.3 shows the UV-visible spectra of NCs as a function of photodoping time. The electronic absorption spectrum of as-prepared NCs is dominated by the band-edge transition above 3.25 eV. With increased photodoping time, the physical appearance of the samples gradually changes to blue with a broad absorption feature that extends throughout the entire visible region into near-IR. The continuous growth of this new absorption feature without changing the band-edge energy suggests that added electrons are not free or delocalized in the conduction band ($e^-_{CB}$), which would have otherwise displayed a significant blue-shift in band-edge absorption due to the Moss-Burstein effect.[20,21] Instead, added electrons create localized $Ti^{3+}$ trap states. In our recent study on the photodoped $SrTiO_3$ NCs,[14] similar blue colorations and an

absorption tail through the visible region was observed. We attributed this broad absorption centered at *ca*. 1.2 eV to charge transfer transition of trapped electrons at polaronic $Ti^{3+}$ sites to the conduction band of $BaTiO_3$ NCs. There is no significant difference in absorption features between $BaTiO_3$ and Cr:$BaTiO_3$ NCs.

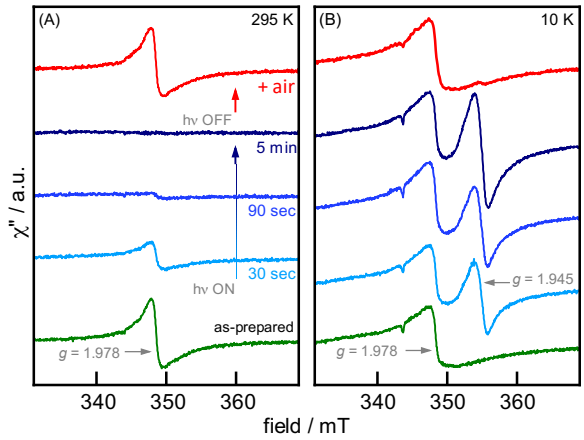


**Figure 5.4** EPR spectra of Cr:$BaTiO_3$ colloidal solutions in hexanes with increased photodoping time at room temperature (left panel-A) and at cryogenic temperature 10 K (right panel-B) with increased photodoping time. The red spectra in both panels correspond to reoxidized samples with air.

To probe the interplay between these polaronic electrons and the substitutional $Cr^{3+}$ dopants, we employed EPR spectroscopy. Figure 5.4A shows the room temperature EPR spectra of Cr:$BaTiO_3$ NCs collected at various photodoping times. With very short photodoping time, the EPR signal at $g$ = 1.978 corresponding to $Cr^{3+}$ sequentially decreases in intensity and completely disappears in 5 min of photodoping time. This EPR signal is quantitatively recovered upon reopening the photodoped samples to air. However, the acquisition of EPR measurements at 10 K as displayed in Figure 5.4B shows that the $Cr^{3+}$ EPR signal remains *intact* with the photodoping, while a new g = 1.945 signal starts appearing. This new signal corresponds to the paramagnetic $Ti^{3+}$ ($d^1$, S = ½) defects that appear only at cryogenic temperature owing to its fast spin relaxation time. This observation suggests that $Cr^{3+}$ dopants are mimicking the spin dynamics of $Ti^{3+}$ in photodoped NCs - acceleration of

spin relaxation times through a near-resonant cross-relaxation phenomenon consistent with our previous report.[21]

To further confirm the existence of spin acceleration, we measured the power saturation rollover behavior of $Cr^{3+}$ dopants in the absence and presence of $Ti^{3+}$ defects. In this particular experiment, a series of EPR spectra on as-prepared and photodoped NCs were collected at various applied microwave powers traversing from lowest to the maximum capacity of the equipment as discussed in an earlier report and also in chapter 3 above.[22] Figure 5.5A-B plots the peak-to-peak signal intensity ($\Delta Y$) extracted from EPR spectra of $Cr^{3+}$ in both the as-prepared and the photodoped NCs and $Ti^{3+}$ in photodoped NCs against the microwave power ($h_1$) at 10 K. At low power end, $\Delta Y$ for $Cr^{3+}$ in as-prepared NCs (green date) increases approximately linearly with increasing $h_1$, but at high power, it rolls over and begins to saturate. While at the same power range, $Cr^{3+}$ and $Ti^{3+}$ signal intensities in photodoped NCs (blue data) increase continuously without showing any signs of saturation. This typical behavior of signal intensities in photodoped NCs reflects the acceleration of spin relaxation times as observed previously in $Cr^{3+}$-doped $SrTiO_3$ NCs. Due to the absence of rollover behavior (saturation) in photodoped NCs, fitting this data is challenging to extract the spin relaxation rates. However, pulse EPR measurements could be carried out to quantify the T1 and T2 times directly. Nevertheless, this data suggests that spin interactions between $Ti^{3+}$ and $Cr^{3+}$ exist regardless of the A-site cation in the $ABO_3$-type cubic crystal structure.

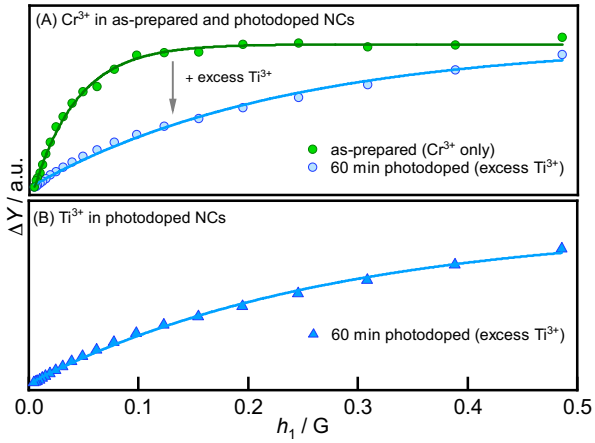


**Figure 5.5** Normalized peak-to-peak intensity ($\Delta Y$) of 10 K CW-EPR spectra of (A) $Cr^{3+}$ in as-prepared and photodoped NCs and (B) $Ti^{3+}$ in photodoped NCs against the microwave power ($h_1$).

To validate the existence of such interactions and the effect of site symmetry, we extended this study to 0.1% Cr-doped $TiO_2$ NCs (referred to as Cr:$TiO_2$ hereafter) prepared from a solvothermal method (see the experimental section for the procedure and SI Figure 5.14 for PXRD measurements). Room temperature EPR measurements on as-prepared samples show anisotropic signal at $g$-value = 1.978 with a prominent zero-field splitting consistent with simulated EPR spectrum using EasySpin (see SI Figure 5.15). This signal is assigned to the substitution of $Cr^{3+}$ at $Ti^{4+}$ site in anatase $TiO_2$ NCs. The electronic absorption spectra displayed in Figure 5.16A-B show the appearance of a broad absorption feature tailing through the band-edge with photodoping. This characteristic broad absorption that maximizes into the mid-IR has been previously observed in n-type $TiO_2$ nanoparticles and is attributed to the localized surface plasmon resonance (LSPR).[23,24] A clear blue-shift in the band-edge absorption with photodoping due to the Moss-Burstein effect indicates the free or delocalized electrons in the conduction band. It is important to notice that in addition to the LSPR-related broad absorption, a weak feature around ~1.75 eV (800 nm) also appears. The energy of this feature is consistent with the trapped electrons at $Ti^{3+}$

sites, as reported by Mayer and coworkers in photodoped $TiO_2$ nanoparticles.[25] Valentin *et al.* found that quasi-localized or localized $Ti^{3+}$ states in the n-type $TiO_2$ lattices are very close in energy (~0.1 eV) to the delocalized electrons, and oftentimes they are thermally excited into the conduction band.[26] We speculate that a fraction of electrons in photodoped NCs creates thermally-detrapped $Ti^{3+}$ defects, and the charge transfer transition from these $Ti^{3+}$ trap states to the conduction band gives rise to this small absorption feature at ~1.75 eV. This observation suggests that the majority of photoexcited electrons are delocalized in the conduction band while that a fraction of them creates quasi-localized $Ti^{3+}$ defects with increased photodoping time.

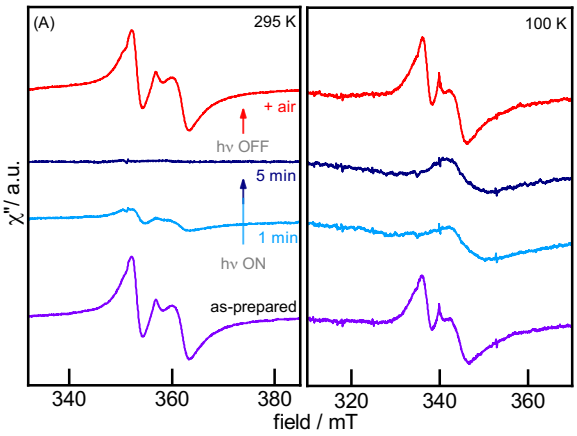


**Figure 5.6** EPR spectra of Cr:$TiO_2$ NCs as a function of photodoping time collected at (A) 295 K and (B) 100 K.

The room temperature EPR spectra of Cr:$TiO_2$ NCs as a function of photodoping time are shown in Figure 5.6A. With a short photodoping time, the $Cr^{3+}$-related EPR signal is completely disappeared and returns to its original states upon reopening the samples to air. This observation seems consistent with the previous discussion on Cr:$BaTiO_3$ NCs. However, the EPR measurements at 100 K (Figure 5.6B) show a broad and poorly resolved $Ti^{3+}$ signal. The $Ti^{3+}$ signal in general is observed only at

cryogenic temperature owing to its short spin relaxation times. The increased spin-spin relaxation pathways in the photodoped NCs with a lot of $Ti^{3+}$ in the vicinity of each other cause the broadening of this $Ti^{3+}$ signal. We further suspect the overlapping of $Cr^{3+}$ and $Ti^{3+}$ signals also led to this broadening. Nevertheless, this observation suggests spin interaction between excess electrons and substitutional $Cr^{3+}$ dopants in colloidal $TiO_2$. We suspect this phenomenon to exist in other Ti(IV)-based oxide NCs as well. High-frequency EPR measurements to resolve these overlapping signals and pulse EPR would be an alternative approach to further study the changes in spin properties of dopants in these oxide NCs.

## 5.4 Supporting Information

**Optimization of synthesis condition.** For the synthesis of high-quality colloidal NCs, several different synthesis parameters were tuned, and the resulting products were analyzed using powder X-ray diffraction, electronic absorption and EPR spectroscopy.

**Effect of NaOH concentration.** To investigate the effect of hydroxide on NCs growth, the concentration of NaOH was gradually increased from 0.5 to 1.5 M keeping all other conditions unchanged. The PXRD pattern displayed in Figure 5.7 shows that (1) $BaTiO_3$ phase formation requires more than 0.5 M NaOH concentration and (2) NCs size increases at higher NaOH concentration as summarized in Table 5.1. In addition to that, the solubility of NCs in hexanes also decreases with increased NaOH. Therefore, we employed 1 M NaOH for all follow-up experiments.

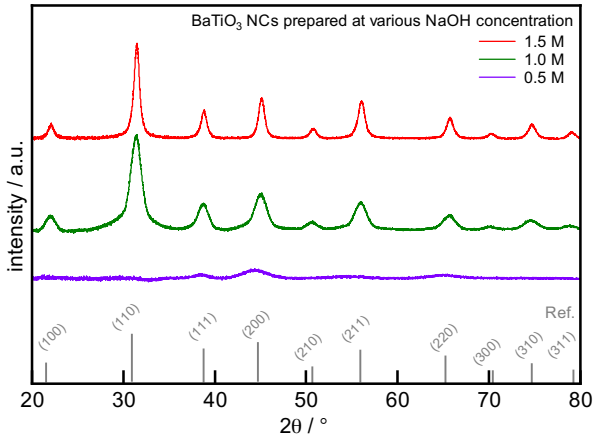


**Figure 5.7** Powder X-ray diffraction patterns of $BaTiO_3$ NCs prepared with different NaOH concentrations at 215 °C for 24 hours.

**Table 5.1** The average lattice parameter and crystallite size of $BaTiO_3$ NCs prepared with different NaOH concentrations at 215 °C for 24 hours.

| [NaOH] (M) | Lattice parameter (Å) | Crystallite size (nm)† |
|---|---|---|
| 1.5 | 4.0161 | 11.5 ± 0.41 |
| 1.0 | 4.0230 | 6.1 ± 0.37 |
| 0.5 | -- | -- |

†Crystallite size is the average size calculated from the three most intense reflections: (110), (200) and (211) using Rigaku SmartLab Studio II

**Effect of temperature.** To achieve the optimized growth temperature, hydrothermal synthesis was carried out at different temperatures. The PXRD analysis shows that a high temperature (> 200 °C) is required for the $BaTiO_3$ phase formation. The analysis summarized in Table 5.2 indicates no significant effect on crystallite size between these three temperatures.

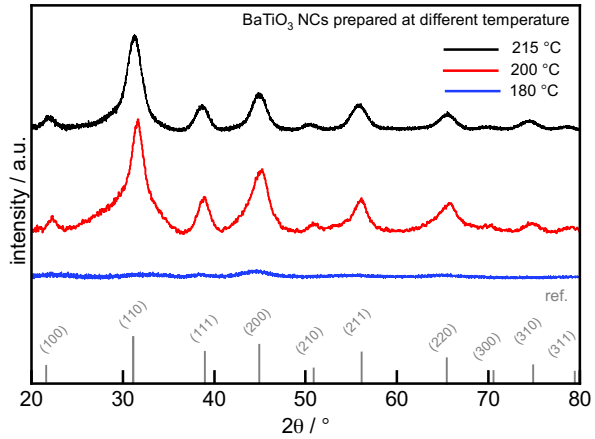

**Figure 5.8** Powder X-ray diffraction patterns of $BaTiO_3$ NCs prepared at different temperatures.

**Table 5.2** The average lattice parameter and crystallite size of $BaTiO_3$ NCs prepared at different temperatures and 1 M NaOH.

| Prep. Temp. (˚C) | Lattice parameter (Å) | Crystallite size (nm)† |
|---|---|---|
| 180 | -- | -- |
| 200 | 4.044 | 4.29 ± 0.91 |
| 215 | 4.033 | 4.42 ± 0.54 |

†Crystallite size is the average size calculated from the three most intense reflections: (110), (200) and (211) using Rigaku SmartLab Studio II

**Evolution of $BaTiO_3$ phase and dopant incorporation.** The growth of $BaTiO_3$ phase was studied by synthesizing the NCs for various times. The PXRD data suggests that phase of $BaTiO_3$ starts growing at a very short time and then NCs size continuously grow in size with increased time, as summarized in Figure 5.9 and Table 5.3. To analyze the dopant incorporation with increased time, EPR measurements and ICP-OES analysis were performed (see Figure 5.10 and Table 5.4). The measurements show that dopant incorporation happens as the NCs grow in size.

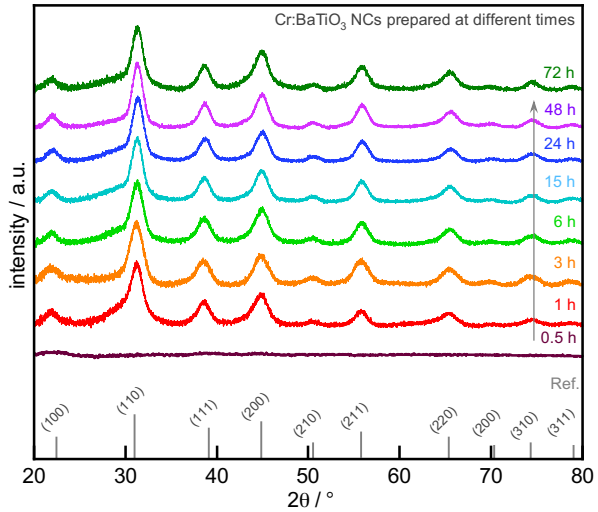


**Figure 5.9** Powder X-ray diffraction pattern of NCs prepared at different times showing the evolution of $BaTiO_3$ phase.

**Table 5.3** The average lattice parameter and crystallite size of $BaTiO_3$ NCs prepared at different times and 215 °C.

| Time (h) | Lattice parameter (Å) | Crystallite size (nm)† |
|---|---|---|
| 0.5 | -- | -- |
| 1 | 4.034 | 3.69 ± 1.4 |
| 3 | 4.033 | 4.31 ± 0.48 |
| 6 | 4.051 | 5.00 ± 0.39 |
| 15 | 4.055 | 5.40 ± 0.62 |
| 24 | 4.0497 | 5.36 ± 0.38 |
| 48 | 4.0404 | 5.61 ± 0.85 |
| 72 | 4.0348 | 5.67 ± 0.68 |

†Crystallite size is the average size calculated from the three most intense reflections: (110), (200) and (211) using Rigaku SmartLab Studio II

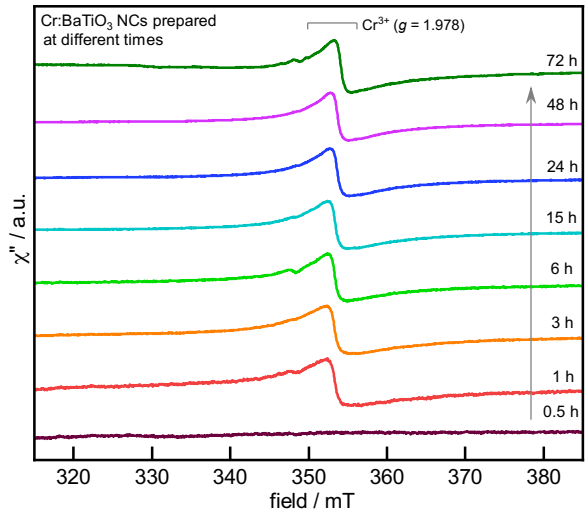


**Figure 5.10** Room temperature EPR spectra of Cr-doped $BaTiO_3$ NCs prepared at various times. The resonance at $g$ = 1.978 is attributed to $Cr^{3+}$ substituted at $Ti^{3+}$ sites.

**Table 5.4** ICP-OES analysis of Cr-doped $BaTiO_3$ NCs prepared at different times.

| Time (h) | Nominal Cr content (%) | ICP-OES Cr content (%) † |
|---|---|---|
| 0.5 | 0.1 | 0.253 |
| 1 | 0.1 | 0.297 |
| 3 | 0.1 | 0.263 |
| 6 | 0.1 | 0.271 |
| 15 | 0.1 | 0.282 |
| 24 | 0.1 | 0.313 |
| 48 | 0.1 | 0.290 |
| 72 | 0.1 | 0.290 |

†The percentage of Cr is calculated based on total Ti content in NCs samples

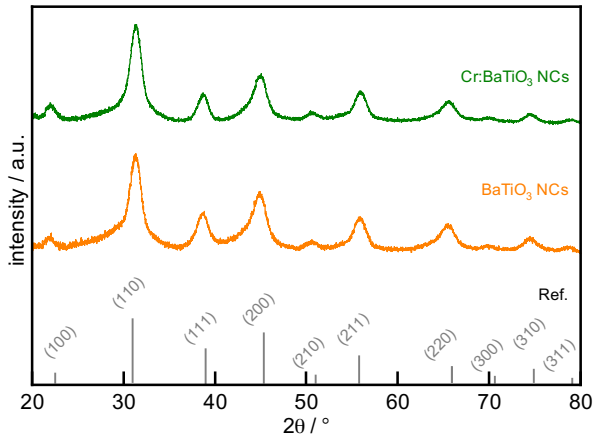


**Figure 5.11** Powder x-ray diffraction patterns of $BaTiO_3$ and Cr:$BaTiO_3$ NCs indexed to cubic phase of $BaTiO_3$ with space group $pm\bar{3}m$.

**Table 5.5** The lattice parameters and crystallite size of $BaTiO_3$ and Cr:$BaTiO_3$ NCs determined from powder X-ray diffraction patterns.

| Sample NCs | Lattice parameter (Å) | Crystallite size (nm)† |
|---|---|---|
| $BaTiO_3$ | 4.0400 | 5.25 ± 0.58 |
| Cr:$BaTiO_3$ | 4.0272 | 5.18 ± 0.90 |

†Crystallite size is the average size calculated from the following reflections: (110), (200) and (211) using Rigaku SmartLab Studio II.

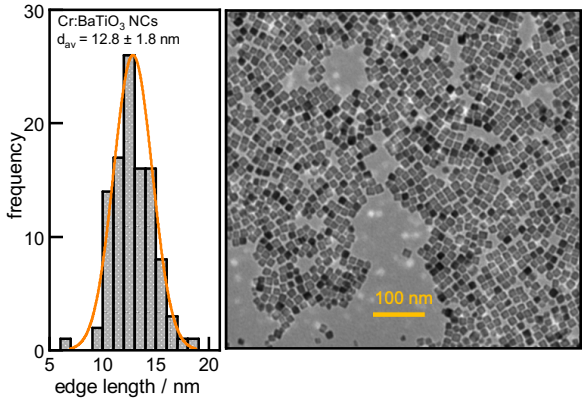


**Figure 5.12** Transmission electron microscopy image of as-prepared Cr:$BaTiO_3$ NCs and size distribution plot showing the average edge length.

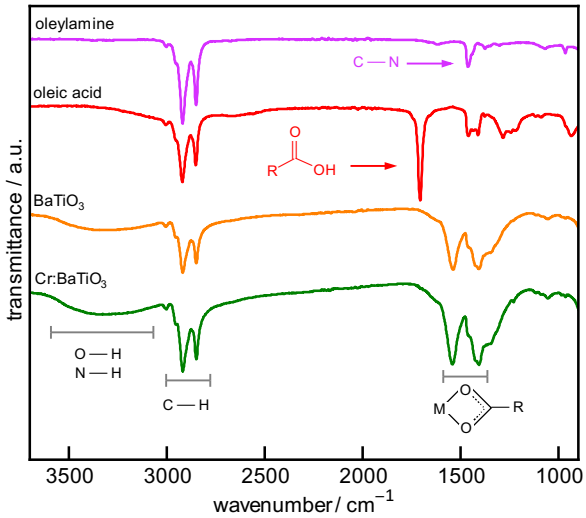


**Figure 5.13** FTIR spectra of solvent-evaporated $BaTiO_3$ (orange) and $Cr:BaTiO_3$ (green) NCs compared to free oleic acid and oleylamine.

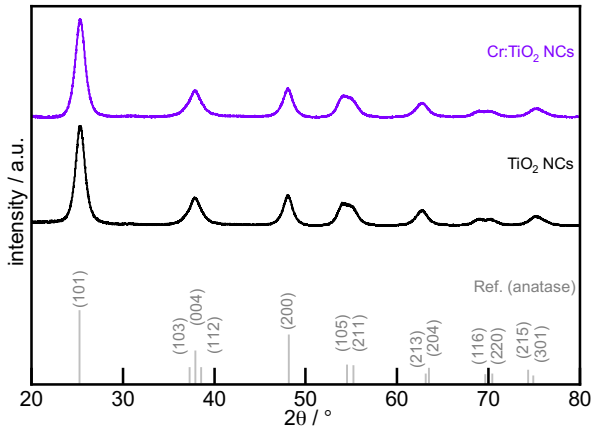


**Figure 5.14** Powder X-ray diffraction pattern of $TiO_2$ and Cr-doped $TiO_2$ indexed to anatase crystal structure.

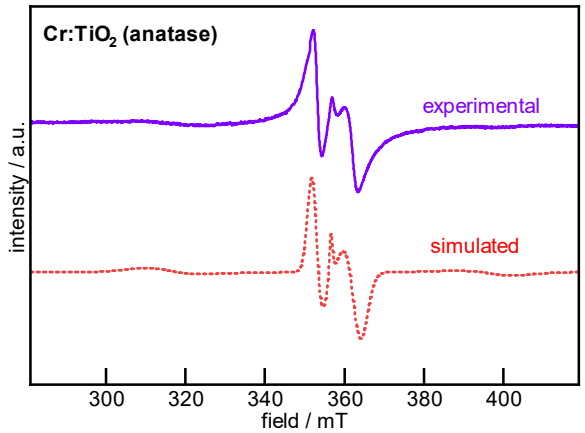


**Figure 5.15** Room temperature EPR spectrum of 0.1% Cr-doped $TiO_2$ NCs compared to simulated EPR spectrum using EasySpin.

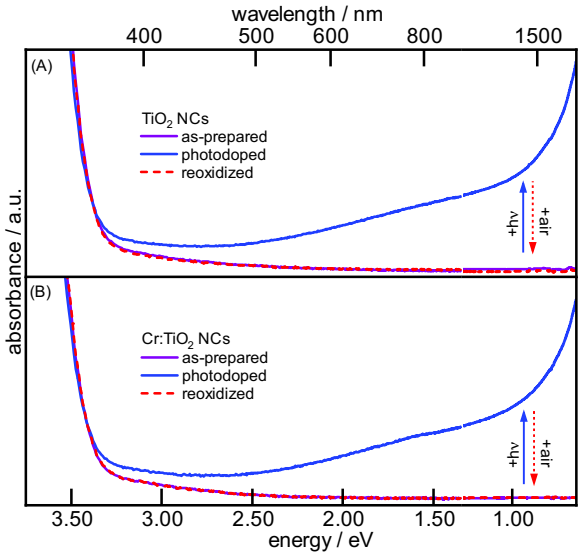


**Figure 5.16** Electronic absorption spectra of as-prepared, photodoped and reoxidized samples of (A) $TiO_2$ and (B) Cr:$TiO_2$ NCs.

## 5.5 References

(1) Chandra, P. Multifunctionality goes quantum critical. *Nat. Mater.* **2019,** *18* (3), 197.

(2) Ohno, H. A window on the future of spintronics. *Nat. Mater.* **2010,** *9* (12), 952-954.

(3) Rani, N.; Chahal, S.; Kumar, P.; Shukla, R.; Singh, S. Role of oxygen vacancies for mediating ferromagnetic ordering in La-doped MgO nanoparticles. *J. Supercond. Novel Magn.* **2019**, 1-8.

(4) Xing, P.; Chen, Y.; Yan, S.-S.; Liu, G.; Mei, L.; Zhang, Z. Tunable ferromagnetism by oxygen vacancies in Fe-doped $In_2O_3$ magnetic semiconductor. *J. Appl. Phys.* **2009,** *106* (4), 043909.

(5) Schwartz, D. A.; Kittilstved, K. R.; Gamelin, D. R. Above-room-temperature ferromagnetic $Ni^{2+}$-doped ZnO thin films prepared from colloidal diluted magnetic semiconductor quantum dots. *Appl. Phys. Lett.* **2004,** *85* (8), 1395-1397.

(6) Norberg, N. S.; Kittilstved, K. R.; Amonette, J. E.; Kukkadapu, R. K.; Schwartz, D. A.; Gamelin, D. R. Synthesis of colloidal $Mn^{2+}$: ZnO quantum dots and high-$T_C$ ferromagnetic nanocrystalline thin films. *J. Am. Chem. Soc.* **2004,** *126* (30), 9387-9398.

(7) Sinha, M.; Pearson, T. J.; Reeder, T. R.; Vivanco, H. K.; Freedman, D. E.; Phelan, W. A.; McQueen, T. M. Introduction of spin centers in single crystals of $Ba_6CaWO_{6-\delta}$. *Phys. Rev. Mater.* **2019,** *3* (12), 125002.

(8) Sato, K.; Dederichs, P.; Katayama-Yoshida, H.; Kudrnovský, J. Exchange interactions in diluted magnetic semiconductors. *J. Phys.: Condens. Matter* **2004,** *16* (48), S5491.

(9) Vlaskin, V. A.; Beaulac, R.; Gamelin, D. R. Dopant– carrier magnetic exchange coupling in colloidal inverted core/shell semiconductor nanocrystals. *Nano Lett.* **2009,** *9* (12), 4376-4382.

(10) Polking, M. J.; Han, M.-G.; Yourdkhani, A.; Petkov, V.; Kisielowski, C. F.; Volkov, V. V.; Zhu, Y.; Caruntu, G.; Alivisatos, A. P.; Ramesh, R. Ferroelectric order in individual nanometre-scale crystals. *Nat. Mater.* **2012,** *11* (8), 700-709.

(11) Rabuffetti, F. A.; Brutchey, R. L. Structural evolution of $BaTiO_3$ nanocrystals synthesized at room temperature. *J. Am. Chem. Soc.* **2012,** *134* (22), 9475-9487.

(12) Costanzo, T.; McCracken, J.; Rotaru, A.; Caruntu, G. Quasi-monodisperse transition-metal-doped $BaTiO_3$ (M = Cr, Mn, Fe, Co) colloidal nanocrystals with multiferroic properties. *ACS Appl. Nano Mater.* **2018,** *1* (9), 4863-4874.

(13) Verma, K. C.; Kotnala, R. Multiferroic approach for Cr, Mn, Fe, Co, Ni, Cu substituted $BaTiO_3$ nanoparticles. *Mater. Res. Express* **2016,** *3* (5), 055006.

(14) Berglund, C.; Braun, H. Optical absorption in single-domain ferroelectric barium titanate. *Phys. Rev.* **1967,** *164* (2), 790.

(15) Ju, L.; Sabergharesou, T.; Stamplecoskie, K. G.; Hegde, M.; Wang, T.; Combe, N. A.; Wu, H.; Radovanovic, P. V. Interplay between size, composition, and phase transition of nanocrystalline $Cr^{3+}$-doped $BaTiO_3$ as a path to multiferroism in perovskite-type oxides. *J. Am. Chem. Soc.* **2012,** *134* (2), 1136-1146.

(16) Eden, S.; Kapphan, S.; Hesse, H.; Trepakov, V.; Vikhnin, V.; Gregora, I.; Jastrabik, L.; Seglins, J. Observations of the absorption, infra-red emission, and excitation spectra of Cr in $BaTiO_3$. *J. Phys.: Condens. Matter* **1998,** *10* (47), 10775.

(17) Eden, S.; Kapphan, S.; Hesse, H.; Trepakov, V.; Vikhnin, V.; Jastrabik, L.; Gregora, I. Near infra-red luminescence of $BaTiO_3$:Cr. *Radiat. Eff. Defects Solids* **1999,** *149* (1-4), 107-112.

(18) Shannon, R. D. Revised effective ionic radii and systematic studies of interatomic distances in halides and chalcogenides. *Acta Crystallogr. Sect. A: Found. Crystallogr.* **1976,** *32* (5), 751-767.

(19) Lehuta, K. A.; Kittilstved, K. R. Speciation of Cr(iii) in intermediate phases during the sol–gel processing of Cr-doped $SrTiO_3$ powders. *J. Mater. Chem. A* **2014,** *2* (17), 6138-6145.

(20) Harrigan, W. L.; Michaud, S. E.; Lehuta, K. A.; Kittilstved, K. R. Tunable electronic structure and surface defects in chromium-doped colloidal $SrTiO_{3-\delta}$ nanocrystals. *Chem. Mater.* **2016,** *28* (2), 430-433.

(21) Harrigan, W. L.; Kittilstved, K. R. Reversible modulation of the $Cr^{3+}$ spin dynamics in colloidal $SrTiO_3$ nanocrystals. *J. Phys. Chem. C* **2018,** *122* (46), 26652-26657.

(22) Abdullah, M.; Kittilstved, K. R.; Nelson, R. J. Tunable redox activity at $Fe^{3+}$ centers in colloidal $ATiO_3$ (A = Sr and Ba) nanocrystals. *Chem. Mater.* **2021**.

(23) Joost, U.; Šutka, A.; Oja, M.; Smits, K.; Döbelin, N.; Loot, A.; Järvekülg, M.; Hirsimäki, M.; Valden, M.; Nõmmiste, E. Reversible photodoping of $TiO_2$ nanoparticles for photochromic applications. *Chem. Mater.* **2018,** *30* (24), 8968-8974.

(24) De Trizio, L.; Buonsanti, R.; Schimpf, A. M.; Llordes, A.; Gamelin, D. R.; Simonutti, R.; Milliron, D. J. Nb-doped colloidal $TiO_2$ nanocrystals with tunable infrared absorption. *Chem. Mater.* **2013,** *25* (16), 3383-3390.

(25) Schrauben, J. N.; Hayoun, R.; Valdez, C. N.; Braten, M.; Fridley, L.; Mayer, J. M. Titanium and zinc oxide nanoparticles are proton-coupled electron transfer agents. *Science* **2012,** *336* (6086), 1298-1301.

(26) Di Valentin, C.; Pacchioni, G.; Selloni, A. Reduced and n-type doped $TiO_2$: nature of $Ti^{3+}$ species. *J. Phys. Chem. C* **2009,** *113* (48), 20543-20552.

# CHAPTER 6

# INVESTIGATING THE PHOTODOPING AND CARRIER DENSITIES OF COLLOIDAL STRONTIUM TITANATE NANOCRYSTALS

## 6.1 Introduction

The generation and manipulation of the charge carriers in semiconducting materials give rise to new exciting properties which are fundamental to their use in optoelectronic, solar-energy conversions and redox-based applications.[1-3] The examples include carrier-induced ferromagnetic ordering in ZnO, MgO and $EuTiO_3$ nanostrcures[4-6] and the reversible control of the dopants oxidation state in $SrTiO_3$ bulk powders.[7] The interactions between n-type carriers and other defects are susceptible to the nature of host material, and they change significantly from bulk to nanoscale lattices. For instance, the addition of extra electrons in Cr-doped colloidal $SrTiO_3$ NCs modulates the spin-dynamic of $Cr^{3+}$ dopants while the same carriers cause the reduction of the higher oxidation states of Cr dopant in bulk powder.[8,9] Similarly, reversible electron accumulation in ZnO NCs has recently gained a lot of interest for energy storage applications.[10] To study the interactions of these carriers in semiconductors, some examples of successful strategies to introduce extra electrons include photochemical, electrochemical and aliovalent doping.[11-13] Among these approaches, photochemical reduction is the most extensively investigated method for modulating carrier densities and is widely applicable to colloidal nanocrystals.[1,14] It has been demonstrated that kinetics of electrons accumulation and their densities in ZnO NCs are sensitive to nature and concentration of molecular reductant, size of the nanocrystals and identity of counter-cation to stabilize the added electrons.[3,15]

However, photochemical electrons doping of colloidal $SrTiO_3$ NCs, its dependence on sacrificial reductant and solvent, and their effect on carrier densities remain elusive.

In this study, a photochemical method for introducing extra charge carriers in colloidal $SrTiO_3$ NCs is discussed. Photoexcitation of $SrTiO_3$ NCs in the presence of a sacrificial hole quencher such as ethanol produces extra electrons that are stable indefinitely under anaerobic conditions. Electron paramagnetic resonance (EPR) and electronic absorption spectroscopies measurements provide evidence that these electrons are localized at $Ti^{3+}$ trap sites. The effect of sacrificial hole quencher and irradiation time on the rate of electrons accumulation is thoroughly discussed. We also estimated the average carrier densities per NC by chemical titration against the known concentration of oxidizing agent and find it exceeds that found for other know semiconductors.

**6.2 Results and Discussion**

The synthesis and characterization of $SrTiO_3$ NCs were completed by following our recent work.[16] The photodoping experiments were performed on as-prepared $SrTiO_3$ NCs following the previously reported method.[9] Briefly, UV irradiation of an anaerobic solution of as-prepared NCs creates electron/hole pairs (excitons) followed by the rapid quenching of holes with sacrificial reductant which leaves excess electrons in the NCs. Figure 6.1 shows the electronic absorption spectra of $SrTiO_3$ NCs as a function of photodoping time. The absorption spectrum of as-prepared NCs is dominated by the bandgap energy above ~3.25 eV. With increased photodoping time, the physical appearance of the sample changes to dark blue and a new absorption feature extends throughout the entire visible region and is centered

at ~1.5 eV (900 nm). This broad near-IR transition is assigned to the metal-to-metal charge transfer (MMCT) transition from localized $Ti^{3+}$ sites to the conduction band reported previously in photodoped $SrTiO_3$ and $TiO_2$.[17,18] We have no evidence that photodoping creates free or delocalized electrons in the conduction band ($e^-_{CB}$). Recent reports showed that n-type doping of small anatase $TiO_2$ NCs could lead to accumulation of $e^-_{CB}$ as observed spectroscopically.[19,20] The presence of free electrons causes significant blue-shifts in the band-edge energy from the Moss-Burstein effect with the formation of a localized surface plasmon resonance (LSPR) in the mid-IR region. The lack of both the absorption in the mid-IR region and the Moss-Burstein effect confirms that $e^-_{CB}$ are absent in our photodoped $SrTiO_3$ NCs. Instead, photochemically added electrons create quasi-localized $Ti^{3+}$ defects ($S = ½$) which can be observed in the EPR spectrum of photodoped NCs (see SI Figure 6.5).

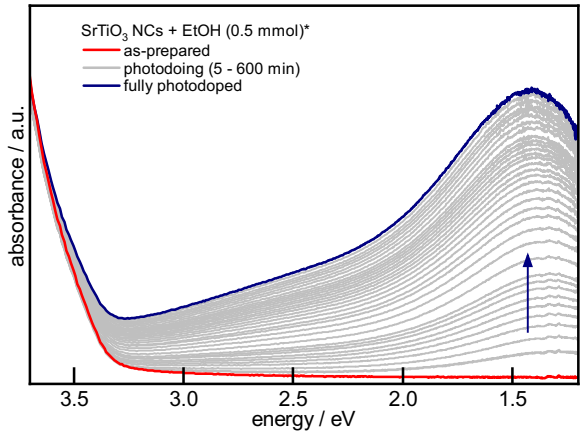


**Figure 6.1** Electronic absorption spectra of $SrTiO_3$ NCs as a function of photodoping time in the presence of ethanol (0.5 mmol) as a sacrificial reductant. The blue arrow shows the progression of date with time.

Although the continuous growth of the absorption feature with increased photodoping time shows the successive addition of electrons, it does not represent the rate of electron accumulation. To gain further insight into it, the relative absorbance at 800 nm ($A_{\text{photodoped}} - A_{\text{as-prepared}}$) plotted against time is displayed in

Figure 6.2. The absorbance (light-blue circle for the data extracted from absorption measurements in Figure 6.1) shows a rapid growth at the initial stages of photodoping which eventually reaches the plateau. The photophysical origin of this rapid increase followed by a slow accumulation of electrons could be various competing processes during the photodoping, as discussed following. The successful electron addition is fundamentally governed by the reactivity of photogenerated holes towards (i) sacrificial reductant, i.e., EtOH and (ii) recombination processes, as demonstrated in Figure 6.3. Each hole being transferred to the sacrificial reductant would result in the addition of one electron. However, after the successful addition of the first electron, further electron accumulation gets complicated, and it must have to go through trion recombination involving already-added electrons and the sacrificial reductant as discussed previously by Schimpf and coworkers in photodoped ZnO NCs.[15] If photogenerated holes are recombined with already-added electrons before they are transferred to sacrificial reductant, further electron addition will not happen. For the successive electron addition, the sacrificial reductant must beat the recombination processes. The relative absorbance in Figure 6.2 shows that one-half of the maximum photodoping is achieved within the first 100 min, and the remaining half is slowly attained in the next 500 min. We speculate that a higher concentration of EtOH as sacrificial reductant (0.5 mmol (29 μL) = $10^3$ x [NCs]) and relatively a few added electrons at the early stages of photodoping make the hole quenching reaction much effective. However, every successive electron addition makes the recombination processes more competitive and EtOH less effective, slowing down the accumulation of electrons as the photodoping time progresses.

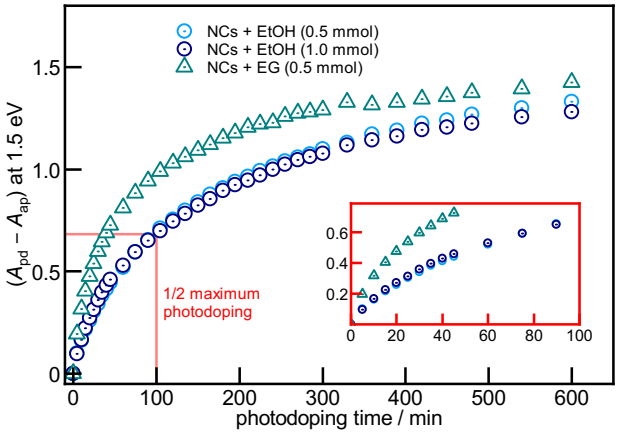


**Figure 6.2** The increase in absorbance at 800 nm as a function of photodoping in the presence of two different concentrations of ethanol (0.5 and 1 mmol) and ethylene glycol as sacrificial reductant.

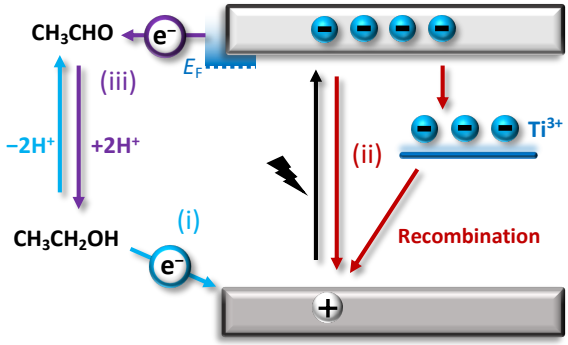


**Figure 6.3** Schematic band structure of $SrTiO_3$ NCs demonstrating the various electron transfer processes during photodoping.

To test the dependence of this electron accumulation on the concentration of sacrificial reductant, the photodoping experiments were performed on the same batch of samples under identical conditions but double the EtOH concentration (1 mmol) and a different sacrificial reductant ethylene glycol (EG) (see SI Figure 6.6 and 6.7). The relative absorbance at 800 nm for both samples plotted against photodoping time is shown in Figure 6.2. The relative change in the absorbance indicates that the rate of electrons accumulation is negligibly faster when the concentration of EtOH is increased to 1 mmol. There are no significant changes in the time scale in achieving ½-maximum photodoping (see inset Figure 6.2). We suspect that the concentration of EtOH (0.5 mmol) is already in significant excess, effectively carrying out the hole scavenging reaction. Furthermore, there is a diffusion limit as well. Therefore, any

further increase in EtOH concentration is not significantly affecting the rate of electron accumulation. For the samples being photodoped in the presence of EG, there is a dramatic increase in the changes in absorbance over time. It quickly reaches the ½-maximum photodoping in about 50 min compared to 100 min with EtOH (see Figure 6.2 insets). This drastic difference in the rate of electron addition between EtOH and EG possibly arises from their relative reactivities towards holes and the number of electrons they can donate per molecule. Theoretically, each EtOH molecule as a sacrificial reductant donates two electrons upon its complete oxidation to acetaldehyde. The H-NMR data collected on the photodoped samples with EtOH shows a signature low-field peak for aldehydic proton at ~9.6 ppm (see SI Figure 6.8). However, methyl protons of acetaldehyde are not observed, and we suspect they might have been occluded by the broad signals from surface-bound oleate ligands. Nevertheless, the peak at ~9.6 ppm suggests that at least a fraction of EtOH is oxidized to acetaldehyde during photodoping. The H-NMR spectrum collected on NCs photodoped with EG also shows a peak at ~9.6 ppm (see SI Figure 6.9) which we attribute to the presence of acetaldehyde from the oxidation of residual EtOH from washing procedures. We do not observe any other low-field signal in the H-NMR spectrum.

EG has been previously reported as a highly effective sacrificial reductant to suppress the photoexcited charge recombination in $TiO_2$ nanoparticles.[21,22] The oxidation of EG produces a mixture of various products, including but not limited to glycolaldehyde, acetaldehyde, formaldehyde, formic acid, and the multiple electrons. However, the mechanisms of such degradation reactions are still unknown. We

speculate that twice the number of active functional groups (-OH) in EG compared to EtOH and its multiple electron donation abilities can play a key role in the faster electron accumulation at the initial stages of photodoping. Although photodoping with EtOH and EG have different rates, they eventually reach about a similar absorbance where further UV irradiation yields no significant changes. The microscopic origin of this saturation has been previously identified as the reduction of acetaldehyde back to EtOH in photodoped ZnO NCs.[3] This hydrogenation reaction is sensitive to changes in Fermi level which at low electron densities is negligible but dominates with increased photodoping time (see pathway iii in Figure 6.3). The saturation in absorbance with prolonged photodoping time suggests the exitance of limit for electron doping in these $SrTiO_3$ NCs. This further motivated us to determine the maximum number of electrons added in these photodoped colloidal NCs.

Although stable indefinitely under anaerobic conditions, these photodoped NCs can be reversed quantitatively by simply reoxidizing the samples with air.[9,17] This reversibility makes the photodoped colloidal NCs amenable to direct redox titration to estimate the added electrons, something not practicable with chemically reduced bulk powders.[7] The detailed method for determining the added electrons was adopted from a procedure developed by Mayer *et al*. on colloidal ZnO and $TiO_2$ nanoparticles.[18] The typical method involves (1) the preparation of colloidal solution with the known concentration of NCs, (2) photodoping of the NCs to their maximum level, and (3) titration against one-electron oxidant under strictly air-free conditions. Briefly, the concentration of colloidal NCs was determined by the combination of the average amount of titanium per NC from size analysis from x-ray diffraction pattern

(see SI Figure 6.10 and Table 6.1-6.2) and the total titanium content in the stock solution from ICP-OES analysis (see SI Figure 6.11-12 and Table 6.3). Since there is one titanium per unit cell of $SrTiO_3$, the concentration of NCs can be estimated from ratiometric analysis as summarized in Table 6.4.

For the photodoping experiments, NCs suspended in hexanes of know molarity were photodoped by prolonged exposure to UV irradiation in the presence of EtOH (1 mmol). The UV-Vis absorption measurements were taken periodically during the entire photodoping process. When absorption did not change over an exposure of a few hours, NCs were considered to have reached their maximum photodoping level. The average number of electrons added per NC ($n_e$) was estimated by stoichiometric chemical titration against TEMPO with known molarity using a customized air-tight glass setup (see SI Figure 6.13 and Table 6.5). In a typical titration experiment, aliquots of a freshly prepared toluene solution of TEMPO were added to the photodoped samples under constant stirring. The absorption measurements were taken after each aliquot addition, as shown in Figure 6.4A (see Figure 6.14-15 for replicate experiments). The complete elimination of absorption attributing to added electrons was considered an endpoint of the titration.

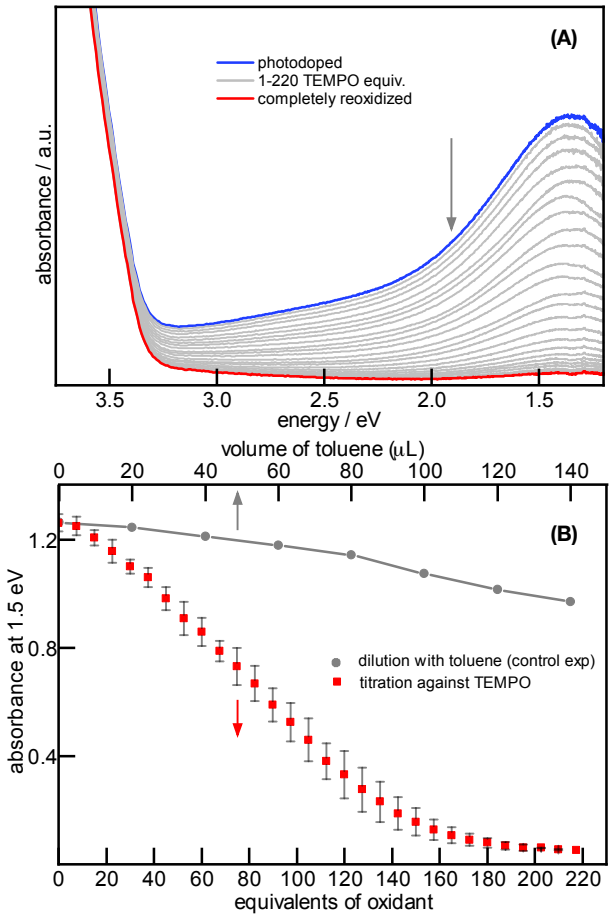


**Figure 6.4** (A) Electronic absorption spectra of photodoped NCs with the sequential addition of TEMPO. (B) The change in absorbance at 1.5 eV plotted against the equivalent of TEMPO as an oxidizing agent. The error bars are shown in grey vertical capped lines and the top grey data shows the change in absorbance of photodoped NCs with the addition of blank toluene as a control experiment.

The changes in the absorbance at 1.5 eV with the addition equivalents on TEMPO along with the toluene plotted in Figure 6.4B shows a complete elimination at ~180 equivalents. Since TEMPO is a one-electron oxidant, this equates to $n_e$ = 180 (see supporting information for detailed calculations). This number for $SrTiO_3$ here exceeds the previous reports on amorphous $TiO_2$ nanoparticles ($n_e$ = 72) and ZnO NCs ($n_e$ = 5).[18] We suspect that the large size of $SrTiO_3$ NCs (~7 nm compared to 3 nm $TiO_2$) can lead to this difference in number of elections accumulated with photodoping. Brozek *et al.* recently reported a spike in electron accumulation ($n_e$ = 250) in Fe-doped ZnO NCs.[10] In these NCs, $Fe^{3+/2+}$ redox level is located below the

conduction band which acts as a trap site for photoexcited carriers facilitating the electron accumulation.[23] We have also recently seen a similar electron addition at $Fe^{3+/2+}$ dopant sites in colloidal $SrTiO_3$ and $BaTiO_3$ NCs.[17] In this report, we presented a band structure of Ti(IV)-oxide nanocrystals where $Fe^{3+/2+}$ dopant level is located below the $Ti^{4+/3+}$ trap states. Although both redox levels are shallow trap centers, $Fe^{3+/2+}$ could not only serve a better trap center due to its relatively lower position than the $Ti^{4+/3+}$ level; it can also offer a tunable carrier density by simply depending on the dopant concentration. The experiments to explore the electron accumulation in doped $SrTiO_3$ would be an interesting future aspect for this work.

### 6.3 Supporting Information

**Synthesis of colloidal $SrTiO_3$ NCs.** The synthesis of colloidal $SrTiO_3$ NCs was carried out by a modified hydrothermal method reported earlier by Harrigan *et al*.[24] In a typical synthesis of 1.25 mmol of TALH and 1.25 mmol $Sr(OH)_2{\cdot}8H_2O$ were dissolved in 30 mL of distilled water. The pH of the solution was then adjusted to 12.1 with an aqueous solution of $NMe_4OH$ (10 M) followed by the addition of oleic acid (2.5 mmol) and hydrazine (5 mmol). The resulting solution was transferred to a 45 mL Teflon-lined autoclave (4744 General Purpose Acid Digestion Vessel, Parr Instrument Company) and heated to 200 °C in an oven for 24 hours. The resulting NCs were collected, washed with ethanol several times, suspended in hexanes, and sonicated for about 30 minutes to produce a cloudy suspension. Finally, a transparent hexane layer containing NCs was extracted by centrifuging the cloudy suspension (5 min at 4000 rpm). These NCs can be further purified by precipitation with ethanol.

**Photodoping of NCs**. The photodoping experiments were performed to introduce excess electrons in as-prepared NCs. Sample preparation was completed in the argon-filled glove box where NCs suspended in hexanes were transferred to a 1 cm air-tight cuvette before removal. Samples were photodoped by prolonged exposure to unfocused irradiation from 75 W xenon lamp in the presence of EtOH as a sacrificial reductant. The electronic absorption spectra were taken periodically during the entire photodoping process. It was estimated that the NCs were photodoped to their saturation limit when no further spectroscopic changes could be observed following prolonged exposure to UV irradiation.

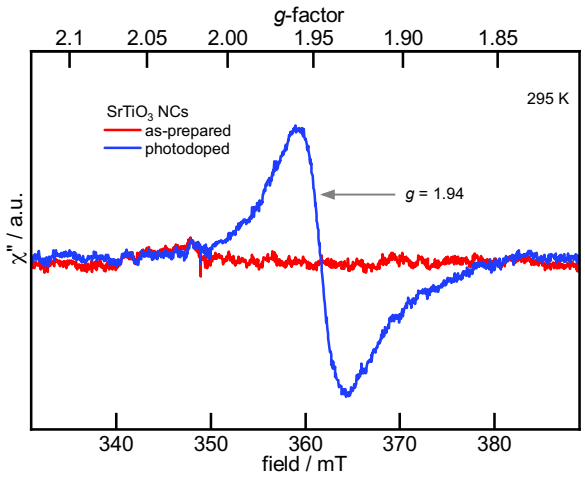


**Figure 6.5** Room temperature EPR spectra of as-prepared and photodoped of $SrTiO_3$ NCs.

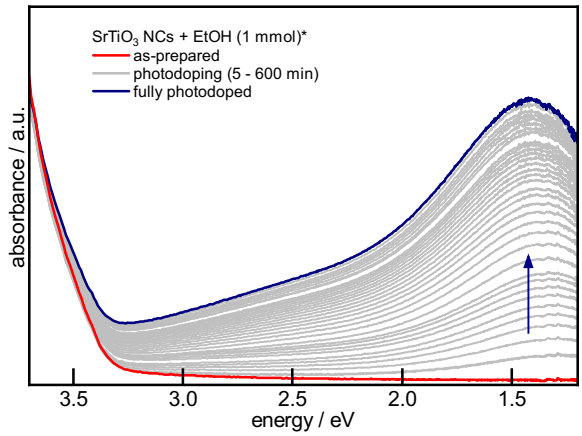


**Figure 6.6** UV-vis spectra of $SrTiO_3$ NCs taken periodically during photodoping in the presence of EtOH (1 mmol).

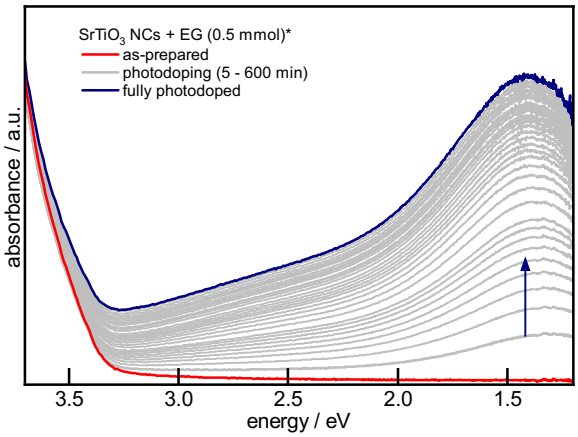


**Figure 6.7** UV-vis spectra of $SrTiO_3$ NCs taken periodically during photodoping in the presence of ethylene glycol (0.5 mmol).

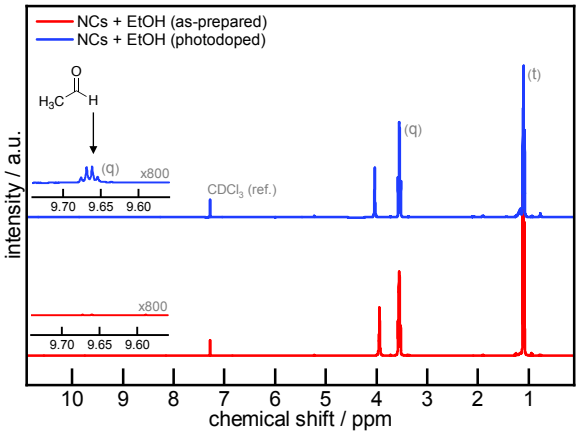


**Figure 6.8** H-NMR spectra of colloidal solution of $SrTiO_3$ NCs suspended in deuterated chloroform before and after the photodoping in the presence of EtOH as hole quencher.

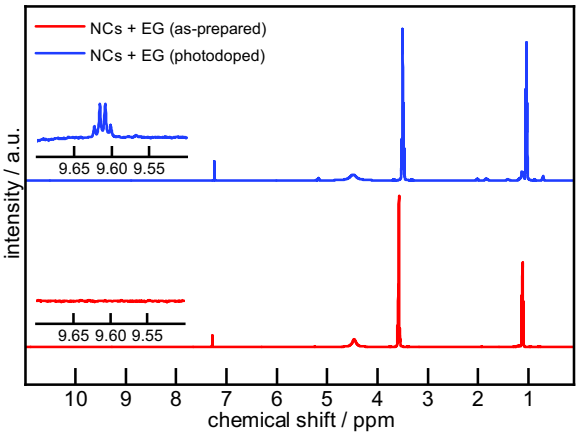


**Figure 6.9** H-NMR spectra of colloidal solution of $SrTiO_3$ NCs suspended in deuterated chloroform before and after the photodoping in the presence of EG as hole quencher.

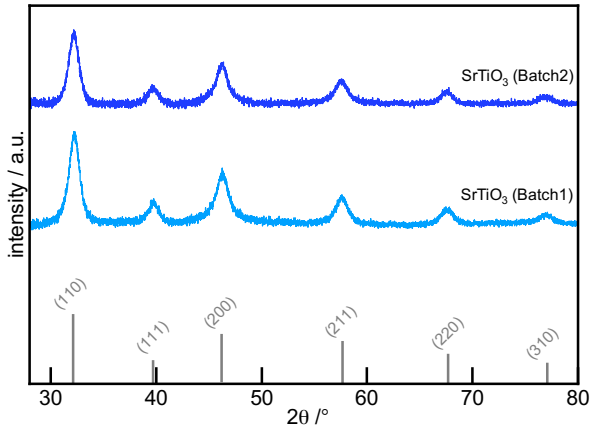


**Figure 6.10** Powder X-ray diffraction patterns of $SrTiO_3$ NCs prepared under identical conditions for average particle size analysis.

**Table 6.1** Determination of average particle size from powder diffraction analysis.

| $SrTiO_3$ NCs | Crystallite size from various reflections (nm) | | | | Average NCs size |
|---|---|---|---|---|---|
| | (110) | (111) | (200) | (211) | |
| Batch-1 | 7.172 | 7.177 | 6.962 | 6.889 | 6.974 ± 0.25 nm |
| Batch-2 | 7.165 | 7.185 | 6.556 | 6.690 | |

**Table 6.2** Determination of the average number of Ti per NC.

| | |
|---|---|
| Average lattice parameter | 3.924 Å |
| Average volume of unit cell | (3.924)3 = 60.42 Å3 |
| Average size of NCs | 69.74 Å |
| Average volume of NCs | (69.74)3 = 339192.18 Å3 |
| Number of unit cells per NC | 339192.18 / 60.42 = 5614 |
| Number of $Ti^{4+}$ per NC | 5614 |

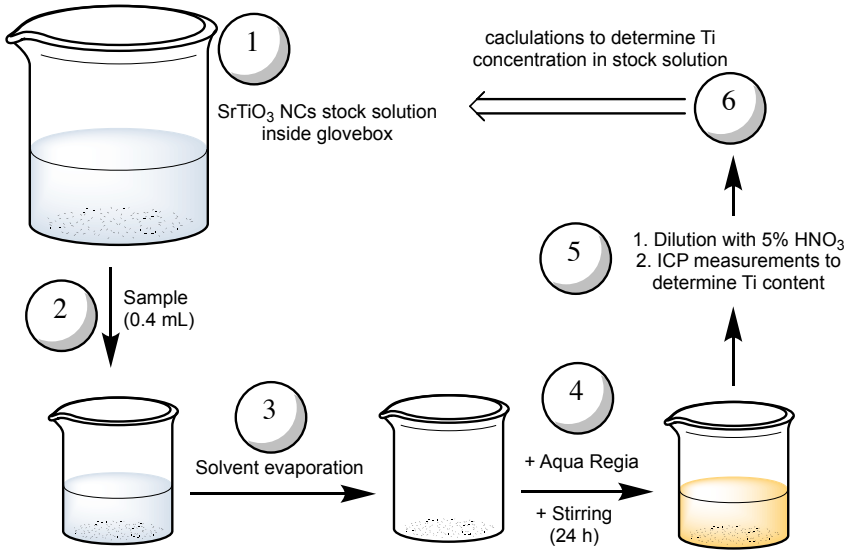


**Figure 6.11** Flow chart elaborating the sample preparation of ICP-OES measurements to determine the total titanium content in stock solution.

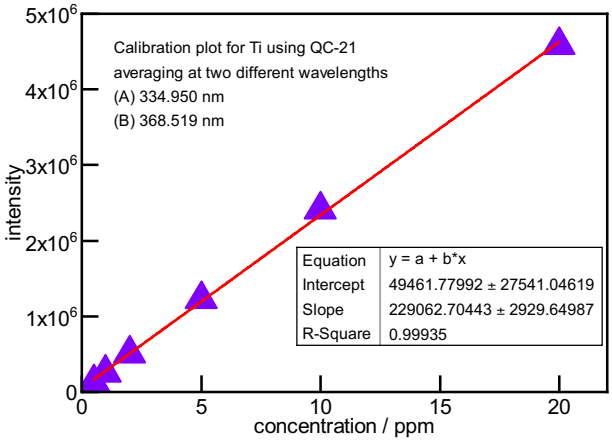


**Figure 6.12** Calibration plot for ICP-OES analysis using standard solutions of different concentrations.

**Table 6.3** Calculations to determine the total Ti content from ICP-OES data.

| $SrTiO_3$ NCs | Concentration of Ti (mg/L) | | | Molarity (mM) | Molarity of stock sol. (dilution factor = 20) |
|---|---|---|---|---|---|
| | 334.940 nm | 368.519 nm | Average | | |
| Sample-1 | 26.82 | 27.51 | 27.26 | 0.569 | 11.88 mM |
| Sample-2 | 27.11 | 27.32 | | | |
| Sample-3 | 27.23 | 27.57 | | | |

**Table 6.4** Determination of concentration of NCs in stock solution.

| | |
|---|---|
| Concentration of Ti in stock solution | 11.88 mM |
| Number of Ti making up one NC | 5614 |
| Concentration of NCs in stock solution | 0.00212 mM = 2.12 µM |

**Table 6.5** Preparation of stock solution of TEMPO of known concentration.

| | |
|---|---|
| Molecular weight | 186.27 |
| Amount taken | 23.9 mg |
| Volume of solution | 20 mL |
| Molarity of solution | 6.4 mM |

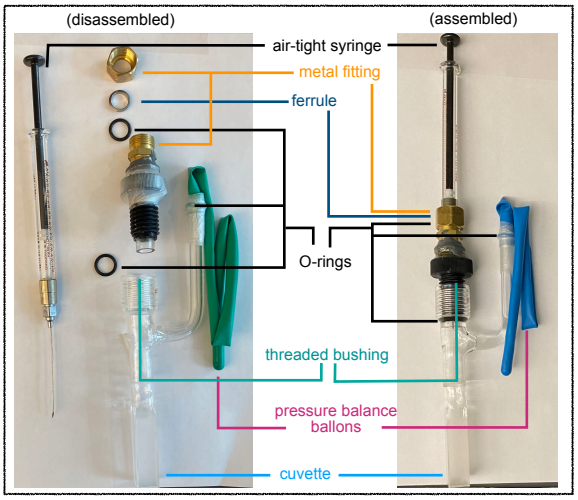


**Figure 6.13** Various components of air-free custom setup used titration experiments.

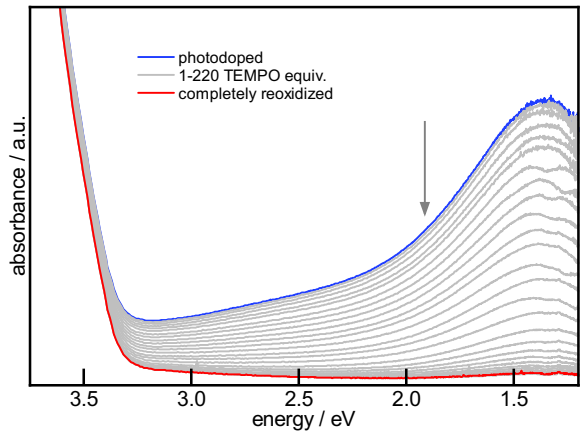


**Figure 6.14** UV-Vis spectra of photodoped NCs collected periodically during titration against TEMPO under air-free conditions (trial 1).

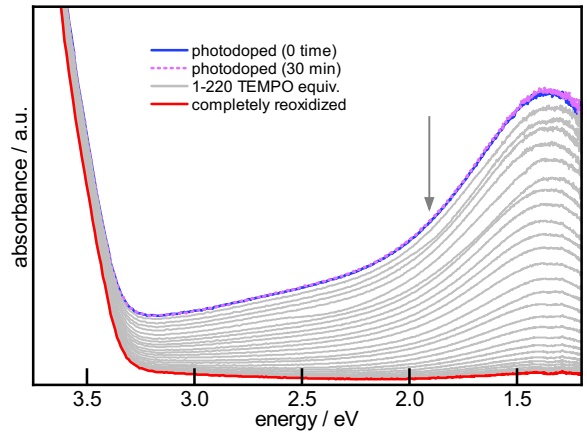


**Figure 6.15** UV-Vis spectra of photodoped NCs collected periodically during titration against TEMPO under air-conditionsition (trial 2). The pink spectrum represents the stability of photodoped NCs during transition between glovebox and air-tight custom setup outside the glovebox.

## Calculations to determine the number of electrons per NC:

Volume of photodoped NCs (0.00212 mM) = 2 mL (0.002L)
Number of moles of photodoped NCs = 0.00212 mmol / L * 2 mL = 0.00212 µmol / mL * 2 mL = 0.00424 µmol = 0.00000424 mmol

Volume of TEMPO (6.4 mM) added incrementally = 140 µL = 0.140 mL
Number of moles added = 6.4 mM x (0.140/1000) = 0.000896 mmol

Equivalents of TEMPO added against NCs = 0.000896/0.00000424 = 211
Equivalents of TEMPO added against NCs per increment = total equivalent / no. of data points = 211/28 = ~7.5

## 6.4 References

(1) Ichihara, F.; Sieland, F.; Pang, H.; Philo, D.; Duong, A.-T.; Chang, K.; Kako, T.; Bahnemann, D. W.; Ye, J. Photogenerated charge carriers dynamics on La- and/or Cr-doped $SrTiO_3$ nanoparticles studied by transient absorption spectroscopy. *J. Phys. Chem. C* **2020,** *124* (2), 1292-1302.

(2) Luther, J. M.; Jain, P. K.; Ewers, T.; Alivisatos, A. P. Localized surface plasmon resonances arising from free carriers in doped quantum dots. *Nat. Mater.* **2011,** *10* (5), 361-366.

(3) Carroll, G. M.; Schimpf, A. M.; Tsui, E. Y.; Gamelin, D. R. Redox potentials of colloidal n-type ZnO nanocrystals: effects of confinement, electron density, and fermi-Level pinning by aldehyde hydrogenation. *J. Am. Chem. Soc.* **2015,** *137* (34), 11163-11169.

(4) Ochsenbein, S. T.; Feng, Y.; Whitaker, K. M.; Badaeva, E.; Liu, W. K.; Li, X.; Gamelin, D. R. Charge-controlled magnetism in colloidal doped semiconductor nanocrystals. *Nat. Nanotechnol.* **2009,** *4* (10), 681-687.

(5) Rani, N.; Chahal, S.; Kumar, P.; Shukla, R.; Singh, S. Role of oxygen vacancies for mediating ferromagnetic ordering in La-doped MgO nanoparticles. *J. Supercond. Novel Magn.* **2019**, 1-8.

(6) Gui, Z.; Janotti, A. Carrier-density-induced ferromagnetism in $EuTiO_3$ bulk and heterostructures. *Phys. Rev. Lett.* **2019,** *123* (12), 127201.

(7) Mansoor, H.; Harrigan, W. L.; Lehuta, K. A.; Kittilstved, K. R. Reversible control of the Mn oxidation state in $SrTiO_3$ bulk powders. *Front. Chem.* **2019,** *7*, 353.

(8) Lehuta, K. A.; Kittilstved, K. R. Reversible control of the chromium valence in chemically reduced Cr-doped $SrTiO_3$ bulk powders. *Dalton Trans.* **2016,** *45* (24), 10034-10041.

(9) Harrigan, W. L.; Kittilstved, K. R. Reversible modulation of the $Cr^{3+}$ spin dynamics in colloidal $SrTiO_3$ nanocrystals. *J. Phys. Chem. C* **2018,** *122* (46), 26652-26657.

(10) Brozek, C. K.; Zhou, D.; Liu, H.; Li, X.; Kittilstved, K. R.; Gamelin, D. R. Soluble supercapacitors: large and reversible charge storage in colloidal iron-doped ZnO nanocrystals. *Nano Lett.* **2018,** *18* (5), 3297-3302.

(11) Schimpf, A. M.; Lounis, S. D.; Runnerstrom, E. L.; Milliron, D. J.; Gamelin, D. R. Redox chemistries and plasmon energies of photodoped $In_2O_3$ and Sn-doped $In_2O_3$ (ITO) nanocrystals. *J. Am. Chem. Soc.* **2015,** *137* (1), 518-524.

(12) Wang, C.; Shim, M.; Guyot-Sionnest, P. Electrochromic nanocrystal quantum dots. *Science* **2001,** *291* (5512), 2390-2392.

(13) Joost, U.; Šutka, A.; Oja, M.; Smits, K.; Döbelin, N.; Loot, A.; Järvekülg, M.; Hirsimäki, M.; Valden, M.; Nõmmiste, E. Reversible photodoping of $TiO_2$ nanoparticles for photochromic applications. *Chem. Mater.* **2018,** *30* (24), 8968-8974.

(14) Liu, W. K.; Whitaker, K. M.; Kittilstved, K. R.; Gamelin, D. R. Stable photogenerated carriers in magnetic semiconductor nanocrystals. *J. Am. Chem. Soc.* **2006,** *128* (12), 3910-3911.

(15) Schimpf, A. M.; Gunthardt, C. E.; Rinehart, J. D.; Mayer, J. M.; Gamelin, D. R. Controlling carrier densities in photochemically reduced colloidal ZnO nanocrystals: size dependence and role of the hole quencher. *J. Am. Chem. Soc.* **2013,** *135* (44), 16569-16577.

(16) Harrigan, W. L.; Michaud, S. E.; Lehuta, K. A.; Kittilstved, K. R. Tunable electronic structure and surface defects in chromium-doped colloidal $SrTiO_{3-\delta}$ nanocrystals. *Chem. Mater.* **2016,** *28* (2), 430-433.

(17) Abdullah, M.; Kittilstved, K. R.; Nelson, R. J. Tunable redox activity at $Fe^{3+}$ centers in colloidal $ATiO_3$ (A = Sr and Ba) nanocrystals. *Chem. Mater.* **2021**.

(18) Schrauben, J. N.; Hayoun, R.; Valdez, C. N.; Braten, M.; Fridley, L.; Mayer, J. M. Titanium and zinc oxide nanoparticles are proton-coupled electron transfer agents. *Science* **2012,** *336* (6086), 1298-1301.

(19) De Trizio, L.; Buonsanti, R.; Schimpf, A. M.; Llordes, A.; Gamelin, D. R.; Simonutti, R.; Milliron, D. J. Nb-doped colloidal $TiO_2$ nanocrystals with tunable infrared absorption. *Chem. Mater.* **2013,** *25* (16), 3383-3390.

(20) Cao, S.; Zhang, S.; Zhang, T.; Fisher, A.; Lee, J. Y. Metal-doped $TiO_2$ colloidal nanocrystals with broadly tunable plasmon resonance absorption. *J. Mater. Chem. C* **2018,** *6* (15), 4007-4014.

(21) Denisov, N.; Yoo, J.; Schmuki, P. Effect of different hole scavengers on the photoelectrochemical properties and photocatalytic hydrogen evolution performance of pristine and Pt-decorated $TiO_2$ nanotubes. *Electrochim. Acta* **2019,** *319*, 61-71.

(22) Berto, T. F.; Sanwald, K. E.; Eisenreich, W.; Gutiérrez, O. Y.; Lercher, J. A. Photoreforming of ethylene glycol over Rh/$TiO_2$ and Rh/GaN:ZnO. *J. Catal.* **2016,** *338*, 68-81.

(23) Zhou, D.; Kittilstved, K. R. Electron trapping on $Fe^{3+}$ sites in photodoped ZnO colloidal nanocrystals. *Chem. Commun.* **2016,** *52* (58), 9101-9104.

(24) Harrigan, W. L.; Michaud, S. E.; Lehuta, K. A.; Kittilstved, K. R. Tunable electronic structure and surface defects in chromium-doped colloidal $SrTiO_{3-\delta}$ nanocrystals. *Chem. Mater.* **2016,** *28* (2), 430-433.

# CHAPTER

# CONCLUSION AND FUTURE DIRECTIONS

This thesis explores the defect chemistry and dopant-carrier interactions in aliovalent-doped colloidal $SrTiO_3$, $BaTiO_3$ and $TiO_2$ NCs. In chapter 2, we have presented a systemic study to control the surface defect formation during the hydrothermal synthesis of colloidal $SrTiO_3$ and $BaTiO_3$ NCs. We found that an electron transfer step presumably from lactate anions to dissolved $O_2$ is the critical step that leads to the formation of the surface-adsorbed $O_2^{\bullet-}$ ions. These surface $O_2^{\bullet-}$ defects are EPR active and impart a broad feature throughout the visible region that produces a reddish-brown color to the NCs. We also provided evidence that the removal of dissolved $O_2$ by either addition of hydrazine, purging with argon or using lactate-free Ti(IV) precursors inhibit $O_2^{\bullet-}$ formation. These results shed light on the role of additives in the chemical synthesis of colloidal $ATiO_3$ NCs. A potential direction for this work could be exploring the existence of such defect formation and their control in other oxide NCs. We also speculate that these reactive defects can play an integral role in surface-based chemistry such as photocatalysis and there is significant work that can be done to make use of these $O_2^{\bullet-}$ radicals for various applications. In addition, the brown color that these defects impart to the $SrTiO_3$ NCs can undoubtedly enhance the optical absorbance for visible light photocatalysis.

Chapter 3 discussed the synthesis and characterization of Fe-doped $SrTiO_3$ and $BaTiO_3$ colloidal NCs and investigated their dopant-defect interaction using various spectroscopies. The results presented here provide convincing evidence that the valance state of Fe dopant can be modulated between 3+ and 2+ by post-synthetic

manipulation of carrier densities in these NCs. The introduction of excess charge carriers at room temperature using photodoping methods into $Fe^{3+}$:$SrTiO_3$ and $Fe^{3+}$:$BaTiO_3$ colloidal NCs results in the reduction of $Fe^{3+}$ to $Fe^{2+}$. Both the dopant and lattice electron storage capacity makes these colloidal NCs potentially suitable for non-aqueous redox flow batteries and charge storage applications. Direct verification of $Fe^{2+}$ is challenging due to the air-sensitive nature of the photodoped NCs. Therefore, the alternative methods to achieve air-stable n-type defects in related $d^0$ colloidal semiconductor NCs are discussed in chapter 4. In addition, we have seen a significant difference in the microenvironment of $Ti^{3+}$ defects between $SrTiO_3$ and $BaTiO_3$ NCs. More sophisticated spectroscopic methods would be required to probe the speciation (surfaces, sub-surfaces and/or cores) of added electrons in these colloidal NCs.

Chapter 4 presented the synthesis and characterization of $Fe^{3+}$-doped $TiO_2$ colloidal NCs using a solvothermal method and reversible control of dopant valence state under ambient conditions. The spectroscopic analysis of as-prepared NCs shows that $Fe^{3+}$ is substituted at the $Ti^{4+}$ site, and there is no evidence of any surface dopants. The introduction of excess electrons using the photodoping method can reversibly manipulate the oxidation state of the dopant between $Fe^{3+}$ and $Fe^{2+}$. We further presented an alternative approach to control the oxidation of $Fe^{3+}$ dopant by incorporating the aliovalent $Nb^{5+}$ as a co-dopant. The substitution of $Nb^{5+}$ at $Ti^{4+}$ adds air-stable excess electrons, majority of which are identified as free carriers in the conduction band. This method reduces the $Fe^{3+}$ dopants to $Fe^{2+}$, offering control over dopant oxidation under ambient conditions. This latter method opens the avenue to

directly observe the $Fe^{2+}$ dopants and their possible spin interactions with $Fe^{3+}$ and $Ti^{3+}$ defects. There is also a possibility of variable $Nb^{5+}$ doping concentration to achieve the mixed-valence states of $Fe^{3+}$ and the other redox-active dopants in oxide lattices.

Chapter 5 is motivated by previous work on Cr-doped $SrTiO_3$ NCs, where the effect of excess carriers on substitutional $Cr^{3+}$ dopants in additional Ti-based oxide NCs is discussed. We prepared and characterized the Cr-doped colloidal $BaTiO_3$ and $TiO_2$ NCs. The synthetic methods employed in this work allowed the incorporation of $Cr^{3+}$ dopants at substitutional $Ti^{4+}$ sites. The introduction of excess electrons using photodoping methods shows the disappearance of the $Cr^{3+}$-related EPR signal in both the $BaTiO_3$ and $TiO_2$ NCs. We attribute this signal disappearance to changes in spin relaxation times ($T_1$ and $T_2$) of $Cr^{3+}$ dopants. This work expands on the interactions we previously found with Cr-doped $SrTiO_3$ NCs and opens the avenue of near-resonant cross-relaxation as a new tool to control the spin properties of paramagnetic centers. Direct measurements of $Cr^{3+}$ relaxation times, its dependence on the concentration of $Ti^{3+}$ defects, and NCs size and surface chemistry are some of the future directions for this project.

In the last chapter of this thesis, a method to estimate the carrier concentration in photodoped colloidal $SrTiO_3$ NCs is discussed. We explored the kinetics and various competing processes for electron addition during photodoping. The controlled photodoping experiments show the rate of electron addition is significantly faster at the earlier stages of photodoping time, which can be further enhanced by employing a better sacrificial reductant. In the latter part of this work, we combined x-ray

diffraction and ICP-OES analysis to determine the concentration of NCs that led to streamlining the chemical titration of photodoped NCs. The chemical titration of photodoped NCs against one-electron oxidant TEMPO was performed to estimate the maximum number of electrons stored per NC of $SrTiO_3$, which is significantly higher than the previously reported number for $TiO_2$ and ZnO NCs. This work can lead to using these NCs as solution-based charge storage. There is also a great potential to expand this work on doped $SrTiO_3$ NCs to tune the kinetics of electron addition and NCs carrier storage capacity. Effect of NCs size, surface chemistry and morphology are some of the challenges to navigate this project in the future.

# BIBLIOGRAPHY


Abdullah, M.; Kittilstved, K. R.; Nelson, R. J. Tunable redox activity at $Fe^{3+}$ centers in colloidal $ATiO_3$ (A = Sr and Ba) nanocrystals. *Chem. Mater.* **2021**.

Abdullah, M.; Nelson, R. J.; Kittilstved, K. R. On the formation of superoxide radicals on colloidal $ATiO_3$ (A= Sr and Ba) nanocrystal surfaces. *Nanoscale Adv.* **2020,** *2*, 1949-1955.

Açıkgöz, M.; Gnutek, P.; Rudowicz, C. Modeling zero-field splitting parameters for dopant $Mn^{2+}$ and $Fe^{3+}$ ions in anatase $TiO_2$ crystal using superposition model analysis. *Chem. Phys. Lett.* **2012,** *524*, 49-55.

Adireddy, S.; Lin, C.; Cao, B.; Zhou, W.; Caruntu, G. Solution-Based Growth of Monodisperse Cube-Like $BaTiO_3$ Colloidal Nanocrystals. *Chem. Mater.* **2010,** *22* (6), 1946-1948.

Ali, T.; Tripathi, P.; Azam, A.; Raza, W.; Ahmed, A. S.; Ahmed, A.; Muneer, M. Photocatalytic performance of Fe-doped $TiO_2$ nanoparticles under visible-light irradiation. *Mater. Res. Express* **2017,** *4* (1), 015022.

Attwood, A. L.; Murphy, D. M.; Edwards, J. L.; Egerton, T. A.; Harrison, R. W. An EPR study of thermally and photochemically generated oxygen radicals on hydrated and dehydrated titania surfaces. *Res. Chem. Intermed.* **2003,** *29* (5), 449-465.

Azzoni, C.; Mozzati, M.; Paleari, A.; Massarotti, V.; Bini, M.; Capsoni, D. Magnetic evidence of different environments of manganese ions in Mn-substituted strontium titanate. *Solid State Commun.* **2000,** *114* (12), 617-622.

Bader, S.; Parkin, S. Spintronics. *Annu. Rev. Condens. Matter Phys.* **2010,** *1* (1), 71-88.

Baeumer, C.; Schmitz, C.; Ramadan, A. H.; Du, H.; Skaja, K.; Feyer, V.; Muller, P.; Arndt, B.; Jia, C. L.; Mayer, J.; De Souza, R. A.; Michael Schneider, C.; Waser, R.; Dittmann, R. Spectromicroscopic insights for rational design of redox-based memristive devices. *Nat. Commun.* **2015,** *6*, 8610.

Beier, C. W.; Cuevas, M. A.; Brutchey, R. L. Low-temperature synthesis of solid-solution $Ba_xSr_{1-x}TiO_3$ nanocrystals. *J. Mater. Chem.* **2010,** *20* (24), 5074-5079.

Benouis, C.; Benhaliliba, M.; Mouffak, Z.; Avila-Garcia, A.; Tiburcio-Silver, A.; Lopez, M. O.; Trujillo, R. R.; Ocak, Y. The low resistive and transparent Al-doped $SnO_2$ films: p-type conductivity, nanostructures and photoluminescence. *J. Alloys Compd.* **2014,** *603*, 213-223.

Berglund, C.; Braun, H. Optical absorption in single-domain ferroelectric barium titanate. *Phys. Rev.* **1967,** *164* (2), 790.

Berney, R.; Cowan, D. Photochromism of three photosensitive Fe centers in $SrTiO_3$. *Phys. Rev. B* **1981,** *23* (1), 37-50.

Bersuker, I. B.; Polinger, V. Perovskite Crystals: Unique Pseudo-Jahn–Teller Origin of Ferroelectricity, Multiferroicity, Permittivity, Flexoelectricity, and Polar Nanoregions. *Condens. Matter* **2020,** *5* (4), 68.

Berto, T. F.; Sanwald, K. E.; Eisenreich, W.; Gutiérrez, O. Y.; Lercher, J. A. Photoreforming of ethylene glycol over $Rh/TiO_2$ and Rh/GaN:ZnO. *J. Catal.* **2016,** *338*, 68-81.

Bertolino, S. M.; Melgaco, L. A.; Sa, R. G.; Leao, V. A. Comparing lactate and glycerol as a single-electron donor for sulfate reduction in fluidized bed reactors. *Biodegradation* **2014,** *25* (5), 719-733.

Bowen, E. J.; Birley, A. W. The vapour phase reaction between hydrazine and oxygen. *Trans. Faraday Soc.* **1951,** *47*, 580-583.

Brozek, C. K.; Zhou, D.; Liu, H.; Li, X.; Kittilstved, K. R.; Gamelin, D. R. Soluble supercapacitors: large and reversible charge storage in colloidal iron-doped ZnO nanocrystals. *Nano Lett.* **2018,** *18* (5), 3297-3302.

Brozek, C. K.; Zhou, D.; Liu, H.; Li, X.; Kittilstved, K. R.; Gamelin, D. R. Soluble supercapacitors: large and reversible charge storage in colloidal iron-doped ZnO nanocrystals. *Nano Lett.* **2018,** *18* (5), 3297-3302.

Buscaglia, M.; Buscaglia, V.; Viviani, M.; Nanni, P.; Hanuskova, M. Influence of foreign ions on the crystal structure of BaTiO3. *J. Eur. Ceram. Soc.* **2000,** *20* (12), 1997-2007.

Buz, E.; Zhou, D. M.; Kittilstved, K. R. Air-stable n-type Fe-doped ZnO colloidal nanocrystals. *J. Chem. Phys.* **2019,** *151* (13), 134702.

Canu, G.; Buscaglia, V. Hydrothermal synthesis of strontium titanate: thermodynamic considerations, morphology control and crystallisation mechanisms. *CrystEngComm* **2017,** *19* (28), 3867-3891.

Cao, S.; Zhang, S.; Zhang, T.; Fisher, A.; Lee, J. Y. Metal-doped $TiO_2$ colloidal nanocrystals with broadly tunable plasmon resonance absorption. *J. Mater. Chem. C* **2018,** *6* (15), 4007-4014.

Cao, S.; Zhang, S.; Zhang, T.; Fisher, A.; Lee, J. Y. Metal-doped $TiO_2$ colloidal nanocrystals with broadly tunable plasmon resonance absorption. *J. Mater. Chem. C* **2018,** *6* (15), 4007-4014.

Cao, Y. C. Impurities enhance semiconductor nanocrystal performance. *Science* **2011,** *332* (6025), 48-49.

Carneiro, J.; Azevedo, S.; Fernandes, F.; Freitas, E.; Pereira, M.; Tavares, C.; Lanceros-Méndez, S.; Teixeira, V. Synthesis of iron-doped $TiO_2$ nanoparticles by ball-milling process: the influence of process parameters on the structural, optical, magnetic, and photocatalytic properties. *J. Mater. Sci.* **2014,** *49* (21), 7476-7488.

Carroll, G. M.; Schimpf, A. M.; Tsui, E. Y.; Gamelin, D. R. Redox potentials of colloidal n-type ZnO nanocrystals: effects of confinement, electron density, and fermi-Level pinning by aldehyde hydrogenation. *J. Am. Chem. Soc.* **2015,** *137* (34), 11163-11169.

Carter, E.; Carley, A. F.; Murphy, D. M. Evidence for $O_2^-$ radical stabilization at surface oxygen vacancies on polycrystalline $TiO_2$. *J. Phys. Chem. C* **2007,** *111* (28), 10630-10638.

Chandra, P. Multifunctionality goes quantum critical. *Nat. Mater.* **2019,** *18* (3), 197.

Cheng, G.; Liu, X.; Song, X.; Chen, X.; Dai, W.; Yuan, R.; Fu, X. Visible-light-driven deep oxidation of NO over Fe doped $TiO_2$ catalyst: Synergic effect of Fe and oxygen vacancies. *Appl. Catal., B* **2020,** *277*, 119196.

Choudhury, D.; Mukherjee, S.; Mandal, P.; Sundaresan, A.; Waghmare, U.; Bhattacharjee, S.; Mathieu, R.; Lazor, P.; Eriksson, O.; Sanyal, B. Tuning of dielectric properties and magnetism of $SrTiO_3$ by site-specific doping of Mn. *Phys. Rev. B* **2011,** *84* (12), 125124.

Choudhury, D.; Pal, B.; Sharma, A.; Bhat, S.; Sarma, D. D. Magnetization in electron-and Mn-doped $SrTiO_3$. *Sci. Rep.* **2013,** *3* (1), 1-4.

Comes, R. B.; Kaspar, T. C.; Heald, S. M.; Bowden, M. E.; Chambers, S. A. Infrared optical absorption in low-spin $Fe^{2+}$-doped $SrTiO_3$. *J. Phys. Cond. Matter* **2016,** *28* (3), 035901.

Costanzo, T.; McCracken, J.; Rotaru, A.; Caruntu, G. Quasi-monodisperse transition-metal-doped $BaTiO_3$ (M = Cr, Mn, Fe, Co) colloidal nanocrystals with multiferroic properties. *ACS Appl. Nano Mater.* **2018,** *1* (9), 4863-4874.

Dahlman, C. J.; Agrawal, A.; Staller, C. M.; Adair, J.; Milliron, D. J. Anisotropic Origins of Localized Surface Plasmon Resonance in n-Type Anatase $TiO_2$ Nanocrystals. *Chem. Mater.* **2019,** *31* (2), 502-511.

Dang, F.; Mimura, K.-I.; Kato, K.; Imai, H.; Wada, S.; Haneda, H.; Kuwabara, M. Growth of monodispersed $SrTiO_3$ nanocubes by thermohydrolysis method. *CrystEngComm* **2011,** *13* (11), 3878-3883.

De Trizio, L.; Buonsanti, R.; Schimpf, A. M.; Llordes, A.; Gamelin, D. R.; Simonutti, R.; Milliron, D. J. Nb-doped colloidal $TiO_2$ nanocrystals with tunable infrared absorption. *Chem. Mater.* **2013,** *25* (16), 3383-3390.

De Trizio, L.; Buonsanti, R.; Schimpf, A. M.; Llordes, A.; Gamelin, D. R.; Simonutti, R.; Milliron, D. J. Nb-doped colloidal $TiO_2$ nanocrystals with tunable infrared absorption. *Chem. Mater.* **2013,** *25* (16), 3383-3390.

Denisov, N.; Yoo, J.; Schmuki, P. Effect of different hole scavengers on the photoelectrochemical properties and photocatalytic hydrogen evolution performance of pristine and Pt-decorated $TiO_2$ nanotubes. *Electrochim. Acta* **2019,** *319*, 61-71.

Di Valentin, C.; Pacchioni, G.; Selloni, A. Reduced and n-type doped $TiO_2$: nature of $Ti^{3+}$ species. *J. Phys. Chem. C* **2009,** *113* (48), 20543-20552.

Dietl, T. A ten-year perspective on dilute magnetic semiconductors and oxides. *Nat. Mater.* **2010,** *9* (12), 965-974.

Dinh, C.-T.; Nguyen, T.-D.; Kleitz, F.; Do, T.-O. Shape-controlled synthesis of highly crystalline titania nanocrystals. *ACS Nano* **2009,** *3* (11), 3737-3743.

Dionne, G. F. Spin-Lattice relaxation of $Ti^{3+}$ ions in $RbAl(SO_4)_2{\cdot}12H_2O$. *Phys. Rev.* **1965,** *139* (5A), A1648.

Drahus, M. D.; Jakes, P.; Erdem, E.; Eichel, R.-A. Defect structure of the mixed ionic electronic conducting $Sr[Ti,Fe]O_x$ solid solution system-change in iron oxidation states and defect complexation. *Solid State Ionics* **2011,** *184* (1), 47-51.

Durán, A.; Martínez, E.; Díaz, J.; Siqueiros, J. Ferroelectricity at room temperature in Pr-doped $SrTiO_3$. *J. Appl. Phys.* **2005,** *97* (10), 104109.

Eden, S.; Kapphan, S.; Hesse, H.; Trepakov, V.; Vikhnin, V.; Gregora, I.; Jastrabik, L.; Seglins, J. Observations of the absorption, infra-red emission, and excitation spectra of Cr in $BaTiO_3$. *J. Phys.: Condens. Matter* **1998,** *10* (47), 10775.

Eden, S.; Kapphan, S.; Hesse, H.; Trepakov, V.; Vikhnin, V.; Jastrabik, L.; Gregora, I. Near infra-red luminescence of $BaTiO_3$:Cr. *Radiat. Eff. Defects Solids* **1999,** *149* (1-4), 107-112.

Eror, N.; Balachandran, U. High-temperature defect structure of acceptor-doped strontium titanate. *J. Am. Ceram. Soc.* **1982,** *65* (9), 426-431.

Farvid, S. S.; Sabergharesou, T.; Hutfluss, L. N.; Hegde, M.; Prouzet, E.; Radovanovic, P. V. Evidence of charge-transfer ferromagnetism in transparent diluted magnetic oxide nanocrystals: switching the mechanism of magnetic interactions. *J. Am. Chem. Soc.* **2014,** *136* (21), 7669-7679.

Faughnan, B.; Kiss, Z. Optical and EPR studies of photochromic $SrTiO_3$ doped with Fe/Mo and Ni/Mo. *IEEE J. Quantum Electron.* **1969,** *5* (1), 17-21.

Fix, T.; Liberati, M.; Aubriet, H.; Sahonta, S.; Bali, R.; Becker, C.; Ruch, D.; MacManus-Driscoll, J.; Arenholz, E.; Blamire, M. Ferromagnetism in Co-doped (La,Sr)$TiO_3$. *New J. Phys.* **2009,** *11* (7), 073042.

Fujinami, K.; Katagiri, K.; Kamiya, J.; Hamanaka, T.; Koumoto, K. Sub-10 nm strontium titanate nanocubes highly dispersed in non-polar organic solvents. *Nanoscale* **2010,** *2* (10), 2080-2083.

Garnet, N. S.; Ghodsi, V.; Hutfluss, L. N.; Yin, P.; Hegde, M.; Radovanovic, P. V. Probing the role of dopant oxidation state in the magnetism of diluted magnetic oxides using Fe-doped $In_2O_3$ and $SnO_2$ nanocrystals. *J. Phys. Chem. C* **2017,** *121* (3), 1918-1927.

Giguère, P. A.; Liu, I. D. On the infrared spectrum of hydrazine. *J. Chem. Phys.* **1952,** *20* (1), 136-140.

Glais, E.; Massuyeau, F.; Gautier, R. Tuning the oxidation states of dopants: a strategy for the modulation of material photoluminescence properties. *Chem. Eur. J.* **2020**.

Green, J.; Carter, E.; Murphy, D. M. Interaction of molecular oxygen with oxygen vacancies on reduced $TiO_2$: Site specific blocking by probe molecules. *Chem. Phys. Lett.* **2009,** *477* (4-6), 340-344.

Gui, Z.; Janotti, A. Carrier-density-induced ferromagnetism in $EuTiO_3$ bulk and heterostructures. *Phys. Rev. Lett.* **2019,** *123* (12), 127201.

Guo, D.; Xu, S.; Wang, C.; Wang, Z.; Yin, H.; Deng, H.; Jiang, Y.; Zhang, Z.; Zhang, X.; Shao, H. Doping of $Mn^{2+}$ into aqueous ZnSe nanocrystals with pure dopant emission through a light-induced electrostatic attraction and diffusion method. *J. Phys. Chem. C* **2021,** *125* (1), 989-997.

Han, W.; Kawakami, R. K.; Gmitra, M.; Fabian, J. Graphene spintronics. *Nat. Nanotech.* **2014,** *9* (10), 794-807.

Harrigan, W. L.; Kittilstved, K. R. Reversible modulation of the $Cr^{3+}$ spin dynamics in colloidal $SrTiO_3$ nanocrystals. *J. Phys. Chem. C* **2018,** *122* (46), 26652-26657.

Harrigan, W. L.; Kittilstved, K. R. Reversible modulation of the $Cr^{3+}$ spin dynamics in colloidal $SrTiO_3$ nanocrystals. *J. Phys. Chem. C* **2018,** *122* (46), 26652-26657.

Harrigan, W. L.; Michaud, S. E.; Lehuta, K. A.; Kittilstved, K. R. Tunable electronic structure and surface defects in chromium-doped colloidal $SrTiO_{3-\delta}$ nanocrystals. *Chem. Mater.* **2016,** *28* (2), 430-433.

Harrigan, W. L.; Michaud, S. E.; Lehuta, K. A.; Kittilstved, K. R. Tunable electronic structure and surface defects in chromium-doped colloidal $SrTiO_{3-\delta}$ nanocrystals. *Chem. Mater.* **2016,** *28* (2), 430-433.

Hayyan, M.; Hashim, M. A.; AlNashef, I. M. Superoxide ion: Generation and chemical implications. *Chem. Rev.* **2016,** *116* (5), 3029-3085.

Henglein, A. Colloidal $TiO_2$ catalyzed photo- and radiation chemical processes in aqueous solution. *Ber. Bunsenges. Phys. Chem.* **1982,** *86* (3), 241-246.

Ichihara, F.; Sieland, F.; Pang, H.; Philo, D.; Duong, A.-T.; Chang, K.; Kako, T.; Bahnemann, D. W.; Ye, J. Photogenerated charge carriers dynamics on La- and/or Cr-doped $SrTiO_3$ nanoparticles studied by transient absorption spectroscopy. *J. Phys. Chem. C* **2020,** *124* (2), 1292-1302.

Inaba, J.; Katsufuji, T. Large magnetoresistance in spin-and carrier-doped $SrTiO_3$. *Phys. Rev. B* **2005,** *72* (5), 052408.

Ishii, T.; Kato, H.; Kudo, A. $H_2$ evolution from an aqueous methanol solution on $SrTiO_3$ photocatalysts codoped with chromium and tantalum ions under visible light irradiation. *J. Photochem. Photobiol. A* **2004,** *163* (1-2), 181-186.

Jiao, Z.; Chen, T.; Xiong, J.; Wang, T.; Lu, G.; Ye, J.; Bi, Y. Visible-light-driven photoelectrochemical and photocatalytic performances of Cr-doped $SrTiO_3/TiO_2$ heterostructured nanotube arrays. *Sci. Rep.* **2013,** *3* (1), 1-6.

Joost, U.; Šutka, A.; Oja, M.; Smits, K.; Döbelin, N.; Loot, A.; Järvekülg, M.; Hirsimäki, M.; Valden, M.; Nõmmiste, E. Reversible photodoping of $TiO_2$ nanoparticles for photochromic applications. *Chem. Mater.* **2018,** *30* (24), 8968-8974.

Joost, U.; Šutka, A.; Oja, M.; Smits, K.; Döbelin, N.; Loot, A.; Järvekülg, M.; Hirsimäki, M.; Valden, M.; Nõmmiste, E. Reversible photodoping of $TiO_2$ nanoparticles for photochromic applications. *Chem. Mater.* **2018,** *30* (24), 8968-8974.

Ju, L.; Sabergharesou, T.; Stamplecoskie, K. G.; Hegde, M.; Wang, T.; Combe, N. A.; Wu, H.; Radovanovic, P. V. Interplay between size, composition, and phase transition of nanocrystalline $Cr^{3+}$-doped $BaTiO_3$ as a path to multiferroism in perovskite-type oxides. *J. Am. Chem. Soc.* **2012,** *134* (2), 1136-1146.

Kan, D.; Terashima, T.; Kanda, R.; Masuno, A.; Tanaka, K.; Chu, S.; Kan, H.; Ishizumi, A.; Kanemitsu, Y.; Shimakawa, Y.; Takano, M. Blue-light emission at room temperature from $Ar^+$-irradiated $SrTiO_3$. *Nat. Mater.* **2005,** *4* (11), 816-819.

Kan, D. S.; Terashima, T.; Kanda, R.; Masuno, A.; Tanaka, K.; Chu, S. C.; Kan, H.; Ishizumi, A.; Kanemitsu, Y.; Shimakawa, Y.; Takano, M. Blue-light emission at room temperature from $Ar^+$-irradiated $SrTiO_3$. *Nat. Mater.* **2005,** *4* (11), 816-819.

Karmakar, D.; Mandal, S.; Kadam, R.; Paulose, P.; Rajarajan, A.; Nath, T. K.; Das, A. K.; Dasgupta, I.; Das, G. Ferromagnetism in Fe-doped ZnO nanocrystals: experiment and theory. *Phys. Rev. B* **2007,** *75* (14), 144404.

Kaspar, T. C.; Droubay, T.; Shutthanandan, V.; Heald, S. M.; Wang, C. M.; McCready, D. E.; Thevuthasan, S.; Bryan, J.; Gamelin, D. R.; Kellock, A. Ferromagnetism and structure of epitaxial Cr-doped anatase $TiO_2$ thin films. *Phys. Rev. B* **2006,** *73* (15), 155327.

Kato, H.; Kudo, A. Visible-light-response and photocatalytic activities of $TiO_2$ and $SrTiO_3$ photocatalysts codoped with antimony and chromium. *J. Phys. Chem. B* **2002,** *106* (19), 5029-5034.

Kato, H.; Kudo, A. Visible-light-response and photocatalytic activities of $TiO_2$ and $SrTiO_3$ photocatalysts codoped with antimony and chromium. *J. Phys. Chem. B* **2002,** *106* (19), 5029-5034.

Kato, H.; Sasaki, Y.; Shirakura, N.; Kudo, A. Synthesis of highly active rhodium-doped $SrTiO_3$ powders in Z-scheme systems for visible-light-driven photocatalytic overall water splitting. *J. Mater. Chem. A* **2013,** *1* (39), 12327.

Kawasaki, S.; Nakatsuji, K.; Yoshinobu, J.; Komori, F.; Takahashi, R.; Lippmaa, M.; Mase, K.; Kudo, A. Epitaxial Rh-doped $SrTiO_3$ thin film photocathode for water splitting under visible light irradiation. *Appl. Phys. Lett.* **2012,** *101* (3), 033910.

Kim, H.-S.; Bi, L.; Dionne, G.; Ross, C. Magnetic and magneto-optical properties of Fe-doped $SrTiO_3$ films. *Appl. Phys. Lett.* **2008,** *93* (9), 092506.

Koehl, A.; Kajewski, D.; Kubacki, J.; Lenser, C.; Dittmann, R.; Meuffels, P.; Szot, K.; Waser, R.; Szade, J. Detection of $Fe^{2+}$ valence states in Fe doped $SrTiO_3$ epitaxial thin films grown by pulsed laser deposition. *Phys. Chem. Chem. Phys.* **2013,** *15* (21), 8311-8317.

Komaguchi, K.; Maruoka, T.; Nakano, H.; Imae, I.; Ooyama, Y.; Harima, Y. Electron-transfer reaction of oxygen species on $TiO_2$ nanoparticles induced by sub-band-gap illumination. *J. Phys. Chem. C* **2010,** *114* (2), 1240-1245.

Komaguchi, K.; Maruoka, T.; Nakano, H.; Imae, I.; Ooyama, Y.; Harima, Y. ESR study on the reversible electron transfer from $O_2^{2-}$ to $Ti^{4+}$ on $TiO_2$ nanoparticles induced by visible-light illumination. *J. Phys. Chem. C* **2009,** *113* (4), 1160-1163.

Kubacki, J.; Kajewski, D.; Koehl, A.; Lenser, C.; Dittmann, R.; Szade, J. X‐ray absorption and resonant photoemission studies of electroforming process in Fe‐doped $SrTiO_3$ epitaxial films. *X-Ray Spectrometry* **2015,** *44* (5), 339-343.

Kumar, A. S.; Suresh, P.; Kumar, M. M.; Srikanth, H.; Post, M.; Sahner, K.; Moos, R.; Srinath, S. In *Magnetic and ferroelectric properties of Fe doped $SrTiO_{3-\delta}$ films*, J. Phys.: Conf. Ser., 2010; p 092010.

Kuo, Y.; Klabunde, K. J. Hydrogen generation from water/methanol under visible light using aerogel prepared strontium titanate ($SrTiO_3$) nanomaterials doped with ruthenium and rhodium metals. *Nanotechnology* **2012,** *23* (29), 294001.

Kwei, G.; Lawson, A.; Billinge, S.; Cheong, S.-W. Structures of the ferroelectric phases of barium titanate. *J. Phys. Chem.* **1993,** *97* (10), 2368-2377.

Łącz, A.; Drożdż, E. Porous Y and Cr–doped $SrTiO_3$ materials—electrical and redox properties. *J. Solid State Electrochem.* **2019,** *23* (10), 2989-2997.

Lehuta, K. A.; Kittilstved, K. R. Reversible control of the chromium valence in chemically reduced Cr-doped $SrTiO_3$ bulk powders. *Dalton Trans.* **2016,** *45* (24), 10034-10041.

Lehuta, K. A.; Kittilstved, K. R. Reversible control of the chromium valence in chemically reduced Cr-doped $SrTiO_3$ bulk powders. *Dalton Trans.* **2016,** *45* (24), 10034-10041.

Lehuta, K. A.; Kittilstved, K. R. Speciation of Cr(iii) in intermediate phases during the sol–gel processing of Cr-doped $SrTiO_3$ powders. *J. Mater. Chem. A* **2014,** *2* (17), 6138-6145.

Lenser, C.; Kalinko, A.; Kuzmin, A.; Berzins, D.; Purans, J.; Szot, K.; Waser, R.; Dittmann, R. Spectroscopic study of the electric field induced valence change of Fe-defect centers in $SrTiO_3$. *Phys. Chem. Chem. Phys.* **2011,** *13* (46), 20779-20786.

Leonelli, R.; Brebner, J. Time-resolved spectroscopy of the visible emission band in strontium titanate. *Phys. Rev. B* **1986,** *33* (12), 8649-8656.

Li, H.; Yin, S.; Wang, Y.; Sekino, T.; Lee, S. W.; Sato, T. Roles of $Cr^{3+}$ doping and oxygen vacancies in $SrTiO_3$ photocatalysts with high visible light activity for NO removal. *J. Catal.* **2013,** *297*, 65-69.

Li, Y.; Zhang, W.; Niu, J.; Chen, Y. Mechanism of photogenerated reactive oxygen species and correlation with the antibacterial properties of engineered metal-oxide nanoparticles. *ACS Nano* **2012,** *6* (6), 5164-5173.

Liu, M.; Piao, L.; Zhao, L.; Ju, S.; Yan, Z.; He, T.; Zhou, C.; Wang, W. Anatase $TiO_2$ single crystals with exposed {001} and {110} facets: facile synthesis and enhanced photocatalysis. *Chem. Commun.* **2010,** *46* (10), 1664-1666.

Liu, W. K.; Whitaker, K. M.; Kittilstved, K. R.; Gamelin, D. R. Stable photogenerated carriers in magnetic semiconductor nanocrystals. *J. Am. Chem. Soc.* **2006,** *128* (12), 3910-3911.

Liu, W. K.; Whitaker, K. M.; Kittilstved, K. R.; Gamelin, D. R. Stable photogenerated carriers in magnetic semiconductor nanocrystals. *J. Am. Chem. Soc.* **2006,** *128* (12), 3910-3911.

Luther, J. M.; Jain, P. K.; Ewers, T.; Alivisatos, A. P. Localized surface plasmon resonances arising from free carriers in doped quantum dots. *Nat. Mater.* **2011,** *10* (5), 361-366.

Luther, J. M.; Jain, P. K.; Ewers, T.; Alivisatos, A. P. Localized surface plasmon resonances arising from free carriers in doped quantum dots. *Nat. Mater.* **2011,** *10* (5), 361-366.

Ma, D.; Liu, A.; Li, S.; Lu, C.; Chen, C. $TiO_2$ photocatalysis for C–C bond formation. *Catal. Sci. Technol.* **2018,** *8* (8), 2030-2045.

Ma, Q.; Kato, K. Nucleation and growth mechanism of barium titanate nanoblocks in hydrothermal process using aqueous titanium compound. *Cryst. Growth Des.* **2017,** *17* (5), 2507-2512.

Maier, R. A.; Johnston‐Peck, A. C.; Donohue, M. P. (Magic Dopant) amphoteric behavior of a redox‐active transition metal ion in a perovskite lattice: new insights on the lattice site occupation of manganese in SrTiO3. *Adv. Funct. Mater.* **2016,** *26* (45), 8325-8333.

Mansoor, H.; Harrigan, W. L.; Lehuta, K. A.; Kittilstved, K. R. Reversible control of the Mn oxidation state in $SrTiO_3$ bulk powders. *Front. Chem.* **2019,** *7*, 353.

Mansoor, H.; Harrigan, W. L.; Lehuta, K. A.; Kittilstved, K. R. Reversible Control of the Mn Oxidation State in $SrTiO_3$ Bulk Powders. *Front. Chem.* **2019,** *7*, 353.

Manthiram, K.; Alivisatos, A. P. Tunable localized surface plasmon resonances in tungsten oxide nanocrystals. *J. Am. Chem. Soc.* **2012,** *134* (9), 3995-3998.

Matsumoto, Y.; Murakami, M.; Shono, T.; Hasegawa, T.; Fukumura, T.; Kawasaki, M.; Ahmet, P.; Chikyow, T.; Koshihara, S.-y.; Koinuma, H. Room-temperature ferromagnetism in transparent transition metal-doped titanium dioxide. *Science* **2001,** *291* (5505), 854-856.

Merkle, R.; Maier, J. Defect association in acceptor-doped $SrTiO_3$: case study for $Fe'_{Ti}V_O^{\cdot\cdot}$ and $Mn''_{Ti}V_O^{\cdot\cdot}$. *Phys. Chem. Chem. Phys.* **2003,** *5* (11), 2297-2303.

Mitchell, R.; Chakhmouradian, A.; Woodward, P. Crystal chemistry of perovskite-type compounds in the tausonite-loparite series,$(Sr_{1-2x}Na_xLa_x)TiO_3$. *Phys. Chem. Miner.* **2000,** *27* (8), 583-589.

Mitchell, R.; Chakhmouradian, A.; Woodward, P. Crystal chemistry of perovskite-type compounds in the tausonite-loparite series,$(Sr_{1-2x}Na_x\ La_x)TiO_3$. *Phys. Chem. Miner.* **2000,** *27* (8), 583-589.

Mitchell, R. H.; Chakhmouradian, A. R.; Woodward, P. M. Crystal chemistry of perovskite-type compounds in the tausonite-loparite series, $(Sr_{1-2x}Na_xLa_x)TiO_3$. *Phys. Chem. Minerals* **2000,** *27* (8), 583-589.

Mitra, C.; Lin, C.; Robertson, J.; Demkov, A. A. Electronic structure of oxygen vacancies in $SrTiO_3$ and $LaAlO_3$. *Phys. Rev. B* **2012,** *86* (15), 155105.

Mo, H.; Giersig, M.; Willig, F. Formation of uniform size anatase nanocrystals from bis(ammonium lactato)titanium dihydroxide by thermohydrolysis. *J. Mater. Chem.* **1999,** *9*, 3051-3056.

Mocatta, D.; Cohen, G.; Schattner, J.; Millo, O.; Rabani, E.; Banin, U. Heavily doped semiconductor nanocrystal quantum dots. *Science* **2011,** *332* (6025), 77-81.

Moradi, H.; Eshaghi, A.; Hosseini, S. R.; Ghani, K. Fabrication of Fe-doped $TiO_2$ nanoparticles and investigation of photocatalytic decolorization of reactive red 198 under visible light irradiation. *Ultrason. Sonochem.* **2016,** *32*, 314-319.

Morin, F.; Oliver, J. Energy levels of iron and aluminum in $SrTiO_3$. *Phys. Rev. B* **1973,** *8* (12), 5847-5854.

Muller, K. Paramagnetische Resonanz von $Fe^{3+}$ in $SrTiO_3$-Einkristallen. *Helv. Phys. Acta* **1958,** *31*, 173-204.

Müller, K.; Burkard, H. $SrTiO_3$: An intrinsic quantum paraelectric below 4 K. *Phys. Rev. B* **1979,** *19* (7), 3593-3602.

Mumtaz, S.; Wang, L. S.; Hussain, S. Z.; Abdullah, M.; Huma, Z.; Iqbal, Z.; Creran, B.; Rotello, V. M.; Hussain, I. Dopamine coated $Fe_3O_4$ nanoparticles as enzyme mimics for the sensitive detection of bacteria. *Chem. Commun.* **2017,** *53* (91), 12306-12308.

Naldoni, A.; Altomare, M.; Zoppellaro, G.; Liu, N.; Kment, S. t. p. n.; Zbořil, R.; Schmuki, P. Photocatalysis with reduced $TiO_2$: from black $TiO_2$ to cocatalyst-free hydrogen production. *ACS Catalysis* **2018,** *9* (1), 345-364.

Niishiro, R.; Kato, H.; Kudo, A. Nickel and either tantalum or niobium-codoped $TiO_2$ and $SrTiO_3$ photocatalysts with visible-light response for $H_2$ or $O_2$ evolution from aqueous solutions. *Phys. Chem. Chem. Phys.* **2005,** *7* (10), 2241.

Nisida, Y. Spin-lattice relaxation of $Cr^{3+}$ in coexistence with $Ti^{3+}$ in $Al_2O_3$. *J. Phys. Soc. Japan* **1965,** *20* (8), 1390-1399.

Nogueira, M.; Lustosa, G.; Kobayakawa, Y.; Kogler, W.; Ruiz, M.; Monteiro Filho, E.; Zaghete, M.; Perazolli, L. Nb-doped $TiO_2$ photocatalysts used to reduction of $CO_2$ to methanol. *Adv. Mater. Sci. & Eng.* **2018,** *2018*.

Noland, J. A. Optical absorption of single-crystal strontium titanate. *Phys. Rev.* **1954,** *94* (3), 724-724.

Norberg, N. S.; Kittilstved, K. R.; Amonette, J. E.; Kukkadapu, R. K.; Schwartz, D. A.; Gamelin, D. R. Synthesis of colloidal $Mn^{2+}$: ZnO quantum dots and high-$T_C$ ferromagnetic nanocrystalline thin films. *J. Am. Chem. Soc.* **2004,** *126* (30), 9387-9398.

Norberg, N. S.; Kittilstved, K. R.; Amonette, J. E.; Kukkadapu, R. K.; Schwartz, D. A.; Gamelin, D. R. Synthesis of colloidal $Mn^{2+}$: ZnO quantum dots and high-$T_C$ ferromagnetic nanocrystalline thin films. *J. Am. Chem. Soc.* **2004,** *126* (30), 9387-9398.

O'Brien, S.; Brus, L.; Murray, C. B. Synthesis of monodisperse nanoparticles of barium titanate: toward a generalized strategy of oxide nanoparticle synthesis. *J. Am. Chem. Soc.* **2001,** *123* (48), 12085-12086.

O'Regan, G., Transistor. In *The innovation in computing companion*, Springer: 2018; pp 249-252.

Ochsenbein, S. T.; Feng, Y.; Whitaker, K. M.; Badaeva, E.; Liu, W. K.; Li, X.; Gamelin, D. R. Charge-controlled magnetism in colloidal doped semiconductor nanocrystals. *Nat. Nanotechnol.* **2009,** *4* (10), 681-687.

Ohno, H. A window on the future of spintronics. *Nat. Mater.* **2010,** *9* (12), 952-954.

Ohno, H. A window on the future of spintronics. *Nat. Mater.* **2010,** *9* (12), 952-954.

Osawa, N.; Takahashi, R.; Lippmaa, M. Hole trap state analysis in $SrTiO_3$. *Appl. Phys. Lett.* **2017,** *110* (26), 263902.

Pallavi D, B.; Deu S, B.; Gavisiddappa S, G. Visible light active superoxide modified nanocrystalline anatase titania. *J. Nanoeng. Nanomanuf.* **2015,** *5*, 216-220.

Park, K.; Son, J. S.; Woo, S. I.; Shin, K.; Oh, M.-W.; Park, S.-D.; Hyeon, T. Colloidal synthesis and thermoelectric properties of La-doped $SrTiO_3$ nanoparticles. *J. Mater. Chem. A* **2014,** *2* (12), 4217-4224.

Paul, S.; Bladt, E.; Richter, A. F.; Döblinger, M.; Tong, Y.; Huang, H.; Dey, A.; Bals, S.; Debnath, T.; Polavarapu, L. Manganese‐doping‐induced quantum confinement within host perovskite nanocrystals through Ruddlesden‐Popper defects. *Angew. Chem. Int. Ed.* **2020,** *59* (17), 6794-6799.

Pecchi, G.; Reyes, P.; Lopez, T.; Gomez, R.; Moreno, A.; Fierro, J.; Martínez-Arias, A. Catalytic combustion of methane on Fe-$TiO_2$ catalysts prepared by sol-gel method. *J. Sol-Gel Sci. Technol.* **2003,** *27* (2), 205-214.

Pei, Y.; Zhang, R.; Song, Y.; Bi, J.; Xu, W.; Zhou, C.; Duan, J.; Yang, J.; Cao, Y. Emergent magnetic phase transitions in Fe-doped $SrTiO_{3-\delta}$. *AIP Adv.* **2019,** *9* (12), 125302.

Peper, J. L.; Vinyard, D. J.; Brudvig, G. W.; Mayer, J. M. Slow Equilibration between Spectroscopically Distinct Trap States in Reduced $TiO_2$ Nanoparticles. *J. Am. Chem. Soc.* **2017,** *139* (8), 2868-2871.

Polking, M. J.; Han, M.-G.; Yourdkhani, A.; Petkov, V.; Kisielowski, C. F.; Volkov, V. V.; Zhu, Y.; Caruntu, G.; Alivisatos, A. P.; Ramesh, R. Ferroelectric order in individual nanometre-scale crystals. *Nat. Mater.* **2012,** *11* (8), 700-709.

Queisser, H. J.; Haller, E. E. Defects in semiconductors: some fatal, some vital. *Science* **1998,** *281* (5379), 945-950.

Rabuffetti, F. A.; Brutchey, R. L. Complex perovskite oxide nanocrystals: low-temperature synthesis and crystal structure. *Dalton Trans.* **2014,** *43* (39), 14499-14513.

Rabuffetti, F. A.; Brutchey, R. L. Structural evolution of $BaTiO_3$ nanocrystals synthesized at room temperature. *J. Am. Chem. Soc.* **2012,** *134* (22), 9475-9487.

Rani, N.; Chahal, S.; Kumar, P.; Shukla, R.; Singh, S. Role of oxygen vacancies for mediating ferromagnetic ordering in La-doped MgO nanoparticles. *J. Supercond. Novel Magn.* **2019**, 1-8.

Rice, W. D.; Ambwani, P.; Bombeck, M.; Thompson, J. D.; Haugstad, G.; Leighton, C.; Crooker, S. A. Persistent optically induced magnetism in oxygen-deficient strontium titanate. *Nat. Mater.* **2014,** *13* (5), 481-487.

Sarin, N.; Mishra, M.; Gupta, G.; Parkin, I. P.; Luthra, V. Elucidating iron doping induced n- to p-characteristics of strontium titanate based ethanol sensors. *Curr. Appl. Phys.* **2018,** *18* (2), 246-253.

Sarma, D.; Barman, S.; Kajueter, H.; Kotliar, G. Spectral functions in doped transition metal oxides. *Europhys. Lett.* **1996,** *36* (4), 307.

Sarma, S. D.; de Sousa, R.; Hu, X.; Koiller, B. Spin quantum computation in silicon nanostructures. *Solid State Commun.* **2005,** *133* (11), 737-746.

Sato, K.; Dederichs, P.; Katayama-Yoshida, H.; Kudrnovský, J. Exchange interactions in diluted magnetic semiconductors. *J. Phys.: Condens. Matter* **2004,** *16* (48), S5491.

Savinov, M.; Trepakov, V.; Syrnikov, P.; Železný, V.; Pokorný, J.; Dejneka, A.; Jastrabik, L.; Galinetto, P. Dielectric properties of Mn doped $SrTiO_3$. *J. Phys.: Condens. Matter* **2008,** *20* (9), 095221.

Schimpf, A. M.; Gunthardt, C. E.; Rinehart, J. D.; Mayer, J. M.; Gamelin, D. R. Controlling carrier densities in photochemically reduced colloidal ZnO nanocrystals: size dependence and role of the hole quencher. *J. Am. Chem. Soc.* **2013,** *135* (44), 16569-16577.

Schimpf, A. M.; Gunthardt, C. E.; Rinehart, J. D.; Mayer, J. M.; Gamelin, D. R. Controlling carrier densities in photochemically reduced colloidal ZnO nanocrystals: size dependence and role of the hole quencher. *J. Am. Chem. Soc.* **2013,** *135* (44), 16569-16577.

Schimpf, A. M.; Lounis, S. D.; Runnerstrom, E. L.; Milliron, D. J.; Gamelin, D. R. Redox chemistries and plasmon energies of photodoped $In_2O_3$ and Sn-doped $In_2O_3$ (ITO) nanocrystals. *J. Am. Chem. Soc.* **2015,** *137* (1), 518-524.

Schrader, M.; Mienert, D.; Oh, T.-S.; Yoo, H.-I.; Becker, K. D. An optical, EPR and electrical conductivity study of blue barium titanate, $BaTiO_{3-\delta}$. *Solid State Sci.* **2008,** *10* (6), 768-775.

Schrauben, J. N.; Hayoun, R.; Valdez, C. N.; Braten, M.; Fridley, L.; Mayer, J. M. Titanium and zinc oxide nanoparticles are proton-coupled electron transfer agents. *Science* **2012,** *336* (6086), 1298-1301.

Schwartz, D. A.; Kittilstved, K. R.; Gamelin, D. R. Above-room-temperature ferromagnetic $Ni^{2+}$-doped ZnO thin films prepared from colloidal diluted magnetic semiconductor quantum dots. *Appl. Phys. Lett.* **2004,** *85* (8), 1395-1397.

Scrivenand, B.; Winter, T. R. Chemical oxygen scavengers - Use of hydrazine and tannins for boiler water treatment. *Anti-Corros. Method Mater.* **1978,** *25* (10), 10-11.

Seisenbaeva, G. A.; Daniel, G.; Nedelec, J. M.; Kessler, V. G. Solution equilibrium behind the room-temperature synthesis of nanocrystalline titanium dioxide. *Nanoscale* **2013,** *5* (8), 3330-3336.

Sekiya, T.; Ichimura, K.; Igarashi, M.; Kurita, S. Absorption spectra of anatase $TiO_2$ single crystals heat-treated under oxygen atmosphere. *J. Phys. Chem. Solids* **2000,** *61* (8), 1237-1242.

Shah, J.; Kotnala, R. K. Induced magnetism and magnetoelectric coupling in ferroelectric $BaTiO_3$ by Cr-doping synthesized by a facile chemical route. *J. Mater. Chem. A* **2013,** *1* (30), 8601-8608.

Shannon, R. D. Revised effective ionic radii and systematic studies of interatomic distances in halides and chalcogenides. *Acta Crystallogr. Sect. A: Found. Crystallogr.* **1976,** *32* (5), 751-767.

Shannon, R. D. Revised effective ionic radii and systematic studies of interatomic distances in halides and chalcogenides. *Acta Crystallogr.* **1976,** *32* (5), 751-767.

Shoji, S.; Yamaguchi, A.; Sakai, E.; Miyauchi, M. Strontium titanate based artificial leaf loaded with reduction and oxidation cocatalysts for selective $CO_2$ reduction using water as an electron donor. *ACS Appl. Mater. Interfaces* **2017,** *9* (24), 20613-20619.

Shoji, S.; Yamaguchi, A.; Sakai, E.; Miyauchi, M. Strontium titanate based artificial leaf loaded with reduction and oxidation cocatalysts for selective $CO_2$ reduction using water as an electron donor. *ACS Appl. Mater. Interfaces* **2017,** *9* (24), 20613-20619.

Shvartsman, V.; Bedanta, S.; Borisov, P.; Kleemann, W.; Tkach, A.; Vilarinho, P. (Sr,Mn)$TiO_3$: A magnetoelectric multiglass. *Phys. Rev. Lett.* **2008,** *101* (16), 165704.

Singh, S.; Sharma, V.; Sachdev, K. Investigation of effect of doping concentration in Nb-doped $TiO_2$ thin films for TCO applications. *J. Mater. Sci.* **2017,** *52* (19), 11580-11591.

Sinha, M.; Pearson, T. J.; Reeder, T. R.; Vivanco, H. K.; Freedman, D. E.; Phelan, W. A.; McQueen, T. M. Introduction of spin centers in single crystals of $Ba_6CaWO_{6-\delta}$. *Phys. Rev. Mater.* **2019,** *3* (12), 125002.

Smith, M. B.; Page, K.; Siegrist, T.; Redmond, P. L.; Walter, E. C.; Seshadri, R.; Brus, L. E.; Steigerwald, M. L. Crystal structure and the paraelectric-to-ferroelectric phase transition of nanoscale $BaTiO_3$. *J. Am. Chem. Soc.* **2008,** *130* (22), 6955-6963.

Soledade, L.; Longo, E.; Leite, E.; Pontes, F.; Lanciotti Jr, F.; Campos, C.; Pizani, P.; Varela, J. A. Room-temperature photoluminescence in amorphous $SrTiO_3$–the influence of acceptor-type dopants. *Appl. Phys. A* **2002,** *75* (5), 629-632.

Son, J.; Moetakef, P.; Jalan, B.; Bierwagen, O.; Wright, N. J.; Engel-Herbert, R.; Stemmer, S. Epitaxial $SrTiO_3$ films with electron mobilities exceeding 30,000 $cm^2\ V^{-1}\ s^{-1}$. *Nat. Mater.* **2010,** *9*, 482.

Sood, S.; Umar, A.; Mehta, S. K.; Kansal, S. K. Highly effective Fe-doped $TiO_2$ nanoparticles photocatalysts for visible-light driven photocatalytic degradation of toxic organic compounds. *J. Colloid Interface Sci.* **2015,** *450*, 213-223.

Su, W.; Song, K.; Huo, D.; Li, B. Analysis of correlation between electrical and infrared optical properties of anatase Nb doped $TiO_2$ films. *Current Applied Physics* **2013,** *13* (3), 556-561.

Sun, Z.; Zhang, L.; Dang, F.; Liu, Y.; Fei, Z.; Shao, Q.; Lin, H.; Guo, J.; Xiang, L.; Yerra, N.; Guo, Z. Experimental and simulation-based understanding of morphology controlled barium titanate nanoparticles under co-adsorption of surfactants. *CrystEngComm* **2017,** *19* (24), 3288-3298.

Suzuki, I.; Gura, L.; Klein, A. The energy level of the $Fe^{2+/3+}$ transition in $BaTiO_3$ and $SrTiO_3$ single crystals. *Phys. Chem. Chem. Phys.* **2019,** *21* (11), 6238-6246.

Tan, H.; Zhao, Z.; Zhu, W. B.; Coker, E. N.; Li, B.; Zheng, M.; Yu, W.; Fan, H.; Sun, Z. Oxygen vacancy enhanced photocatalytic activity of pervoskite $SrTiO_3$. *ACS Appl. Mater. Interfaces* **2014,** *6* (21), 19184-19190.

Townsend, T. K.; Browning, N. D.; Osterloh, F. E. Nanoscale strontium titanate photocatalysts for overall water splitting. *ACS nano* **2012,** *6* (8), 7420-7426.

Townsend, T. K.; Browning, N. D.; Osterloh, F. E. Nanoscale strontium titanate photocatalysts for overall water splitting. *ACS Nano* **2012,** *6* (8), 7420-7426.

Tsubakizaki, S.; Gotou, H.; Ishihara, N.; Takada, M.; Mawatari, K.; Kai, R. Alternatives to hydrazine in water treatment at thermal power plants. *Mitsubishi Heavy Ind. Tech. Rev.* **2009,** *46* (2), 43-47.

van Benthem, K.; Elsässer, C.; French, R. H. Bulk electronic structure of $SrTiO_3$: Experiment and theory. *J. Appl. Phys.* **2001,** *90* (12), 6156-6164.

Vandieken, V.; Finke, N.; Thamdrup, B. Hydrogen, acetate, and lactate as electron donors for microbial manganese reduction in a manganese-rich coastal marine sediment. *FEMS Microbiol. Ecol.* **2014,** *87* (3), 733-745.

Verma, K. C.; Kotnala, R. Multiferroic approach for Cr, Mn, Fe, Co, Ni, Cu substituted $BaTiO_3$ nanoparticles. *Mater. Res. Express* **2016,** *3* (5), 055006.

Vlaskin, V. A.; Beaulac, R.; Gamelin, D. R. Dopant– carrier magnetic exchange coupling in colloidal inverted core/shell semiconductor nanocrystals. *Nano Lett.* **2009,** *9* (12), 4376-4382.

Wang, C.; Shim, M.; Guyot-Sionnest, P. Electrochromic nanocrystal quantum dots. *Science* **2001,** *291* (5512), 2390-2392.

Wang, D.; Zhao, L.; Ma, H.; Zhang, H.; Guo, L. H. Quantitative analysis of reactive oxygen species photogenerated on metal oxide nanoparticles and their bacteria toxicity: The role of superoxide radicals. *Environ. Sci. Technol.* **2017,** *51* (17), 10137-10145.

Wang, J.; Choudhary, S.; Harrigan, W. L.; Crosby, A. J.; Kittilstved, K. R.; Nonnenmann, S. S. Transferable memristive nanoribbons comprising solution-processed strontium titanate nanocubes. *ACS Appl. Mater. Interfaces* **2017,** *9* (12), 10847-10854.

Wang, Q.; Hisatomi, T.; Jia, Q.; Tokudome, H.; Zhong, M.; Wang, C.; Pan, Z.; Takata, T.; Nakabayashi, M.; Shibata, N.; Li, Y.; Sharp, I. D.; Kudo, A.; Yamada, T.; Domen, K. Scalable water splitting on particulate photocatalyst sheets with a solar-to-hydrogen energy conversion efficiency exceeding 1%. *Nat. Mater.* **2016,** *15* (6), 611-615.

Wechsler, B.; Klein, M. B. Thermodynamic point defect model of barium titanate and application to the photorefractive effect. *J. Opt. Soc. Am. B* **1988,** *5* (8), 1711-1723.

Wei, Z.; Liu, D.; Wei, W.; Chen, X.; Han, Q.; Yao, W.; Ma, X.; Zhu, Y. Ultrathin $TiO_2$(B) Nanosheets as the Inductive Agent for Transfrering $H_2O_2$ into Superoxide Radicals. *ACS Appl. Mater. Interfaces* **2017,** *9* (18), 15533-15540.

Wick, F. G. Some electrical properties of silicon I. thermo-electric behavior of metallic silicon. *Phys. Rev.* **1907,** *25* (5), 382.

Wrighton, M. S.; Ellis, A. B.; Wolczanski, P. T.; Morse, D. L.; Abrahamson, H. B.; Ginley, D. S. Strontium titanate photoelectrodes. Efficient photoassisted electrolysis of water at zero applied potential. *J. Am. Chem. Soc.* **1976,** *98* (10), 2774-2779.

Xing, P.; Chen, Y.; Yan, S.-S.; Liu, G.; Mei, L.; Zhang, Z. Tunable ferromagnetism by oxygen vacancies in Fe-doped $In_2O_3$ magnetic semiconductor. *J. Appl. Phys.* **2009,** *106* (4), 043909.

Yermakov, A. Y.; Gubkin, A. F.; Korolev, A. V.; Molochnikov, L. S.; Uimin, M. A.; Rosenfeld, E. V.; Kurkin, M. I.; Minin, A. S.; Volegov, A. S.; Boukhvalov, D. W. Formation of Fe–Fe antiferromagnetic dimers in doped $TiO_2$:Fe nanoparticles. *J. Phys. Chem. C* **2018,** *123* (2), 1494-1505.

Yu, H.; Ouyang, S.; Yan, S.; Li, Z.; Yu, T.; Zou, Z. Sol–gel hydrothermal synthesis of visible-light-driven Cr-doped $SrTiO_3$ for efficient hydrogen production. *J. Mater. Chem.* **2011,** *21* (30), 11347-11351.

Yu, J.; Chen, J.; Li, C.; Wang, X.; Zhang, B.; Ding, H. ESR signal of superoxide radical anion adsorbed on $TiO_2$ generated at room temperature. *J. Phys. Chem. B* **2004,** *108* (9), 2781-2783.

Yu, S.; Yun, H. J.; Lee, D. M.; Yi, J. Preparation and characterization of Fe-doped $TiO_2$ nanoparticles as a support for a high performance CO oxidation catalyst. *J. Mater. Chem.* **2012,** *22* (25), 12629-12635.

Zhang, Q.; Huang, Y.; Peng, S.; Huang, T.; Cao, J.-j.; Ho, W.; Lee, S. Synthesis of $SrFe_xTi_{1-x}O_{3-\delta}$ nanocubes with tunable oxygen vacancies for selective and efficient photocatalytic NO oxidation. *Appl. Catal., B* **2018,** *239*, 1-9.

Zhang, S. Y.; Lin, Y. H.; Nan, C. W.; Zhao, R.; He, J. Magnetic and electrical properties of (Mn,La) ‐ codoped $SrTiO_3$ thin films. *J. Am. Ceram. Soc.* **2008,** *91* (10), 3263-3266.

Zhou, D.; Kittilstved, K. R. Control over $Fe^{3+}$ speciation in colloidal ZnO nanocrystals. *J. Mater. Chem. C* **2015,** *3* (17), 4352-4358.

Zhou, D.; Kittilstved, K. R. Electron trapping on $Fe^{3+}$ sites in photodoped ZnO colloidal nanocrystals. *Chem. Commun.* **2016,** *52* (58), 9101-9104.

Zhou, D.; Kittilstved, K. R. Electron trapping on $Fe^{3+}$ sites in photodoped ZnO colloidal nanocrystals. *Chem. Commun.* **2016,** *52* (58), 9101-9104.

Zhou, D. M.; Wang, P. J.; Roy, C. R.; Barnes, M. D.; Kittilstved, K. R. Direct evidence of surface charges in n-type Al-doped ZnO. *J. Phys. Chem. C* **2018,** *122* (32), 18596-18602.

Zhu, H.; Tao, J.; Dong, X. Preparation and photoelectrochemical activity of Cr-doped $TiO_2$ nanorods with nanocavities. *J. Phys. Chem. C* **2010,** *114* (7), 2873-2879.

Zuo, F.; Wang, L.; Wu, T.; Zhang, Z.; Borchardt, D.; Feng, P. Self-doped $Ti^{3+}$ enhanced photocatalyst for hydrogen production under visible light. *J. Am. Chem. Soc.* **2010,** *132* (34), 11856-11857.